

THERMAL LATTICE BOLTZMANN TWO-PHASE FLOW MODEL FOR FLUID
DYNAMICS

by

Peng Yuan

BS, Hefei University of Technology, P. R. China, 1997

MS, Chongqing University, P. R. China, 2000

Submitted to the Graduate Faculty of
the School of Engineering in partial fulfillment
of the requirements for the degree of
Doctor of Philosophy

University of Pittsburgh

2005

UNIVERSITY OF PITTSBURGH
SCHOOL OF ENGINEERING

This dissertation was presented

by

Peng Yuan

It was defended on

November 17, 2005

and approved by

Dr. Giovanni P. Galdi, Professor, Department of Mechanical Engineering,

Dr. Anne M. Robertson, Associate Professor, Department of Mechanical Engineering

Dr. Joseph J. McCarthy, Associate Professor, Department of Chemical & Petroleum Engineering

Dr. Sung K. Cho, Assistant Professor, Department of Mechanical Engineering

Dissertation Director: Dr. Laura Schaefer, Assistant Professor,
Department of Mechanical Engineering

Copyright © by Peng Yuan
2005

THERMAL LATTICE BOLTZMANN TWO-PHASE FLOW MODEL FOR FLUID DYNAMICS

Peng Yuan, PhD

University of Pittsburgh, 2005

This dissertation presents a systematic development of a new thermal lattice Boltzmann multiphase model. Unlike conventional CFD methods, the lattice Boltzmann equation (LBE) method is based on microscopic models and mesoscopic kinetic equations in which the collective behavior of the particles in a system is used to simulate the continuum mechanics of the system. Due to this kinetic nature, the LBE method has been found to be particularly useful in applications involving interfacial dynamics and complex boundaries, e.g. multiphase or multicomponent flows.

First, the methodology and general concepts of the LBE method are introduced. Following this introduction, an accurate mass conserving wall boundary condition for the LBE method is proposed together with benchmark test results. Next, the widely used Shan and Chen (SC) single component two-phase flow model is presented, as well as improvements to that model. In this model, by incorporating fluid-fluid interaction, phase separation and interfacial dynamics can be properly captured. Sharp interfaces between phases can be easily obtained without any additional numerical treatment. In order to achieve flexibility for the surface tension term, an additional force term which represents the contribution of surface tension is incorporated into the fluid-fluid interaction force term. The validity of this treatment is verified by our simulation results. Different equations of state are also incorporated into this model to compare their behavior.

Finally, based on the SC model, a new and generalized lattice Boltzmann model for simulating thermal two-phase flow is described. In this model, the SC model is used to simulate the fluid dynamics. The temperature field is simulated using the passive-scalar approach, i.e. through modeling the density field of an extra component, which evolves according to the advection-diffusion equation. By coupling the fluid dynamics and temperature field through a suitably defined body force term, the thermal two-phase lattice Boltzmann model is obtained. Our simulation results show that different equations of state, variable wettability, gravity and buoyancy effects, and relatively high Rayleigh numbers can be readily simulated by this new model. Lastly, the accomplishments of this study are summarized and future perspectives are provided.

TABLE OF CONTENTS

LIST OF TABLES	x
LIST OF FIGURES	xi
NOMENCLATURE	xvi
ACKNOWLEDGEMENTS.....	xxiii
1.0 THE LATTICE BOLTZMANN EQUATION METHOD	1
1.1 INTRODUCTION	1
1.2 DIFFERENT APPROACHES FOR FLUID MODELING	1
1.2.1 Traditional computational fluid dynamics methods	2
1.2.2 Molecular dynamics (MD) method	4
1.2.3 Lattice gas and lattice Boltzmann equation methods	5
1.3 OVERVIEW OF THE LBE METHOD.....	8
1.4 FROM THE CONTINUUM BOLTZMANN EQUATION TO THE LBE MODEL	14
2.0 IMPROVEMENT OF BOUNDARY TREATMENT IN THE LBE METHOD.....	18
2.1 INTRODUCTION	18
2.2 THE OPEN BOUNDARY CONDITION	18
2.2.1 Periodical boundary condition.....	19
2.2.2 Extrapolation boundary condition	19
2.2.3 Bounce-back and other boundary conditions for the inlet	20
2.3 WALL BOUNDARY CONDITIONS.....	22
2.3.1 Fullway and halfway bounce-back wall boundary conditions	22

2.3.2	Solid wall boundary conditions for a curved boundary	24
2.3.3	Slip velocity for different wall boundary conditions.....	26
2.3.4	Mass conserving solid wall boundary condition	29
2.3.4.1	Drawbacks of FH & MLS's BC.....	29
2.3.4.2	Implementation of mass conserving solid wall BC.....	35
2.3.4.3	Benchmark tests for the new boundary condition.....	41
2.3.4.4	Conclusion.....	54
2.4	DISCUSSION.....	54
3.0	MULTIPHASE LBE MODEL	56
3.1	INTRODUCTION	56
3.2	COMPUTATIONAL APPROACHES USED IN TWO-PHASE FLOW SIMULATION.....	57
3.2.1	Front capturing methods.....	57
3.2.2	Front-tracking methods	59
3.2.3	Lattice Boltzmann two-phase models	60
3.3	SINGLE COMPONENT MULTIPHASE LATTICE BOLTZMANN MODEL ..	61
3.4	BENCHMARK TESTS	67
3.4.1	Single-phase flow tests for LBE model.....	67
3.4.2	Two-phase flow tests for LBE model.....	70
3.5	PHASE EQUILIBRIUM AND WETTABILITY.....	74
3.6	SURFACE TENSION IN THE LBE MODEL.....	81
3.6.1	Surface tension in original SC LBE model	82
3.6.2	Changing surface tension in the SC LBE model.....	83
3.7	DISCUSSION.....	91
4.0	EQUATIONS OF STATE IN THE LBE MODEL	92
4.1	INTRODUCTION	92
4.2	CRITERIA USED IN EVALUATING EQUATIONS OF STATE.....	94

4.2.1	Spurious currents.....	95
4.2.2	Stable temperature range.....	96
4.2.3	Coexistence curve.....	97
4.2.4	Density ratio.....	97
4.3	INCORPORATING EQUATIONS OF STATE.....	98
4.4	SIMULATION RESULTS.....	101
4.4.1	Comparison of different types of equations of state.....	102
4.4.2	Comparison of different cubic equations of state.....	104
4.4.3	Comparison of equations of state and actual fluid properties.....	111
4.5	DISCUSSION.....	113
5.0	THERMAL LBE MODEL.....	115
5.1	INTRODUCTION.....	115
5.2	SINGLE-PHASE TLBE MODEL.....	116
5.2.1	Numerical method.....	116
5.2.2	Boundary conditions.....	117
5.2.3	Benchmark tests.....	118
5.3	MULTIPHASE TLBE MODEL.....	123
5.4	SIMULATION RESULTS.....	124
5.4.1	Initial flow field and temperature setting.....	124
5.4.2	Multiphase thermal flow base case.....	125
5.4.3	Effect of varying Rayleigh number.....	128
5.4.4	Nusselt number variation.....	129
5.4.5	Effect of fluid-solid interaction strength.....	133
5.5	DISCUSSION.....	134
6.0	CONCLUSIONS AND FUTURE WORK.....	135

6.1	MAJOR ACCOMPLISHMENTS.....	135
6.2	FUTURE WORK.....	137
6.3	APPLICATIONS OF THE MODEL.....	141
	APPENDIX A.....	143
	FROM THE LBE TO THE N-S EQUATIONS.....	143
	BIBLIOGRAPHY.....	148

LIST OF TABLES

Table 2.1: The L_2 -norm error obtained by different boundary conditions.	43
Table 2.2: L_2 -norm error obtained by different boundary conditions.....	49
Table 3.1: Vortex centers: Stream function and location	68
Table 4.1: Properties at T_{\min} for different EOS	103
Table 5.1: Nusselt numbers at different g_w values	133

LIST OF FIGURES

Figure 1.1: Two different types of numerical solutions: “top-down” and “bottom-up” (after [6]).	3
Figure 1.2: An example of one time step in the evolution of a two-dimensional lattice gas. (a) Initial condition: each arrow represents a particle of unit mass moving in the direction of the arrow (its lattice velocity); (b) Streaming step: each particle moves one lattice unit in the direction of its velocity; (c) Collision step. (after [12]).	6
Figure 1.3: Discrete velocity vectors for some commonly used 2-D and 3-D particle speed models.	10
Figure 2.1: Layout of the inlet boundary.	20
Figure 2.2: Configuration of PDFs used to construct the inlet boundary condition: (a) Configuration of equilibrium PDFs at the inlet, (b) Configuration of non-equilibrium PDFs at the inlet (the gray color denotes a fluid node).	21
Figure 2.3: Illustration of fullway and halfway bounce-back boundary conditions. t_t denotes a time step after a propagation process and t'_t denotes the time after the application of the boundary condition. The gray color represents the boundary nodes (after [51]).	23
Figure 2.4: Layout of the lattice and curved wall boundary (after [49]).	25
Figure 2.5: Relation between α and τ .	27
Figure 2.6: System mass changes with time in a typical LBE simulation.	29
Figure 2.7: Schematic of static flow under gravity.	30
Figure 2.8: System mass changes with time using FH’s BC.	30
Figure 2.9: Mass changing rate varying with time.	31
Figure 2.10: Density as a function of height at selected time.	34
Figure 2.11: PDFs of a flat boundary site at the lower wall boundary after the streaming step.	36
Figure 2.12: System mass changes with time using new BC.	37

Figure 2.13: The mass distribution at $x = nx/2$ when $t = 60000$ obtained from different schemes.	38
Figure 2.14: y -component of velocity at $x = nx/2$ when $t = 60000$ obtained from different schemes.	38
Figure 2.15: Three flat wall boundary configurations. Blue dashed arrows, red plain arrows and black plain arrows represent the incoming distribution, outgoing distribution and fluid-fluid (buried) distribution. Gray areas represent the solid part.	39
Figure 2.16: Dependence of relative L_2 -norm error on the lattice resolution for 2-D channel flow.	42
Figure 2.17: Relative L_2 -norm error as a function of Δ for 2-D channel flow.	42
Figure 2.18: Regions of stability and instability in the LBE computation for fully developed 2-D channel flow (after [56]) (a) Using FH's BC, (b) Using MLS's BC	44
Figure 2.19: System mass as a function of time using MLS's BC.	45
Figure 2.20: Regions of stability and instability in the LBE computation for fully developed 2-D channel flow using new BC.	46
Figure 2.21: Stability boundary of the FH's scheme in a square duct flow for Δ near 1.0 (after [50]).	46
Figure 2.22: Obtained velocity profiles (black dots) over a complete period compared to the exact solution (red lines). The measurements are taken at the middle of the channel, at each $t = 0.04nT$ when $n = 0,1,\dots,25$	48
Figure 2.23: Dependence of relative L_2 -norm error on the lattice resolution for oscillating 2-D channel flow.	49
Figure 2.24: Velocity profiles at $t = 100$ (in lattice units) for Stokes first problem with different values of Δ	50
Figure 2.25: Relative L_2 -norm error as function of time for the Stokes first problem with different values of Δ	51
Figure 2.26: Velocity profiles at $nx/4$ and $nx/2$ in lid-driven cavity flow for $\Delta = 0.5$ and halfway bounce-back (denote as BBL: bounce-back at link in the figures) scheme. (a) x component of velocity, (b) y component of velocity.	52
Figure 2.27: Velocity profiles at $nx/4$ and $nx/2$ for different values of Δ . (a) x component of velocity, (b) y component of velocity.	53
Figure 3.1: Schematic for the Marker-and-Cell method (after [63]).	58

Figure 3.2: Schematic for boundary-fitted method (after [63]).	59
Figure 3.3: Streamlines of 2-D lid-driven cavity flow at $Re = 10^3$.	68
Figure 3.4: Velocity profiles for u along the vertical geometric centerline of the cavity.	68
Figure 3.5: Comparison of axial velocity profile.	69
Figure 3.6: Dependence of relative L_2 -norm on lattice resolution.	69
Figure 3.7: Snapshots of the droplet shape at different times ($\nu = 0.16667$, $\rho_l = 2.261$, $\rho_v = 0.122$). Red color represents liquid phase (high density) and blue color represents vapor phase (low density).	71
Figure 3.8: The radius at $y = ny/2$ as a function of time.	72
Figure 3.9: The oscillations of a deformed droplet with the initial shape of an ellipse at several times ($\nu = 0.16667$, $\rho_l = 2.307$, $\rho_v = 0.118$). Red color represents liquid phase (high density) and blue color represents vapor phase (low density).	73
Figure 3.10: The evolutions of length of the major and minor axis with time.	74
Figure 3.11: Maximum and minimum density values as a function of $ g_f $.	75
Figure 3.12: Density ratio as a function of $ g_f $.	75
Figure 3.13: Density contours and velocity vectors in the xy -plane at $z = 25$.	76
Figure 3.14: The maximum magnitude of spurious currents changing with $ g_f $.	78
Figure 3.15: Contact angle between a fluid-fluid interface and a solid wall. γ denotes the interfacial tension between fluids, and θ denotes the contact angle.	78
Figure 3.16: Density contours for different values of g_w (different wettabilities).	79
Figure 3.17: Velocity fields for different values of g_w .	80
Figure 3.18: The relation between the contact angle θ of the drop and the fluid-solid interaction strength g_w .	81
Figure 3.19: Test of the Laplace law. The slope (i.e. the surface tension) is 0.09728 and the coefficient of determination is 0.99943.	83
Figure 3.20: Estimation of surface tension from curvature (1/radius) and pressure difference between the inside and outside of simulated bubbles/droplets.	85

Figure 3.21: Surface tension coefficient σ as a function of the strength of the surface tension κ . The inset diagram shows the small κ values: $-0.4 \leq \kappa \leq 0.4$	85
Figure 3.22: Density contours at $\kappa = -0.9$	86
Figure 3.23: Maximum magnitude of spurious current as a function of κ	87
Figure 3.24: Simulation set up and wave initialization.....	88
Figure 3.25: The y position of the capillary wave interface as a function of time. The red line is the exponential curve fitted to the peak points (dots).....	88
Figure 3.26: The dispersion relation (angular frequency ω vs. wave number k). Simulation results using $\kappa = 0$ are compared with the corresponding analytical solution from potential theory, Eq. (3.21a).....	90
Figure 4.1: Pressure-density relationship of the SC EOS under different g_f values.	93
Figure 4.2: The maximum magnitude of spurious current changes with reduced temperature....	97
Figure 4.3: The maximum magnitude of the spurious current varying with the density ratio for the vdW EOS.....	102
Figure 4.4: Maximum magnitude of the spurious current varying with the density ratio for the SC EOS and C-S EOS.....	103
Figure 4.5: The maximum magnitude of the spurious current variation with density ratio for different EOS.....	105
Figure 4.6: Coexistence curves for three EOS.....	106
Figure 4.7: Comparison of coexistence curves obtained from simulations with theoretical values for different EOS.....	109
Figure 4.8: Comparison of the vapor branch of the coexistence curves obtained from simulations for R-K EOS and P-R EOS.....	110
Figure 4.9: Comparison of coexistence curves obtained from simulations with theoretical values obtained by equating the chemical potentials for C-S EOS.....	110
Figure 4.10: Comparison of coexistence curve obtained from simulations with theoretical values for P-R EOS with $\omega = 0.011$	111
Figure 4.11: Comparison of the saturated density of water obtained from simulations with experimental data from the steam table for different EOS.....	112
Figure 5.1: Velocity vectors and isotherms at $Ra = 5000$, $Pr = 1.0$	119

Figure 5.2: Growth rate of instability vs. Ra number	120
Figure 5.3: Isotherms at steady state obtained by the LBE method.....	122
Figure 5.4: Nusselt number at the top wall with respect to the time step obtained by the LBE method.	122
Figure 5.5: Isotherms, density contours and velocity vectors at Ra = 10000 , Re = 100	126
Figure 5.6: Isotherms and density contours at different Rayleigh numbers	129
Figure 5.7: Nusselt numbers of the bulk flow, at the top wall, and at the bottom wall as functions of the time step (Ra = 10000 , Re = 100).	130
Figure 5.8: The bulk Nusselt number changing with the time step at different Rayleigh numbers.	130
Figure 5.9: The bulk Nusselt number changing with time step at different Reynolds numbers.	131
Figure 5.10: Isotherms and density contours at Ra = 10000 , Re = 500	132

NOMENCLATURE

Roman Letters

a, \mathbf{a}	Acceleration; attraction parameter in equation of state
b	Repulsion parameter in equation of state
c	Lattice speed; lattice spacing
c_0	Constant in equation of state
c_s	Lattice sound speed
c_V	Specific heat capacity
D	Dimension of space
\mathbf{e}_α	Lattice velocity vector
f_α	Particle distribution function
$f_\alpha^{(eq)}$	Equilibrium particle distribution function
\mathbf{F}	Force per unit mass
g	Gravitational constant; fluid-fluid interaction strength
g_f	Intensity of fluid-fluid interaction
g_w	Intensity of fluid-solid interaction

\mathbf{G}	Buoyancy force per unit mass
$G(\mathbf{x}, \mathbf{x}')$	Green's function (related to the fluid-fluid interaction potential)
$G_w(\mathbf{x}, \mathbf{x}')$	Green's function (related to the fluid-solid interaction potential)
H	Height of the domain
k	Thermal conductivity; wave number
L	Length of the domain; wavelength
n_x, n_y, n_z	Lattice size in the x , y and z directions
Nu	Nusselt number
p	Pressure
p^*	Non-ideal part of pressure
Pr	Prandtl number
q'''	Heat generation per volume
q^*	Non-dimensional heat
R	Gas constant; radius
Ra	Rayleigh number
Re	Reynolds number
t	Time
t^*	Non-dimensional time
T	Temperature

T_0	Reference temperature
$\mathbf{u}, u, \mathbf{U}$	Fluid velocity
\mathbf{u}^{eq}	Equilibrium velocity
$ \mathbf{u}^s _{\max}$	Magnitude of maximum spurious current
U'	Characteristic velocity
w_α, W_α	Weighting coefficients
\mathbf{x}, \mathbf{x}'	Position

Greek Letters

α	Thermal diffusivity
β	Thermal expansion coefficient
γ	Damping rate of the wave
δt	Time step
$\delta x, \delta y$	Lattice constant
Δ	Fraction of an intersected link in the fluid region
ΔT	Temperature difference
θ	Contact angle
κ	Coefficient in surface tension term
λ	Relaxation time

μ	Dynamic viscosity
ν	Kinematic viscosity
ξ_α	Discrete velocity set
$\Pi_{\alpha\beta}$	Momentum flux tensor
ρ	Density
ρ_w	Wall density
σ	Coefficient of surface tension
τ	Relaxation time
τ_T	Relaxation time for temperature field
χ	Weighting coefficient used in linear interpolation
ψ	Effective mass
Ψ	Heat source term
ω	Oscillating frequency; angular frequency; acentric factor in equation of state
Ω	Collision operator

Subscripts

α	Lattice direction
b	Boundary node
c	Critical value

f	Fluid node
i	Initial value
l	Liquid phase
Lu	Lattice unit
v	Vapor phase
w	Wall node

Superscripts

*	Quantifier denoting non-dimensional variables
–	Quantifier denoting average values
~	Quantifier denoting post-collision state
(<i>eq</i>)	Quantifier denoting equilibrium properties
(<i>neq</i>)	Quantifier denoting non-equilibrium properties

Abbreviations

BC	Boundary condition
BGK	Bhatnagar-Gross-Krook
CFD	Computational fluid dynamics
CFL	Courant-Friedrichs-Lewy
C-S	Carnahan-Starling

EOS	Equation of state
FD	Finite difference
FH	Filippova and Hänel
FHP	Frisch, Hasslacher, and Pomeau
HCZ	He, Chen, and Zhang
LB	Lattice Boltzmann
LBE	Lattice Boltzmann equation
LBGK	Lattice BGK
LGA	Lattice gas automata
MLS	Mei, Luo, and Shyy
N-S	Navier-Stokes
PDE	Partial differential equation
PDF	Particle distribution function
P-R	Peng-Robinson
RHS	Right hand side
R-K	Redlich-Kwong
RKS	Redlich-Kwong Soave
SC	Shan & Chen
SRT	Single relaxation time

TLBE Thermal LBE

vdW van der Waals

ACKNOWLEDGEMENTS

During this work, I was in contact with many people who helped me in numerous ways. Let me try to thank them without, I hope, forgetting anyone.

First and foremost, I wish to acknowledge my advisor, Dr. Laura Schaefer, for supporting me, encouraging me, for providing continuous motivation and guidance throughout my dissertation work and for all her optimism, patience and words of kindness. For me she has been an advisor, a collaborator, and a friend. Thank you.

My thanks are extended to the members of my thesis committee, Drs. Giovanni P. Galdi, Anne M. Robertson, Joseph J. McCarthy and Sung K. Cho. Thank you for your time, encouragement and valuable advice. I also thank Dr. Galdi and Robertson for the wonderful classes they gave. I am very thankful to the faculty and staff members in the Department of Mechanical Engineering, who have made my studies here valuable and enjoyable.

Special thanks go to Dr. Qinjun Kang and Robert Nourgaliev for the interesting discussions and their helpful suggestions.

I feel lucky to have made a lot of new friends here. My time spent in Pitt went by much faster due to the following people: Jun Zhang, Tao Zhang, Qingming Chen, Yue Ke, Zhouyan Wang, Fang Li, Yixin Lu, Fei Yan, Yuksel Korkmaz, Omer Bilen, Mesut Gur, Yuki Yamamoto, Robyn Peifley, and Parker Lin.

I reserve my sincere thanks for my family members. I am deeply indebted to my father: Zhongmin Yuan, my mother Huidian Liu, and my brother Kun Yuan for their never ending love, dedication and support through my long journey of study. They have done so much for me in the

past, and words cannot express the gratitude I have. I am also thankful for the love and encouragements provided by my wife's parents and my sister-in-law.

Finally, I would like to thank my wife Chunhua Fu for sharing with me all the exciting and difficult times of living in a foreign country, and for all her love, support and faith in me. Her brilliant smile made and will make my life go well.

1.0 THE LATTICE BOLTZMANN EQUATION METHOD

1.1 INTRODUCTION

Recently, the lattice Boltzmann equation (LBE) method has been successfully applied to simulate fluid flow and transport phenomena [1]. Unlike conventional CFD methods, the LBE method is based on microscopic models and mesoscopic kinetic equations in which the collective behavior of the particles in a system is used to simulate the continuum mechanics of the system. Due to this kinetic nature, the LBE method has been found to be particularly useful in applications involving interfacial dynamics and complex boundaries, e.g. multiphase or multicomponent flows [2]. In this chapter, we will introduce the methodology and general concepts of LBE method without going into details. The details of LBE model and its application are presented in the following chapters.

1.2 DIFFERENT APPROACHES FOR FLUID MODELING

Macroscopic systems and transport phenomena have been systematically investigated since the 19th century. Two basic approaches were used in the study. One is the macroscopic continuum theory, including fluid mechanics and thermodynamics. The other is the microscopic approach, namely kinetic theory, the non-equilibrium branch of statistical mechanics. Both views will give the same macroscopic governing equations for systems composed of many particles.

Classical fluid mechanics studies a fluid system from a macroscopic point of view. It means that although a fluid system consists of discrete particles, no consideration is given to the detailed behavior of each individual molecule. The usual interest is in obtaining macroscopic variables, such as density, pressure, temperature and velocity, which characterize the state of the fluid system. Based on the continuum assumption, Navier-Stokes (N-S) equations can be derived through conservation laws. How to solve the N-S equations with specific boundary conditions, initial conditions and physical constraints becomes one of main tasks of fluid mechanics research. Statistical mechanics and kinetic theory, on the other hand, study macroscopic systems, such as fluid and thermal systems, using a microscopic approach based on realistic molecular models. It is well known that a fluid is a discrete system with a large number of particles or molecules (the number of particles can be as large as $2.7 \times 10^{19}/\text{cm}^3$ for a gas at normal conditions). Meanwhile the initial conditions are usually not known. Thus, it can be a formidable task to solve such a system of many particles. Statistical mechanics bypasses these difficulties by considering all possible states of a system and finding the probability for each state. A macroscopic quantity is then obtained by evaluating a weighted average of a physical quantity over such states [3]. By doing this, three levels of equations can be obtained: the Liouville equation on the microscopic level, the kinetic equations (including Boltzmann equation) on the mesoscopic level, and the N-S equations on the macroscopic level.

1.2.1 Traditional computational fluid dynamics methods

It is usually convenient to solve a fluid problem by using the governing partial differential equations (PDEs), such as the N-S equations. Almost all traditional computational fluid dynamics (CFD) methods are based on solving either differential or integral forms of the PDEs.

These are the so-called “top-down” approaches, as illustrated in Figure 1.1. These approaches start from the governing PDEs and discretize them (usually on a regular-sized mesh) by finite difference, finite volume or finite element methods. The approximate solutions are then obtained on the discretized spatial and temporal scales [4, 5]. On the other hand, solutions based on the kinetic theory, the LBE method and its ancestor lattice gas automata (LGA) are “bottom-up” approaches. They solve mesoscopic equations (such as the Boltzmann equation) for an ensemble-averaged distribution of moving, interacting fluid particles on a discrete lattice. Then, by using a multi-scale analysis, the desired macroscopic PDEs can be recovered. Molecular dynamics is another “bottom-up” approach, which simulates the macroscopic behavior of a fluid system at the microscopic level.

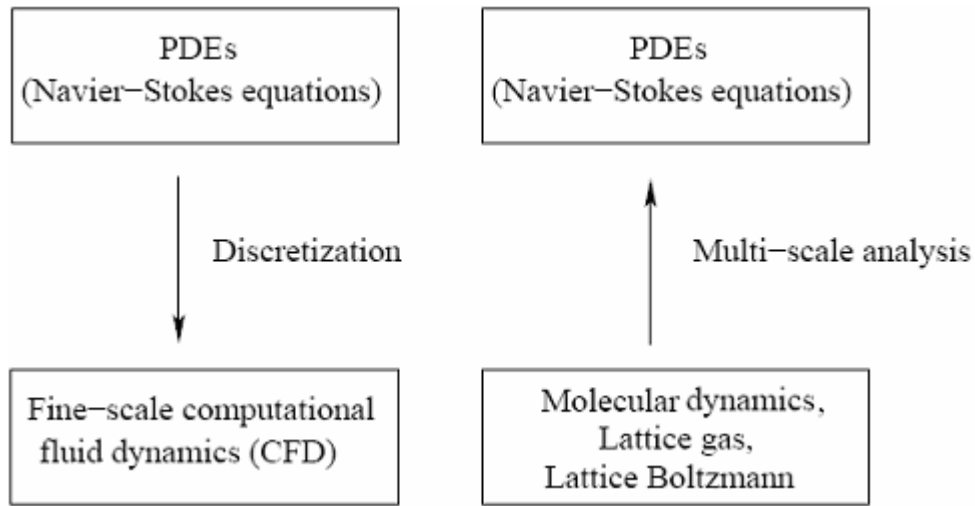


Figure 1.1: Two different types of numerical solutions: “top-down” and “bottom-up” (after [6]).

Although a wide variety of flows can be addressed by traditional CFD methods with great accuracy, there still exist flows for which traditional CFD methods are not adapted. Two examples are presented. First, multiphase flow, especially when the interfaces undergo topological changes may not be accurately modeled with a macroscale approach. Using

traditional CFD methods, one might be able to track a few, but hardly many interfaces in a system. A second example is the flow of lava or mud. These fluids are typically non-Newtonian fluids. Therefore, the N-S equations are no longer suitable. However, these examples, as well as many other flows, can be more easily dealt with using the LBE method.

1.2.2 Molecular dynamics (MD) method

It is well known that fluid is made of the discrete atoms/molecules. Therefore, tracing the movements and collisions of all individual molecules becomes an obvious way of flow simulation. This is the so-called molecular dynamics approach and is often used in material science and biological research, particularly for investigating the structure, dynamics and thermodynamics of biological molecules and their complexes [7, 8, 9]. The MD method is deterministic: at every time step, the new position and velocity of all molecules are calculated from their previous position and velocity based on Newton's second law.

Obviously, MD simulations are time consuming and computationally expensive. As a result, the number of molecules that can be simulated is still very limited at this stage. Two possible ways have been proposed to reduce the computational demands for MD methods. First, instead of considering each individual molecule at the molecular (microscopic) scale, fluid particles at mesoscopic scale, which are made up of a group of molecules are considered in the simulation. Second, the degree of the freedom of the system can be reduced by forcing the fluid particles to move in specified directions. It is based on these concepts that the lattice Boltzmann method and its ancestor lattice gas method emerged and have been successfully applied to simulate fluid flow and transport phenomena.

1.2.3 Lattice gas and lattice Boltzmann equation methods

Historically, the LBE method was derived from lattice gas automata, a discrete particle kinetics, utilizing a discrete lattice and discrete time. The first two-dimensional LGA model was proposed by Frisch, Hasslacher, and Pomeau (known as the FHP model) in 1986 [10]. The FHP model uses a triangular lattice, and, unlike the previous similar models, for the first time it recovers the two-dimensional N-S equations. The evidence that a simple LGA model could faithfully simulate hydrodynamics paved the way for its rapid development. Shortly after the FHP model was introduced, three-dimensional LGA models were proposed by d’Humières, Lallemand and Frisch [11].

The essential features of LGA are very different from those of traditional CFD methods. In order to construct the kinetic LGA model, a lattice with correct symmetry must first be designed, and then suitable evolution rules must be established. At each lattice node, a set of Boolean variables $n_\alpha(\mathbf{x}, t)$ ($n_\alpha = 0, \text{ or } 1; \alpha = 1, \dots, N$) is used to describe the particle occupation, where the subscript α is an index for velocity and denotes a different velocity direction, \mathbf{x} is a vector in the lattice space, t denotes discrete time and N is the number of particle velocities. There is either no particle $n_\alpha = 0$ or one particle $n_\alpha = 1$ in the α th-direction, as shown in Figure 1.2a. The evolution equation of LGA can be written as:

$$n_\alpha(\mathbf{x} + \mathbf{e}_\alpha, t + 1) = n_\alpha(\mathbf{x}, t) + \Omega_\alpha(n(\mathbf{x}, t)) \quad (1.1)$$

where \mathbf{e}_α are the local particle velocities and Ω_α is the collision operator. The evolution of LGA consists of two alternative steps: (1) Streaming: a particle moves to the nearest neighboring node along its velocity direction (see Figure 1.2b), and (2) Collision: particles collide with each other and change their velocities and directions according to collision rules after arriving at the

neighboring nodes, as shown in Figure 1.2c. It is very important to construct collision rules for LGA. The correct collision rules must guarantee that mass, momentum, and energy are conserved in the collision and meanwhile no spurious invariance is preserved.

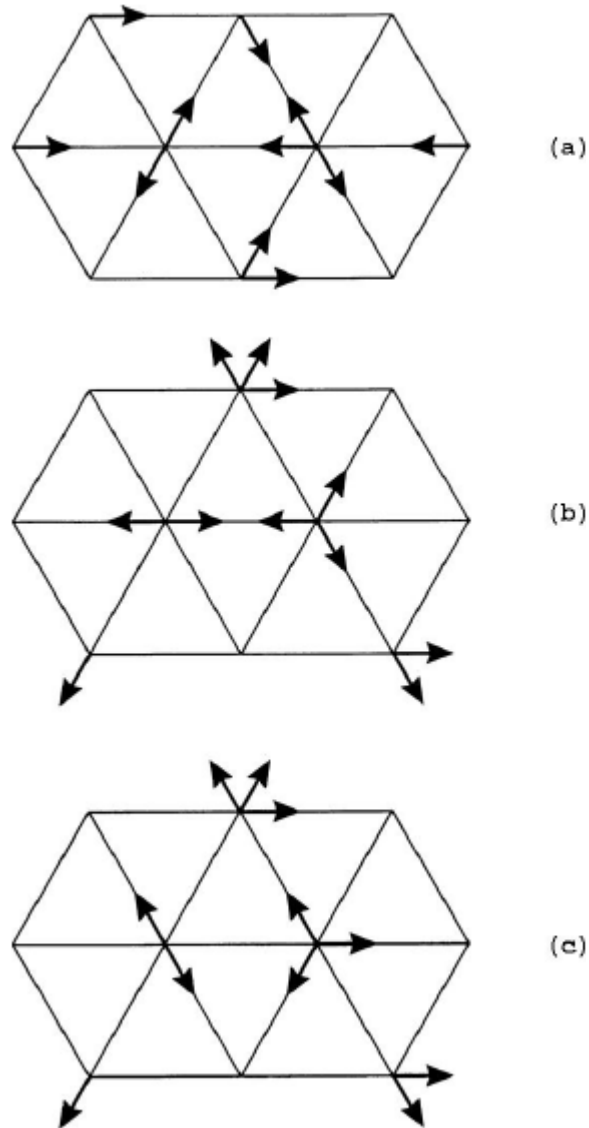


Figure 1.2: An example of one time step in the evolution of a two-dimensional lattice gas. (a) Initial condition: each arrow represents a particle of unit mass moving in the direction of the arrow (its lattice velocity); (b) Streaming step: each particle moves one lattice unit in the direction of its velocity; (c) Collision step. (after [12]).

The LGA has several advantages over traditional CFD methods, like simple evolution rules, which are easy to implement as parallel computations [13, 14]. However, it also has several undesirable features. The most serious one is the inherent statistical noise in the simulations due to the large fluctuation in n_α . Also in LGA, the Galilean invariance is destroyed because of the existence of a density-dependent coefficient in the convection term of the N-S equations.

To overcome the intrinsic drawbacks of LGA, its real variable counterparts, LBE models, were introduced. The most striking feature of the LBE method is the replacement of the particle occupation variables n_α (Boolean variables) in the evolution equation by the particle distribution functions (PDFs) $f_\alpha = \langle n_\alpha \rangle$, where $\langle \cdot \rangle$ denotes the local ensemble average. Therefore, f_α are real variables, and $0 \leq f_\alpha \leq 1$. This eliminates the statistical noise in LGA. The first LBE model was proposed by McNamara and Zanetti [15], in which the same form of the collision operator as in the LGA was adopted. Later on, Higuera, Jimenez and Succi introduced a linearized, matrix collision operator which can avoid the detailed collision rules. Although the statistical noise was eliminated in both models, other problems still remained, because the equilibrium distribution is still Fermi-Dirac. Chen *et al.* [16] and Qian *et al.* [17] proposed LBE models in which Fermi-Dirac statistics were abandoned, and thus provided the freedom required for the equilibrium distribution to satisfy isotropy, Galilean invariance and to possess a velocity-independent pressure. In their models, the single relaxation time approximation known as the Bhatnagar, Gross and Krook (BGK) approximation was applied to greatly simplify the collision operator. The LBE model with the BGK approximation is called the lattice BGK (LBGK) model. There also exist other LBE models, like the Somers model [18]. However, the LBGK model is the most widely used model in lattice Boltzmann (LB) simulations. We will focus on this model in our later discussions.

Although the LBE method was developed only a decade ago, it has attracted significant attention and has been applied to a variety of flow fields, such as magnetohydrodynamics [19], flow in dynamic geometry (blood flow) [20], turbulence and large eddy simulation [21], wave propagation [22], and global ocean circulation [23, 24]. The LGA and LBE methods have been particularly successful in the area of complex fluids including multiphase fluids [25], suspensions in fluid [26, 27], viscoelastic flow [28, 29], and chemical reaction flows [30]. The applications of the LBE method are very diverse and interdisciplinary. More details about the various applications of the LBE method can be found in the review articles [1, 2] and monographs [1, 31].

1.3 OVERVIEW OF THE LBE METHOD

The continuum Boltzmann equation is an integro-differential equation, which describes the evolution of the single-particle distribution function $f(\mathbf{x}, \boldsymbol{\xi}, t)$ in the physical-momentum space (phase space):

$$\frac{\partial f}{\partial t} + \boldsymbol{\xi} \cdot \nabla_{\mathbf{x}} f + \mathbf{a} \cdot \nabla_{\boldsymbol{\xi}} f = Q(f, f) \quad (1.2)$$

The collision integral is:

$$Q(f, f) = \int d^3 \xi_1 \int d\Omega \sigma(\Omega) |\boldsymbol{\xi} - \boldsymbol{\xi}_1| [f(\boldsymbol{\xi}') f(\boldsymbol{\xi}'_1) - f(\boldsymbol{\xi}) f(\boldsymbol{\xi}_1)] \quad (1.3)$$

with $\sigma(\Omega)$ as the differential collision cross section for the two-particle collision which transforms the velocities from $\{\boldsymbol{\xi}, \boldsymbol{\xi}_1\}$ (incoming) into $\{\boldsymbol{\xi}', \boldsymbol{\xi}'_1\}$ (outgoing). The position in physical space is denoted by \mathbf{x} and the velocity in the momentum (or velocity) space is denoted by $\boldsymbol{\xi}$. $f(\mathbf{x}, \boldsymbol{\xi}, t) d^3 x d^3 \boldsymbol{\xi}$ represents the probability of finding a particle in the volume $d^3 x$ around

\mathbf{x} and with velocity between ξ and $\xi + d\xi$. The \mathbf{a} is the force per unit mass acting on the particle, which will be neglected in the later discussion in this chapter.

The Boltzmann equation has its foundations in gas dynamics and is a well-accepted mathematical model of a fluid at the microscopic level. It provides detailed microscopic information, which is critical for the modeling of the underlying physics behind complex fluid behavior. It is more fundamental than the N-S equations. However, due to the high dimensions of the distribution and the complexity in the collision integral, direct solution of the full Boltzmann equation is a formidable task for both analytical and numerical techniques [32].

One of the major difficulties in dealing with the Boltzmann equation is the complicated nature of the collision integral. Therefore, as mentioned previously, an important simplification of collision term was proposed by Bhatnagar, Gross and Krook in 1954 [33] and is known as the BGK approximation. The Boltzmann-BGK equation then takes the form:

$$\frac{\partial f}{\partial t} + \xi \cdot \nabla f = -\frac{1}{\lambda} [f - f^{(0)}] \quad (1.4)$$

where ξ is the particle velocity, $f^{(0)}$ is the equilibrium distribution function (the Maxwell-Boltzmann distribution function), and λ is the relaxation time.

To solve for f numerically, Eq. (1.4) is first discretized in the momentum space using a finite set of velocities $\{\xi_\alpha\}$ without violating the conservation laws.

$$\frac{\partial f_\alpha}{\partial t} + \xi_\alpha \cdot \nabla f_\alpha = -\frac{1}{\lambda} [f_\alpha - f_\alpha^{(eq)}] \quad (1.5)$$

in the above equation, $f_\alpha(\mathbf{x}, t) \equiv f(\mathbf{x}, \xi_\alpha, t)$ and $f_\alpha^{(eq)}(\mathbf{x}, t) \equiv f^{(0)}(\mathbf{x}, \xi_\alpha, t)$ are the distribution function and the equilibrium distribution function of the α th discrete velocity ξ_α , respectively.

For 2-D flow, the 9-velocity LBE model on the 2-D square lattice, denoted as the D2Q9 model,

has been widely used. For simulating 3-D flow, there are several cubic lattice models, such as the D3Q15, the D3Q19 and the D3Q27 model. Figure 1.2 presents the most common lattices. The equilibrium distributions for all of the D2Q9, D3Q15, D3Q19 and D3Q27 models can be expressed in the form:

$$f_{\alpha}^{(eq)} = \rho w_{\alpha} \left[1 + \frac{3}{c^2} \mathbf{e}_{\alpha} \cdot \mathbf{u} + \frac{9}{2c^4} (\mathbf{e}_{\alpha} \cdot \mathbf{u})^2 - \frac{3}{2c^2} \mathbf{u} \cdot \mathbf{u} \right] \quad (1.6)$$

where w_{α} is the weighting factor, $c = \delta x / \delta t$ is the lattice speed, \mathbf{e}_{α} denotes the discrete velocity set, δx and δt are the lattice constant and the time step, respectively, and \mathbf{u} is the macroscopic velocity.

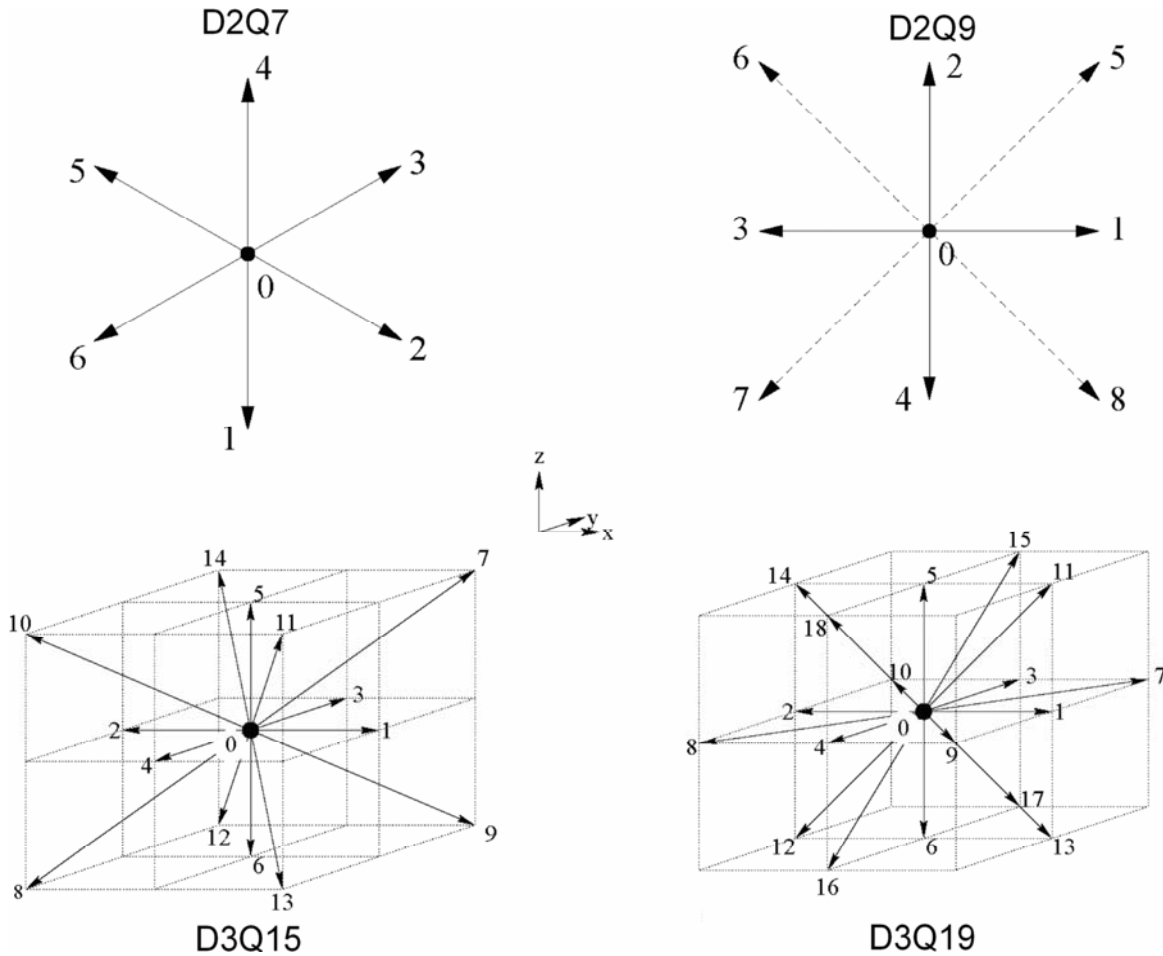


Figure 1.3: Discrete velocity vectors for some commonly used 2-D and 3-D particle speed models.

In our simulations, the D2Q9 and D3Q19 models, which have been shown to have better performance than other models [34], are used for the 2-D and 3-D flow calculations. The weighting factor and discrete velocity set for these two models are given below.

D2Q9:

$$\mathbf{e}_\alpha = \begin{cases} (0,0), & \alpha = 0; \\ (\pm 1,0)c, (0,\pm 1)c, & \alpha = 1,2,3,4; \\ (\pm 1,\pm 1)c, & \alpha = 5,6,7,8. \end{cases} \quad (1.7a)$$

$$w_\alpha = \begin{cases} 4/9, & \alpha = 0; \\ 1/9, & \alpha = 1,2,3,4; \\ 1/36, & \alpha = 5,6,7,8. \end{cases} \quad (1.7b)$$

D3Q19:

$$\mathbf{e}_\alpha = \begin{cases} (0,0,0), & \alpha = 0; \\ (\pm 1,0,0)c, (0,\pm 1,0)c, (0,0,\pm 1)c, & \alpha = 1,2,\dots,6; \\ (\pm 1,\pm 1,0)c, (\pm 1,0,\pm 1)c, (0,\pm 1,\pm 1)c, & \alpha = 7,8,\dots,18. \end{cases} \quad (1.8a)$$

$$w_\alpha = \begin{cases} 1/3, & \alpha = 0; \\ 1/18, & \alpha = 1,2,\dots,6; \\ 1/36, & \alpha = 7,8,\dots,18. \end{cases} \quad (1.8b)$$

With the momentum space discretized, the local mass density ρ and the local momentum density $\rho \mathbf{u}$ can be evaluated as:

$$\rho = \sum_{\alpha=0}^N f_\alpha = \sum_{\alpha=0}^N f_\alpha^{(eq)} \quad (1.9a)$$

$$\rho \mathbf{u} = \sum_{\alpha=0}^N f_\alpha \mathbf{e}_\alpha = \sum_{\alpha=0}^N f_\alpha^{(eq)} \mathbf{e}_\alpha \quad (1.9b)$$

The speed of sound in both the D2Q9 and D3Q19 models is $c_s = c/\sqrt{3}$, and the equation of state for both models is that of an ideal gas:

$$p = \rho c_s^2 \quad (1.10)$$

Equation (1.5) can be further discretized in physical space, \mathbf{x} , and time, t . The completely discretized form of Eq. (1.5) is:

$$f_\alpha(\mathbf{x} + \mathbf{e}_\alpha \delta t, t + \delta t) = f_\alpha(\mathbf{x}, t) - \frac{1}{\tau} [f_\alpha(\mathbf{x}, t) - f_\alpha^{(eq)}(\mathbf{x}, t)] \quad (1.11)$$

where $\tau = \lambda / \delta t$ is the non-dimensional relaxation time. The above equation is the discrete lattice Boltzmann equation with the BGK approximation and is known as the LBGK model. Since only one relaxation time is used in the model, this model belongs to the single relaxation time (SRT) model. There are also multiple-relaxation-time (MRT) models used in literature [35]. Eq. (1.11) is often solved in the following two steps:

$$\text{Collision step: } \tilde{f}_\alpha(\mathbf{x}, t) = f_\alpha(\mathbf{x}, t) - \frac{1}{\tau} [f_\alpha(\mathbf{x}, t) - f_\alpha^{(eq)}(\mathbf{x}, t)] \quad (1.12a)$$

$$\text{Streaming step: } f_\alpha(\mathbf{x} + \mathbf{e}_\alpha \delta t, t + \delta t) = \tilde{f}_\alpha(\mathbf{x}, t) \quad (1.12b)$$

where f_α and \tilde{f}_α denote the pre- and post-collision state of the distribution function, respectively. From Eq. (1.12), we can see that the collision step is purely local, and the streaming step is a uniform data shifting and requires little computational effort. Eq. (1.12) is explicit, easy to implement, and straightforward for parallel computation.

The viscosity in the macroscopic N-S equations can be derived from Eq. (1.11) as:

$$\nu = \left(\tau - \frac{1}{2}\right) c_s^2 \delta t \quad (1.13)$$

This choice of the viscosity makes the LBGK scheme a second order method in solving incompressible flows [31]. According to Eq. (1.13), the positivity of the viscosity requires that $\tau > 1/2$.

The differences between the LBE method and the N-S equation solver are as follows:

1. The N-S equations are second-order PDEs (macroscopic equations); the discrete velocity model from which the LBE model is derived consists of a set of first-order PDEs (kinetic equations).
2. The N-S solver must deal with nonlinear convective terms; in the LBE model the convection terms are linear and handled by simple advection (uniform data shifting).
3. For incompressible flow, the N-S solver needs to solve the Poisson equation for the pressure, which involves global data communication. In the LBE method, pressure is obtained through an equation of state and data communication is always local.
4. Usually in the LBE method, the grid Courant-Friedrichs-Lewy (CFL) number is equal to 1, based on the lattice units of $\delta x = \delta t = 1$. Also, the coupling between the discretized momentum space and physical space leads to regular square grids.
5. Due to the kinetic nature of the Boltzmann equation, the physics associated with the molecular level interaction can be incorporated more easily in the LBE model.
6. For boundary conditions (BCs), in the LBE model there is no counterpart of the BCs found in a continuum framework, e.g. no-slip at the wall. Thus the BCs in LBE model need to be developed.
7. The N-S solver usually employs iterative procedures to obtain a converged solution; the LBE models are usually explicit and don't need iterative procedures.

1.4 FROM THE CONTINUUM BOLTZMANN EQUATION TO THE LBE MODEL

Although historically the LBE method was derived from LGA, it was shown later by He and Luo [36, 37] that the LBE method could be derived rigorously from the kinetic theory of gases (i.e. the Boltzmann equation), which establishes LBE on a solid theoretical foundation. We will discuss their derivations in this section and in Appendix A.

We start from the Boltzmann equation with the BGK approximation [Eq. (1.4)]. In Eq. (1.4), $f^{(0)}$ satisfies the Maxwell-Boltzmann distribution function:

$$f^{(0)} \equiv \frac{\rho}{(2\pi RT)^{D/2}} \exp\left(-\frac{(\boldsymbol{\xi} - \mathbf{u})^2}{2RT}\right) \quad (1.14)$$

where R is the gas constant, D is the dimension of the space, and T is the macroscopic temperature. The hydrodynamic variables are the moments of the distribution function f :

$$\rho = \int f d\boldsymbol{\xi} = \int f^{(0)} d\boldsymbol{\xi}, \quad \rho \mathbf{u} = \int \boldsymbol{\xi} f d\boldsymbol{\xi} = \int \boldsymbol{\xi} f^{(0)} d\boldsymbol{\xi}, \quad \rho \varepsilon = \frac{1}{2} \int (\boldsymbol{\xi} - \mathbf{u})^2 f d\boldsymbol{\xi} = \int (\boldsymbol{\xi} - \mathbf{u})^2 f^{(0)} d\boldsymbol{\xi} \quad (1.15)$$

where $\varepsilon = \frac{1}{2} D_0 RT$ and D_0 is the number of the degrees of freedom of a particle.

Integrating Eq. (1.4) over a time interval δt , we find:

$$f(\mathbf{x} + \boldsymbol{\xi} \delta t, \boldsymbol{\xi}, t + \delta t) = e^{-\delta t / \lambda} f(\mathbf{x}, \boldsymbol{\xi}, t) + \frac{1}{\lambda} e^{-\delta t / \lambda} \int_0^{\delta t} e^{t' / \lambda} f^{(0)}(\mathbf{x} + \boldsymbol{\xi} t', \boldsymbol{\xi}, t + t') dt' \quad (1.16)$$

Assuming that δt is relatively small and g is locally smooth, and further neglecting the terms of $O(\delta t^2)$ or higher on the right hand side (RHS) of Eq. (1.16), we obtain:

$$f(\mathbf{x} + \boldsymbol{\xi} \delta t, \boldsymbol{\xi}, t + \delta t) - f(\mathbf{x}, \boldsymbol{\xi}, t) = -\frac{1}{\tau} [f(\mathbf{x}, \boldsymbol{\xi}, t) - f^{(0)}(\mathbf{x}, \boldsymbol{\xi}, t)] \quad (1.17)$$

Next, we expand the equilibrium distribution $f^{(0)}$ as a Taylor series in \mathbf{u} :

$$f^{(0)} = \frac{\rho}{(2\pi RT)^{D/2}} \exp\left(-\frac{\xi^2}{2RT}\right) \left[1 + \frac{(\xi \cdot \mathbf{u})^2}{RT} + \frac{(\xi \cdot \mathbf{u})^2}{2(RT)^2} - \frac{\mathbf{u}^2}{2RT} \right] + O(\mathbf{u}^3) \quad (1.18)$$

In order to derive the N-S equations, the second order expansion is enough, so we denote:

$$f^{(eq)} = \frac{\rho}{(2\pi RT)^{D/2}} \exp\left(-\frac{\xi^2}{2RT}\right) \left[1 + \frac{(\xi \cdot \mathbf{u})^2}{RT} + \frac{(\xi \cdot \mathbf{u})^2}{2(RT)^2} - \frac{\mathbf{u}^2}{2RT} \right] \quad (1.19)$$

and we will use $f^{(eq)}$ instead of $f^{(0)}$ in the following calculations.

To numerically evaluate the hydrodynamic variables in Eq. (1.15), we need to discretize the momentum space ξ properly. With an appropriately discretized momentum space, integration in Eq. (1.15) can be approximated by quadrature up to a certain degree of accuracy, i.e.:

$$\rho = \sum_{\alpha} f_{\alpha} = \sum_{\alpha} f_{\alpha}^{(eq)}, \quad \rho \mathbf{u} = \sum_{\alpha} \xi_{\alpha} f_{\alpha} = \sum_{\alpha} \xi_{\alpha} f_{\alpha}^{(eq)}, \quad \rho \varepsilon = \frac{1}{2} \sum_{\alpha} (\xi_{\alpha} - \mathbf{u})^2 f_{\alpha} = \frac{1}{2} \sum_{\alpha} (\xi_{\alpha} - \mathbf{u})^2 f_{\alpha}^{(eq)} \quad (1.20)$$

where

$$f_{\alpha} \equiv f_{\alpha}(\mathbf{x}, t) \equiv W_{\alpha} f(\mathbf{x}, \xi_{\alpha}, t), \quad f_{\alpha}^{(eq)} \equiv f_{\alpha}^{(eq)}(\mathbf{x}, t) \equiv W_{\alpha} f^{(eq)}(\mathbf{x}, \xi_{\alpha}, t) \quad (1.21)$$

W_{α} is the weight coefficient of the quadrature and ξ_{α} is the discrete velocity set.

The above approximation process can be written in the following general form:

$$\int \psi(\xi) f^{(eq)}(\mathbf{x}, \xi, t) d\xi = \sum_{\alpha} W_{\alpha} \psi(\xi_{\alpha}) f^{(eq)}(\mathbf{x}, \xi_{\alpha}, t) \quad (1.22)$$

where $\psi(\xi)$ is the polynomial of ξ . The above integral has the following common part, which can be evaluated by a Gaussian-type quadrature [38]:

$$I = \int \exp\left(-\frac{\xi^2}{2RT}\right) \psi(\xi) d\xi = \sum_{\alpha} W_{\alpha} \exp\left(-\frac{\xi_{\alpha}^2}{2RT}\right) \psi(\xi_{\alpha}) \quad (1.23)$$

We next need to discretize the phase space so that the evolution equation, i.e. Eq. (1.17), can be numerically evaluated over a discretized physical phase space and time. In doing this, we need to consider two factors. First, the discretized momentum space is coupled to that of physical space such that a lattice structure is obtained. Second, a lattice with necessary symmetries is required to satisfy the conservation constraints in Eq. (1.20) and also to retain the N-S equations. We use the D2Q9 model to illustrate the derivation of the LBE models.

A Cartesian coordinate system is used to recover the D2Q9 model. Therefore, we can set: $\psi(\xi) = \xi_x^m \xi_y^n$, where ξ_x and ξ_y are the x and y components of ξ . The integral in Eq. (1.23) can then be written as:

$$I = (\sqrt{2RT})^{(m+n+2)} I_m I_n \quad (1.24)$$

where

$$I_m = \int_{-\infty}^{+\infty} e^{-\zeta^2} \zeta^m d\zeta, \quad \zeta = \xi_x / \sqrt{2RT} \text{ or } \zeta = \xi_y / \sqrt{2RT} \quad (1.25)$$

For the purpose of deriving the D2Q9 model, a third-order Hermite formula [25] is used to

evaluate I_m , i.e. $I_m = \sum_{j=1}^3 \omega_j \zeta_j^m$. The three abscissas of the quadrature are:

$$\xi_1 = -\sqrt{3/2}, \quad \xi_2 = 0, \quad \xi_3 = \sqrt{3/2} \quad (1.26)$$

and the corresponding weight coefficients are:

$$\omega_1 = \sqrt{\pi}/6, \quad \omega_2 = 2\sqrt{\pi}/3, \quad \omega_3 = \sqrt{\pi}/6 \quad (1.27)$$

Then the integral in Eq. (1.24) becomes:

$$I = 2RT \omega_2^2 \psi(\mathbf{0}) + \sum_{\alpha=1}^4 \omega_1 \omega_2 \psi(\xi_\alpha) + \sum_{\alpha=5}^8 \omega_1^2 \psi(\xi_\alpha) \quad (1.28)$$

where ξ_α is the discrete velocity set with a zero-velocity vector for $\alpha = 0$, vectors of $\sqrt{3RT}(\pm 1, 0)$ and $\sqrt{3RT}(0, \pm 1)$ for $\alpha = 1-4$, and $\sqrt{3RT}(\pm 1, \pm 1)$ for $\alpha = 5-8$. After the momentum space is discretized with these nine discrete velocities, the physical space needs to be discretized accordingly. This means that the physical space is discretized into a square lattice space with a lattice constant $\delta x = \sqrt{3RT}\delta t$. If we only deal with the isothermal model, then the temperature T has no physical significance here. Thus we can pick δx to be a fundamental quantity, i.e. $\sqrt{3RT} = c \equiv \frac{\delta x}{\delta t}$, or $RT = c_s^2 = \frac{1}{3}c^2$, where c_s is called the sound speed of the model, and c is the lattice speed. Usually the lattice speed is fixed as 1, so for the D2Q9 model, $c_s^2 = 1/3$.

Comparing Eq. (1.23) and Eq. (1.28), we can identify the weights in Eq. (1.23) as:

$$W_\alpha = 2\pi RT \exp\left(\frac{\xi_\alpha^2}{2RT}\right) w_\alpha \quad (1.29)$$

where w_α is the same as given in Eq. (1.7b).

Then the equilibrium distribution function of the D2Q9 model is:

$$f_\alpha^{(eq)} = W_\alpha f^{(eq)}(\mathbf{x}, \xi_\alpha, t) = w_\alpha \rho \left[1 + \frac{3(\mathbf{e}_\alpha \cdot \mathbf{u})}{c^2} + \frac{9(\mathbf{e}_\alpha \cdot \mathbf{u})^2}{2c^4} - \frac{3\mathbf{u}^2}{2c^2} \right] \quad (1.30)$$

where \mathbf{e}_α is the same as given in Eq. (1.7a). The evolution equation [Eq. (1.17)] is then finally discretized to Eq. (1.11) and can be solved numerically. Models for the other lattice configurations (D2Q7, D3Q27) can be derived in a similar manner [37].

2.0 IMPROVEMENT OF BOUNDARY TREATMENT IN THE LBE METHOD

2.1 INTRODUCTION

In the previous chapter, the role of boundary conditions (BCs) was not discussed. However, to some extent, developing accurate and efficient BCs is as important as developing an accurate computation scheme itself, since they will influence the accuracy and stability of the computation [39, 40, 41]. We will discuss two classes of boundaries encountered in the LBE simulation: the open boundary and the solid wall boundary. In practice, the solid wall boundary conditions are usually more important than the open boundary conditions, and are also much harder to incorporate. Therefore, we will put more emphasis on them in the following sections. In this chapter, we will first briefly introduce several commonly used open boundary conditions. Next, we will discuss the development of solid wall boundary conditions and finally propose our improved mass conserving solid wall boundary condition together with benchmark test results.

2.2 THE OPEN BOUNDARY CONDITION

Open boundaries denote inlets/outlets, periodical boundaries, lines of symmetry and infinity. The commonly used open boundary conditions are introduced in this section.

2.2.1 Periodical boundary condition

The periodical BC is the easiest BC. The periodical BC is applied directly to the PDFs, and not to the macroscopic flow variables, which means the PDFs coming out of one boundary will enter into the opposite boundary. In most early papers, the periodical BC was used together with the bounce-back wall boundary condition (discuss in section 2.3).

The periodical BC can be used as an inflow/outflow BC in the streamwise direction. For example, with the periodical BCs at the inlet and outlet, the uniform body force or constant pressure gradient can be included in the simulation procedure after the collision step, which is expressed as follows:

$$\tilde{f}_{\alpha_inlet} = \tilde{f}_{\alpha_outlet} - w_{\alpha} \frac{3}{c^2} \frac{dp}{dx} \mathbf{e}_{\alpha} \cdot \bar{\mathbf{x}} \quad (2.1)$$

where $\frac{dp}{dx}$ is the constant pressure gradient, $\bar{\mathbf{x}}$ is the unit vector in the \mathbf{x} (streamwise) direction,

α denotes the direction of the unknown PDF, and \sim denotes the post-collision state here and hereafter.

2.2.2 Extrapolation boundary condition

Besides the periodical BC, we can use the zero derivative condition for an inflow/outflow boundary. Supposing $i = 1$ is the inlet boundary and $i = nx$ is the outlet boundary, in the 2-D case, the zero derivative condition can be expressed in the following form:

$$\tilde{f}_{\alpha}(i = 1, j) = \tilde{f}_{\alpha}(i = 2, j) \quad (2.2a)$$

$$\tilde{f}_{\alpha}(i = nx, j) = \tilde{f}_{\alpha}(i = nx - 1, j) \quad (2.2b)$$

In some instances, we can use extrapolation to find PDFs at the inflow/outflow boundary; e.g, instead of using Eq. (2.1), the following simple extrapolation can be used:

$$\tilde{f}_\alpha(i=1, j) = 2\tilde{f}_\alpha(i=2, j) - \tilde{f}_\alpha(i=3, j) \quad (2.3a)$$

$$\tilde{f}_\alpha(i=nx, j) = 2\tilde{f}_\alpha(i=nx-1, j) - \tilde{f}_\alpha(i=nx-2, j) \quad (2.3b)$$

2.2.3 Bounce-back and other boundary conditions for the inlet

Based on the bounce-back of the PDFs or non-equilibrium part of the PDFs, different approaches [42, 43] have been proposed to obtain the PDFs at the inlet, from which the specified velocity or pressure can be recovered. In these approaches, usually the inlet boundary is placed half way between the inlet boundary node and the first fluid node as shown in Figure 2.1. If the velocity profile is known at the inlet, the standard bounce-back scheme for unknown PDFs at the inlet yields:

$$\tilde{f}_{\bar{\alpha}}_{inlet} = \tilde{f}_\alpha + 2w_\alpha \rho_{internal} \frac{3}{c^2} \mathbf{e}_{\bar{\alpha}} \cdot \mathbf{u}_{inlet} \quad (2.4)$$

where w_α is the weighting factor; and \mathbf{e}_α and $\mathbf{e}_{\bar{\alpha}}$ denote directions opposite to each other: $\mathbf{e}_\alpha = -\mathbf{e}_{\bar{\alpha}}$. We use this notation hereafter.

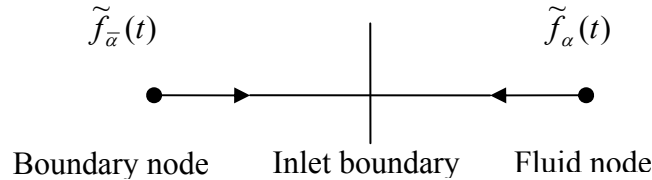


Figure 2.1: Layout of the inlet boundary.

Grunau [44] placed the inlet at the boundary node and assigned an equilibrium distribution function to be the desired $\tilde{f}_{\bar{\alpha}}(t)$ at the inlet. For the D2Q9 model, this gives:

$$\tilde{f}_{\bar{\alpha}_{inlet}} = f_{\alpha}^{eq} = w_{\alpha} \rho_{inlet} \left[1 + \frac{3}{c^2} \mathbf{e}_{\alpha} \cdot \mathbf{u}_{inlet} + \frac{9}{2c^4} (\mathbf{e}_{\alpha} \cdot \mathbf{u}_{inlet})^2 - \frac{3}{2c^2} \mathbf{u}_{inlet}^2 \right] \quad (2.5)$$

However, this method was reported to have a bigger error than the standard bounce-back scheme [43].

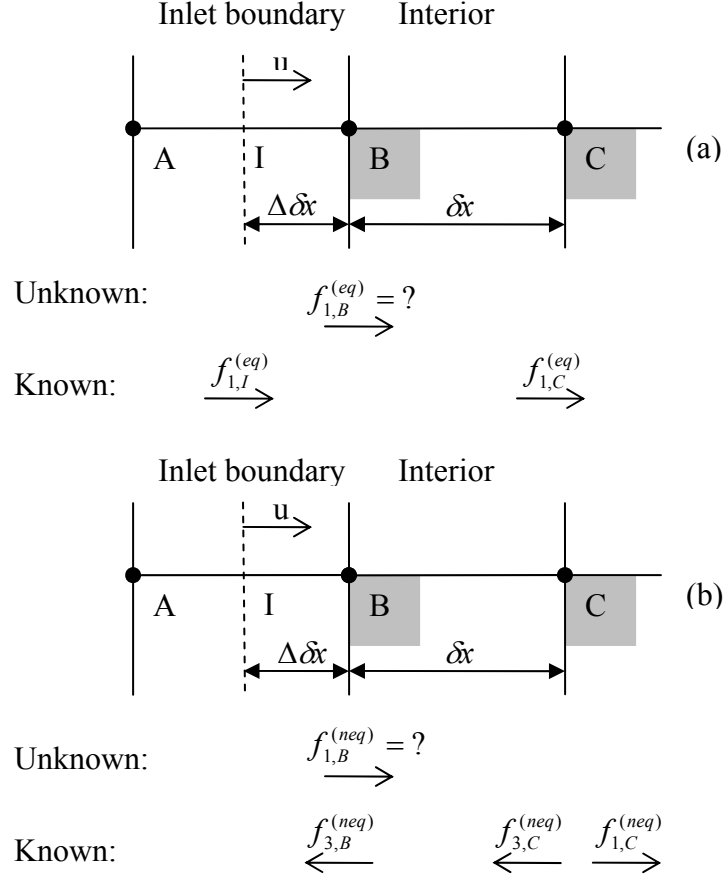


Figure 2.2: Configuration of PDFs used to construct the inlet boundary condition: (a) Configuration of equilibrium PDFs at the inlet, (b) Configuration of non-equilibrium PDFs at the inlet (the gray color denotes a fluid node).

Recently, Yu [45] proposed a new boundary treatment for the inlet boundary. In this approach, the unknown PDFs at the inlet were decomposed to an equilibrium part and non-equilibrium part and then computed separately, i.e. $\tilde{f}_{\bar{\alpha}_{inlet}} = f_{\bar{\alpha}_{inlet}}^{(eq)} + f_{\bar{\alpha}_{inlet}}^{(neq)}$. To illustrate how to numerically construct the $f_{\bar{\alpha}_{inlet}}^{(eq)}$ and $f_{\bar{\alpha}_{inlet}}^{(neq)}$, an 1-D example is shown in Figure 2.2. In Yu's

approach, by using linear interpolation and setting $f_{3,I}^{(neq)} = f_{3,B}^{(neq)}$ the unknown PDF can be obtained:

$$f_{1,B}^{(eq)} = f_{1,I}^{(eq)} + \frac{\Delta}{1+\Delta} [f_{1,C}^{(eq)} - f_{1,I}^{(eq)}] \quad (2.6a)$$

$$f_{1,B}^{(neq)} = f_{1,I}^{(neq)} + \frac{\Delta}{1+\Delta} [f_{1,C}^{(neq)} - f_{1,I}^{(neq)}] \quad (2.6b)$$

2.3 WALL BOUNDARY CONDITIONS

The most common and simplest solid wall boundary condition is the bounce-back boundary condition. In this boundary condition, when a particle distribution streams to a wall node, it scatters back to the fluid node along its incoming link. However, the bounce-back boundary condition only gives first order numerical accuracy, which means the lowest-order term in the truncation error is first order. To improve it, many boundary conditions have been proposed in the past [46, 47]. Among them, the halfway bounce-back scheme [26, 27, 48] is easy to implement and gives second-order accuracy for straight walls. The boundary condition proposed by Mei *et. al.* [49, 50] has the ability to handle complex geometries, e.g. a curved boundary.

2.3.1 Fullway and halfway bounce-back wall boundary conditions

The no-slip wall BC is widely used in traditional CFD methods. However, there is no corresponding counterpart for kinetic equations. Historically, the LBE method directly adopted a wall BC from the LGA, which resulted in the so-called fullway bounce-back condition. In the fullway bounce-back scheme, when a fluid particle collides with a wall node, it will scatter back to the fluid nodes along its incoming direction, i.e. $f_{\alpha}^{out} = f_{\alpha}^{in}$, where f_{α}^{in} is the PDF entering

the boundary site, f^{out} is the PDF leaving the boundary site, and α and $\bar{\alpha}$ denote directions opposite to each other. The Fullway bounce-back BC is very simple and leads to mass and momentum conservation. However, the fullway bounce-back BC only gives first order accuracy at the boundaries. The LBE method itself is a second-order scheme, therefore using the fullway bounce-back BC will deteriorate the simulation results. Notice that in practice the order of accuracy can also be obtained by measuring the slope of relative L_2 -norm error (see Eq. (2.21)). We will discuss this in section 2.3.4.3.

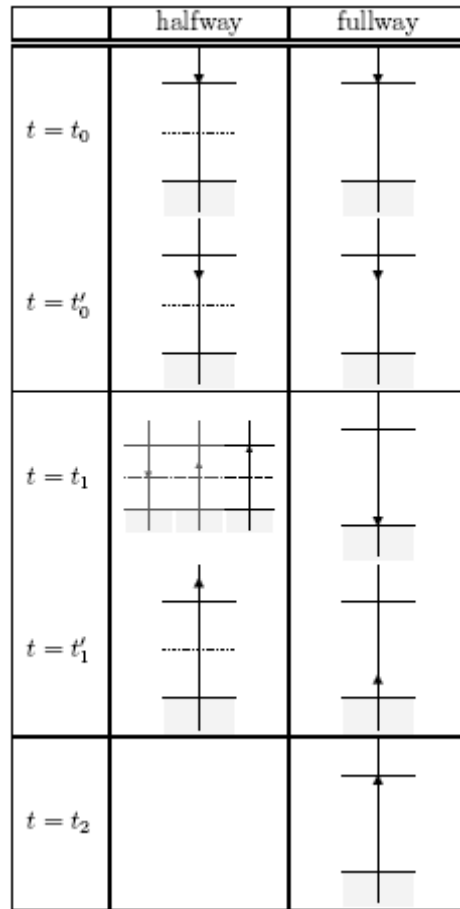


Figure 2.3: Illustration of fullway and halfway bounce-back boundary conditions. t_i denotes a time step after a propagation process and t'_i denotes the time after the application of the boundary condition. The gray color represents the boundary nodes (after [51]).

In order to achieve second order accuracy, several BCs have been proposed, such as the extrapolation scheme [42], bounce-back of the non-equilibrium distribution [43], etc. It was also shown that second order accuracy in space could be obtained by using the halfway bounce-back scheme. In this scheme the wall is placed at halfway between a fluid node and a bounce-back node. Compared with other second order boundary treatments, halfway bounce-back doesn't need any extrapolation and is easy to implement. Figure 2.3 shows the application procedure of both the fullway and halfway bounce-back BC. For the halfway bounce-back BC, in only one time step a fluid particle goes to the boundary site, reverses its velocity and comes back, while the fullway bounce-back condition needs two time steps to go forth and back.

2.3.2 Solid wall boundary conditions for a curved boundary

Although the halfway bounce-back BC gives second order accuracy and is very easy to implement, it encounters problems when dealing with a curved boundary where one can no longer keep the wall boundary halfway between the lattice nodes. In order to solve this difficulty, several curved boundary treatments have been proposed, among which the unified BC proposed by Mei, Luo and Shyy (MLS) [49, 50] is the simplest to implement and can also handle different BCs, e.g. moving boundary.

MLS's BC is a revised version of the boundary treatment proposed by Filippova and Hänel (FH) [52]. We will discuss both of them here. As shown in Figure 2.4, \mathbf{e}_α and $\mathbf{e}_{\bar{\alpha}}$ denote directions opposite to each other, \mathbf{x}_b is a boundary node, and \mathbf{x}_f is a fluid node. The curved wall

is located between a boundary node and fluid node, with $\Delta = \frac{|\mathbf{x}_f - \mathbf{x}_w|}{|\mathbf{x}_f - \mathbf{x}_b|}$ denoting the fraction of

an intersected link in the fluid region. Obviously, $0 \leq \Delta \leq 1$. In order to finish the streaming step, we need to know $\tilde{f}_{\bar{\alpha}}(\mathbf{x}_b, t)$ at boundary node \mathbf{x}_b .

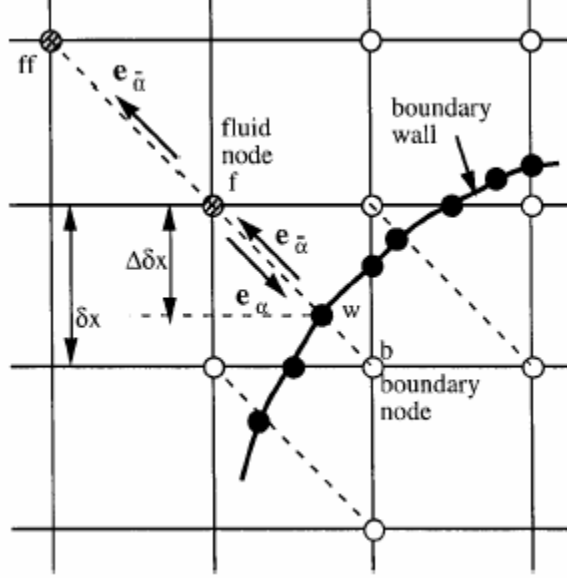


Figure 2.4: Layout of the lattice and curved wall boundary (after [49]).

FH proposed the following treatment for $\tilde{f}_{\bar{\alpha}}(\mathbf{x}_b, t)$ on curved boundaries:

$$\tilde{f}_{\bar{\alpha}}(\mathbf{x}_b, t) = (1 - \chi)\tilde{f}_{\alpha}(\mathbf{x}_f, t) + \chi f_{\alpha}^{(*)}(\mathbf{x}_b, t) + 2w_{\alpha}\rho \frac{3}{c^2} \mathbf{e}_{\bar{\alpha}} \cdot \mathbf{u}_w \quad (2.7)$$

where $\mathbf{u}_w \equiv \mathbf{u}(\mathbf{x}_w, t)$ is the velocity at the wall, χ is the weighting factor that controls the linear interpolation between $\tilde{f}_{\alpha}(\mathbf{x}_f, t)$ and $f_{\alpha}^{(*)}(\mathbf{x}_b, t)$, and $f_{\alpha}^{(*)}(\mathbf{x}_b, t)$ is given by a fictitious equilibrium distribution:

$$f_{\alpha}^{(*)}(\mathbf{x}_b, t) = w_{\alpha}\rho(\mathbf{x}_f, t) \left[1 + \frac{3}{c^2} \mathbf{e}_{\alpha} \cdot \mathbf{u}_{bf} + \frac{9}{2c^4} (\mathbf{e}_{\alpha} \cdot \mathbf{u}_f)^2 - \frac{3}{2c^2} \mathbf{u}_f \cdot \mathbf{u}_f \right] \quad (2.8)$$

In Eq. (2.8), $\mathbf{u}_f \equiv \mathbf{u}(\mathbf{x}_f, t)$ is the fluid velocity near the wall, \mathbf{u}_{bf} is to be chosen, and the weighting factor χ depends on how \mathbf{u}_{bf} is chosen. In FH's original paper, the following combination of \mathbf{u}_{bf} and χ was given:

$$\mathbf{u}_{bf} = (\Delta - 1)\mathbf{u}_f / \Delta + \mathbf{u}_w / \Delta \quad \text{and} \quad \chi = (2\Delta - 1) / \tau \quad \text{for } \Delta \geq 1/2 \quad (2.9a)$$

$$\mathbf{u}_{bf} = \mathbf{u}_f \quad \text{and} \quad \chi = (2\Delta - 1) / (\tau - 1) \quad \text{for } \Delta < 1/2 \quad (2.9b)$$

In order to improve the stability of the scheme, MLS revised the expression for \mathbf{u}_{bf} and χ to the following form:

$$\mathbf{u}_{bf} = [1 - 3/(2\Delta)]\mathbf{u}_f + 3/(2\Delta)\mathbf{u}_w \quad \text{and} \quad \chi = (2\Delta - 1) / (\tau + 1/2) \quad \text{for } \Delta \geq 1/2 \quad (2.10a)$$

$$\mathbf{u}_{bf} = \mathbf{u}_{ff} = \mathbf{u}_f(\mathbf{x}_f + \mathbf{e}_{\bar{\alpha}}\delta t, t) \quad \text{and} \quad \chi = (2\Delta - 1) / (\tau - 2) \quad \text{for } \Delta < 1/2 \quad (2.10b)$$

We can see that these boundary treatments can handle curved boundaries as well as moving boundaries.

2.3.3 Slip velocity for different wall boundary conditions

Theoretically, the “non-slip” boundary condition should be maintained at the solid wall boundary, which means that fluid molecules immediately at the surface of a solid move with exactly the same velocity as that solid. However, in the LBE simulation, all the above mentioned BCs will generate slip velocities at the wall boundary. He [53, 54] *et al.* analyzed the slip velocity of simple flows for different BCs. They showed both theoretically and numerically that for Poiseuille flow, the fullway bounce-back scheme generates a slip velocity which is equal to:

$$u_s = \frac{2u_c}{3n^2} [(2\tau - 1)(4\tau - 3) - 3n] \quad (2.11a)$$

The halfway bounce-back scheme generates a slip velocity which is equal to:

$$u_s = \frac{u_c}{3(n-1)^2} [4\tau(4\tau-5) + 3] \quad (2.11b)$$

where u_c is the centerline velocity, τ is the relaxation time and n is lattice resolution in the width of the channel. The channel width is $H = n\delta x$ for the fullway bounce-back scheme and $H = (n-1)\delta x$ for the halfway bounce-back scheme.

From Eq. (2.11), we can see that for the fullway bounce-back scheme the slip velocity is first order in space because it has a term of $O(1/n)$ and for the halfway bounce-back scheme the slip velocity is second order since all the terms of the slip velocity are on at the order of $O(1/(n-1)^2)$. He also showed in his paper that the above conclusion holds for other simple flows, like plane Couette flow.

MLS didn't analyze the slip velocity generated by their scheme. Following He's method, we conducted simulations of Poiseuille flow to determine the slip velocity generated by MLS's BC. In simulation, wall boundaries are placed at $y = \pm H/2$ ($\Delta = 1$) and the body force in the x direction is set to be $\mathbf{F} = \rho G \mathbf{i}$. Then the centerline velocity is $u_c = \frac{H^2 G}{8\nu}$. Suppose the slip velocity is $u_s = \alpha G$. Figure 2.5(a) gives the relation between α and τ . Figure 2.5(b) shows that

$\alpha \propto \frac{\tau(5-4\tau)}{6\nu}$. We try to formulate the slip velocity in the form of Eq. (2.11). We found that

$$\alpha = \frac{\tau(5-4\tau)}{2\tau-1} = \frac{\tau(5-4\tau)}{6\nu}. \text{ Therefore, } u_s = \frac{\tau(5-4\tau)}{6\nu} G = \frac{H^2 G}{8\nu} \frac{8}{H^2} \frac{\tau(5-4\tau)}{6} = \frac{u_c}{3H^2} [4\tau(4\tau-5)],$$

or $u_s = \frac{u_c}{3n^2} [4\tau(4\tau-5)]$, which is also second order in space and quite close to the slip velocity

of the halfway bounce-back scheme.

Notice that for a fixed lattice size, the error (slip velocity) goes to infinite as $\tau \rightarrow \infty$. However, for practical purposes, there is no need to take a large value of τ in a simulation. In fact, the factor $4\tau(4\tau - 5)$ in the error expression has a maximal absolute value of only -6.25 (when $\tau = 0.625$) for $0.5 < \tau \leq 1.25$. Then, if the lattice size is 40, the slip velocity is about 0.13% of the maximum velocity.

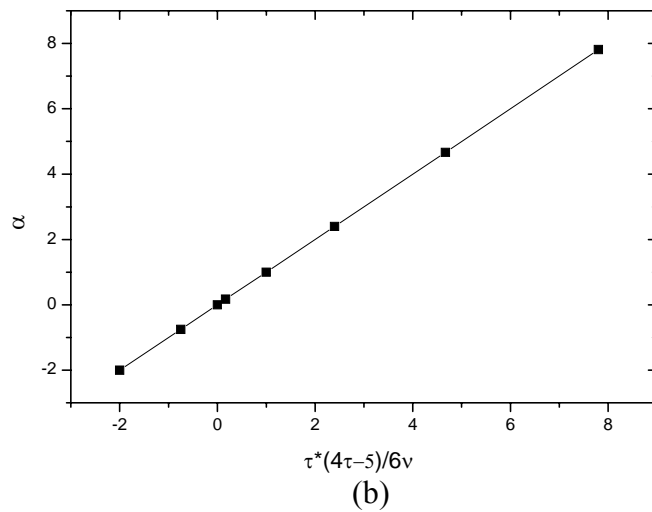
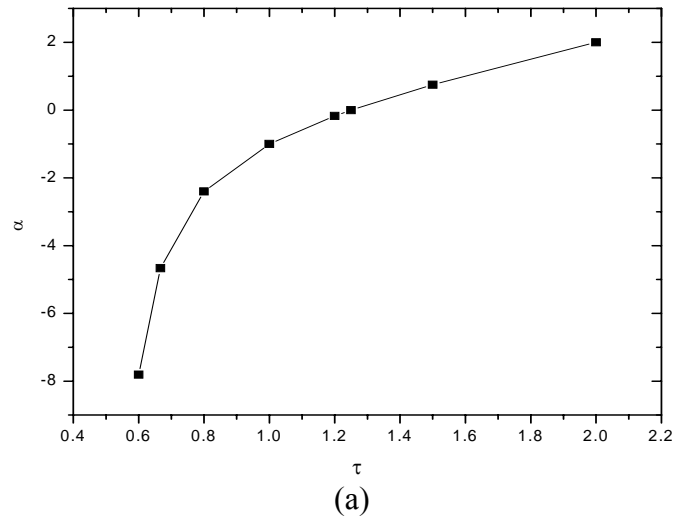


Figure 2.5: Relation between α and τ .

2.3.4 Mass conserving solid wall boundary condition

In this subsection, we will describe the drawbacks of FH & MLS's BC and give our remedy, i.e. our new mass conserving solid wall BC. We will show the advantage of our new BC by several benchmark tests.

2.3.4.1 Drawbacks of FH & MLS's BC Usually in the LBE simulation, the mass of the system is not conserved exactly. There will be mass loss/gain at each time step during the beginning stage of the simulation, which is the so-called “mass leakage” in the literature. Since in most cases the leakage is very small and it eventually approaches zero with enough time steps, as shown in Figure 2.6, therefore its effect on the simulation results can be neglected. However, under some circumstances, this mass leakage becomes no longer small and will affect the simulation result.

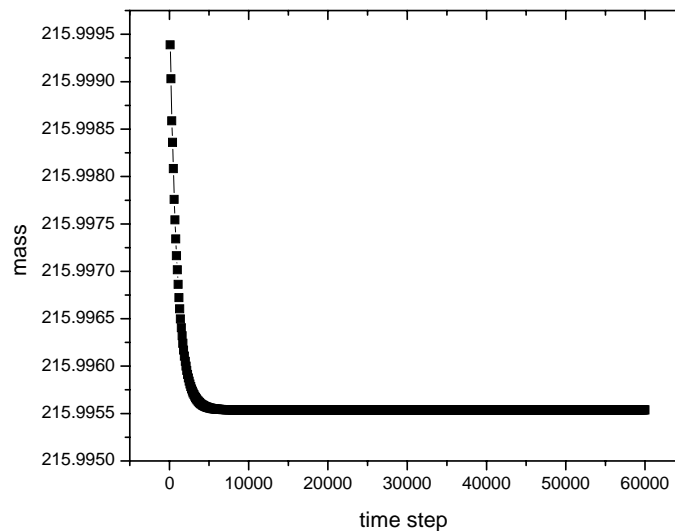


Figure 2.6: System mass changes with time in a typical LBE simulation.

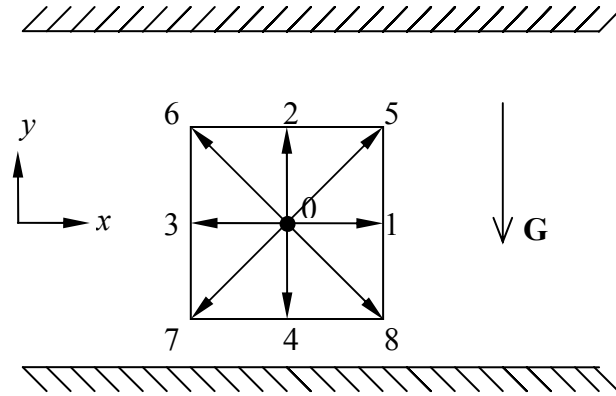


Figure 2.7: Schematic of static flow under gravity.

One simple yet very useful case to consider is static flow under gravity $\mathbf{G} = -\rho g \mathbf{j}$. Figure 2.7 shows the set up of the simulation system. We set $\Delta = 1$, $u_w = 0$, $\tau = 1$, $g = 0.001$ and set the lattice resolution to be $nx \times ny = 100 \times 50$. Using FH's BC, the system mass will keep decreasing at a constant rate as shown in Figure 2.8. Shown in Figure 2.9 is the mass changing rate (defined as: $mass|_{t+100} - mass|_t$) varying with time, which fluctuates at the beginning stage then instead of approaching to zero as in a typical LBE simulation, approaches a constant negative value.

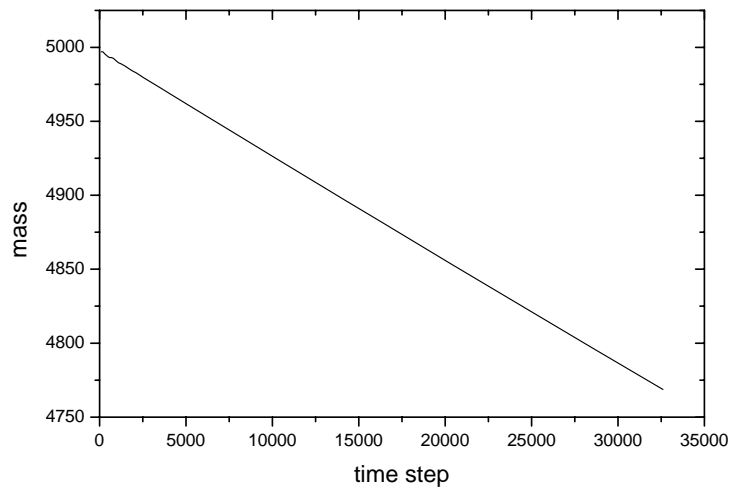


Figure 2.8: System mass changes with time using FH's BC.

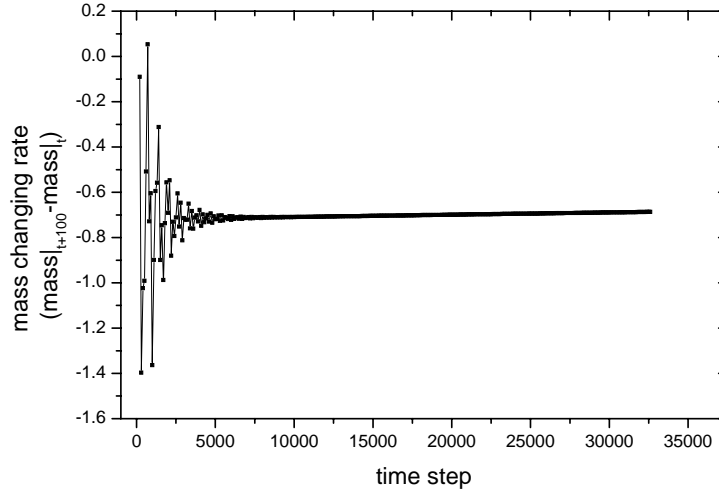


Figure 2.9: Mass changing rate varying with time.

We notice that by setting $\Delta = 1$ and $\tau = 1$, the weight coefficient $\chi = 1$, and then by setting $\mathbf{u}_w = 0$, Eq. (2.7) becomes: $\tilde{f}_{\bar{\alpha}}(\mathbf{x}_b, t) = f_{\alpha}^{(*)}(\mathbf{x}_b, t)$. Now, we consider another extreme case, i.e. setting $\Delta = 1/2$, where therefore, $\chi = 0$, which means $\tilde{f}_{\bar{\alpha}}(\mathbf{x}_b, t) = \tilde{f}_{\alpha}(\mathbf{x}_f, t)$. This time, the mass is exactly conserved. From this comparison, we can see the mass leakage is due to the $f_{\alpha}^{(*)}(\mathbf{x}_b, t)$ term itself.

Since the mass leakage results from the interchange of mass between fluid nodes and boundary nodes, to analyze it we now consider two fluid nodes next to the boundary, located at $y = 1$ and $y = ny - 1$, respectively, and only study their outgoing and incoming PDFs. There are several methods of incorporating body force into the scheme [55]. In order to simplify our analysis, we use a simple and commonly used approach -- direct body forcing. In this approach, the body force is included in the scheme after the collision step by:

$$\tilde{f}_{\alpha}(\mathbf{x}_i, t) = \tilde{f}_{\alpha}(\mathbf{x}_i, t) - w_{\alpha} \frac{3}{c^2} \rho(\mathbf{x}_i, t) g \mathbf{e}_{\alpha} \cdot \hat{\mathbf{j}} \quad (2.12)$$

For the upper fluid node at $y = ny - 1$, the outgoing PDFs are f_2 , f_5 and f_6 which are given

by:

$$\tilde{f}_2(ny-1, t) \approx \tilde{f}_2^{(eq)}(ny-1, t) - \frac{\rho(ny-1, t)g}{3c^2} \quad (2.13a)$$

$$\tilde{f}_5(ny-1, t) \approx \tilde{f}_5^{(eq)}(ny-1, t) - \frac{\rho(ny-1, t)g}{12c^2} \quad (2.13b)$$

$$\tilde{f}_6(ny-1, t) \approx \tilde{f}_6^{(eq)}(ny-1, t) - \frac{\rho(ny-1, t)g}{12c^2} \quad (2.13c)$$

In the above equations, use the “=” sign when $\tau = 1$. Similarly, for the lower fluid node at $y = 1$,

the outgoing PDFs are f_4 , f_7 and f_8 which are given by:

$$\tilde{f}_4(1, t) \approx \tilde{f}_4^{(eq)}(1, t) + \frac{\rho(1, t)g}{3c^2} \quad (2.13d)$$

$$\tilde{f}_7(1, t) \approx \tilde{f}_7^{(eq)}(1, t) + \frac{\rho(1, t)g}{12c^2} \quad (2.13e)$$

$$\tilde{f}_8(1, t) \approx \tilde{f}_8^{(eq)}(1, t) + \frac{\rho(1, t)g}{12c^2} \quad (2.13f)$$

For $\tau = 1$, the incoming PDFs are:

$$\tilde{f}_4(ny-1, t) = f_2^{(*)}(ny, t) \approx \tilde{f}_2^{(eq)}(ny-1, t) \quad (2.14a)$$

$$\tilde{f}_7(ny-1, t) = f_5^{(*)}(ny, t) \approx \tilde{f}_5^{(eq)}(ny-1, t) \quad (2.14b)$$

$$\tilde{f}_8(ny-1, t) = f_6^{(*)}(ny, t) \approx \tilde{f}_6^{(eq)}(ny-1, t) \quad (2.14c)$$

$$\tilde{f}_2(1, t) = f_4^{(*)}(0, t) \approx \tilde{f}_4^{(eq)}(1, t) \quad (2.14d)$$

$$\tilde{f}_5(1, t) = f_7^{(*)}(0, t) \approx \tilde{f}_7^{(eq)}(1, t) \quad (2.14e)$$

$$\tilde{f}_6(1, t) = f_8^{(*)}(0, t) \approx \tilde{f}_8^{(eq)}(1, t) \quad (2.14f)$$

The “ \approx ” is obtained because $f_\alpha^{(*)}(\mathbf{x}_b, t)$ is given by a fictitious equilibrium distribution, Eq. (2.8), which is in the same form of $f_\alpha^{(eq)}$ in Eq. (1.6). The only difference is that in the second term \mathbf{u}_{bf} is used instead of \mathbf{u}_f . Since $\mathbf{u}_{bf} \approx \mathbf{u}_f$ (for FH’s BC, when $\Delta < 1/2$, $\mathbf{u}_{bf} = \mathbf{u}_f$), therefore $f_\alpha^{(*)}(\mathbf{x}_b, t) \approx \tilde{f}_\alpha^{(eq)}(\mathbf{x}_f, t)$.

Then the mass leakage of one pair of fluid nodes, i.e. the upper and the lower fluid node will be:

$$\begin{aligned}
\sum_{outgoing} \tilde{f} - \sum_{incoming} \tilde{f} &= \tilde{f}_2(ny-1, t) + \tilde{f}_5(ny-1, t) + \tilde{f}_6(ny-1, t) + \tilde{f}_4(1, t) + \tilde{f}_7(1, t) + \tilde{f}_8(1, t) \\
&\quad - [\tilde{f}_4(ny-1, t) + \tilde{f}_7(ny-1, t) + \tilde{f}_8(ny-1, t) + \tilde{f}_2(1, t) - \tilde{f}_5(1, t) - \tilde{f}_6(1, t)] \\
&\approx \frac{1}{2c^2} [\rho(1, t) - \rho(ny-1, t)]g \\
&= \frac{1}{2} [\rho(1, t) - \rho(ny-1, t)]g
\end{aligned} \tag{2.15}$$

Since lattice Boltzmann fluids are intrinsically compressible, introducing gravity into the LB scheme will result to density variation in the system. The density difference between the upper and lower fluid nodes therefore produces the mass leakage. Suppose there is no density variation along the x direction, which is verified by the simulation, and also assume that the density change is small during a short time interval, say 100 time steps. Then the mass leakage of the system in this time interval can be calculated by:

$$mass\ leakage = 0.5 * (nx + 1) * time\ interval * [\rho(ny - 1) - \rho(1)]g. \tag{2.16}$$

Figure 2.10 shows the density at $x = nx/2$ as a function of height when $t = 32600$. Using Eq. (2.16), we can estimate the mass leakage during 100 time steps:

$$mass\ leakage = 0.5 * 101 * 100 * (0.887033 - 1.024421) * 0.001 = -0.6938$$

The actual mass leakage during this time interval is -0.6867 (see Figure 2.8), which is very close to our estimate, an error of 0.03%.

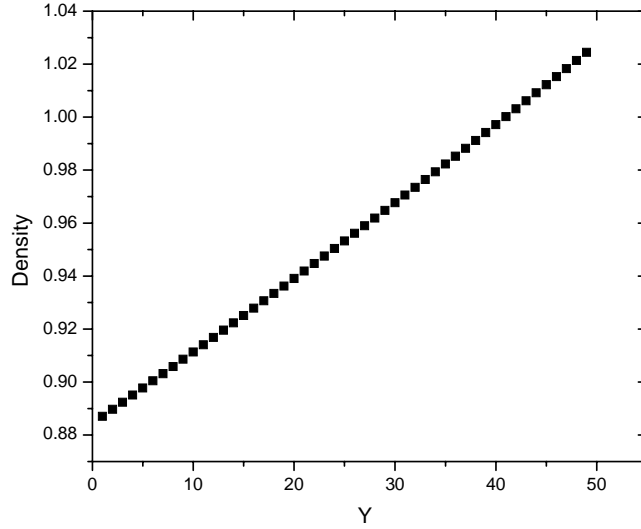


Figure 2.10: Density as a function of height at selected time.

The above discussion clearly shows that the mass leakage is due to the density variation in the system, or more precisely, due to the fact that the $f_{\alpha}^{(*)}(\mathbf{x}_b, t)$ term doesn't correctly reflect the density variation. Since $\tilde{f}_{\bar{\alpha}}(\mathbf{x}_b, t)$ is the linear combination of $\tilde{f}_{\alpha}(\mathbf{x}_f, t)$ and $f_{\alpha}^{(*)}(\mathbf{x}_b, t)$, to improve the stability of the scheme, MLS tried to change the weighting coefficients of these two terms. In the commonly used range of τ , MLS's revision produces a smaller weighting coefficient χ and therefore a better stability (as discussed later). However, under some circumstances, like the one we discussed in this subsection, MLS's BC cannot eliminate the constant mass leakage. In most cases, it can only decrease the mass changing rate, unless $\chi = 0$.

It should be emphasized here that the intensity of gravity $g = 0.001$ used in the example is quite big. Usually, in the LBE simulations, the intensity of the body force is restricted to satisfy the incompressible limit, $\mathbf{u} \ll c_s$. In this example, the common practice is to set $g * ny \ll c_s^2$, which results in a smaller density variation and a smaller mass leakage too. Meanwhile, in many

system configurations, the density variation will not produce the constant mass leakage as shown in the example, so FH & MLS's BCs are still widely used in the literature.

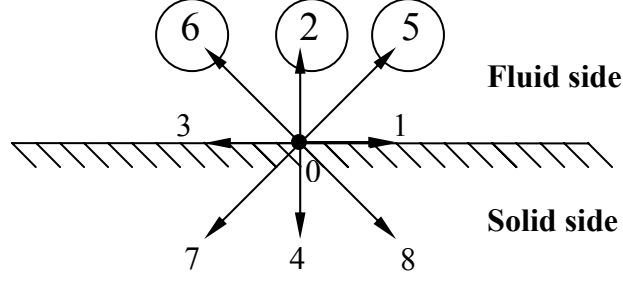
In order to eliminate the abovementioned constant mass leakage and therefore make the LBE method suitable for the flow system with small compressibility, in the next subsection we will propose a new mass conserving BC by revising MLS's BC. We will show that by using our new BC we can not only eliminate the constant mass leakage but also greatly improve the stability of the scheme.

2.3.4.2 Implementation of mass conserving solid wall BC From the above discussions we can see that a boundary condition that can preserve the total mass in a given system is very important for LBE simulations. Based on MLS's BC, we defined a new boundary condition, called the mass conserving solid wall boundary condition. The basic idea is that we still use linear interpolation between $\tilde{f}_\alpha(\mathbf{x}_f, t)$ and $f_\alpha^{(*)}(\mathbf{x}_b, t)$ (Eq. (2.12)) to find $\tilde{f}_\alpha(\mathbf{x}_b, t)$. However, we will change the density term in the expression of $f_\alpha^{(*)}(\mathbf{x}_b, t)$, (Eq. (2.13)) to guarantee the mass conservation, since the $f_\alpha^{(*)}(\mathbf{x}_b, t)$ term is responsible for the mass leakage. Therefore, we define that:

$$f_\alpha^{(*)}(\mathbf{x}_b, t) = w_\alpha \rho(\mathbf{x}_w, t) \left[1 + \frac{3}{c^2} \mathbf{e}_\alpha \cdot \mathbf{u}_{bf} + \frac{9}{2c^4} (\mathbf{e}_\alpha \cdot \mathbf{u}_f)^2 - \frac{3}{2c^2} \mathbf{u}_f \cdot \mathbf{u}_f \right] \quad (2.17)$$

where $\rho(\mathbf{x}_w, t)$ is called the wall density.

It must be determined what $\rho(\mathbf{x}_w, t)$ term guarantees the mass conservation. We discuss this in the context of D2Q9 model. Shown in Figure 2.11 are the known and unknown PDFs of a flat boundary site at the lower wall boundary after the streaming step.



Unknown (Incoming) PDFs: $f_2 = ?, f_5 = ?, f_6 = ?$

Known (Outgoing) PDFs: f_4, f_7, f_8

Figure 2.11: PDFs of a flat boundary site at the lower wall boundary after the streaming step.

The outgoing PDFs are f_4, f_7, f_8 , which are known and the incoming PDFs are f_2, f_5, f_6 , which are unknown. The mass conservation requires that $f_2 + f_5 + f_6 = f_4 + f_7 + f_8$. Assume that all the outgoing PDFs also satisfy Eq. (2.17), with an unknown $\rho(\mathbf{x}_w, t)$ term. Then summing these together, we find:

$$f_4 + f_7 + f_8 = \frac{1}{6} \rho(\mathbf{x}_w, t) (1 - 3u_{bf}^y + 3u_f^y) \quad (2.18)$$

where u_{bf}^y is the y -component of \mathbf{u}_{bf} and u_f^y is the y -component of \mathbf{u}_f . Therefore $\rho(\mathbf{x}_w, t)$ will be:

$$\rho(\mathbf{x}_w, t) = 6 \frac{f_4 + f_7 + f_8}{1 - 3u_{bf}^y + 3u_f^y} \quad (2.19)$$

Then by substituting the expression of $\rho(\mathbf{x}_w, t)$ into Eq. (2.17), the unknown PDFs f_2, f_5, f_6 can be obtained. It is straightforward to show that this boundary treatment indeed satisfies the condition: $\sum_{outgoing} f = \sum_{incoming} f$, so therefore the total mass is conserved.

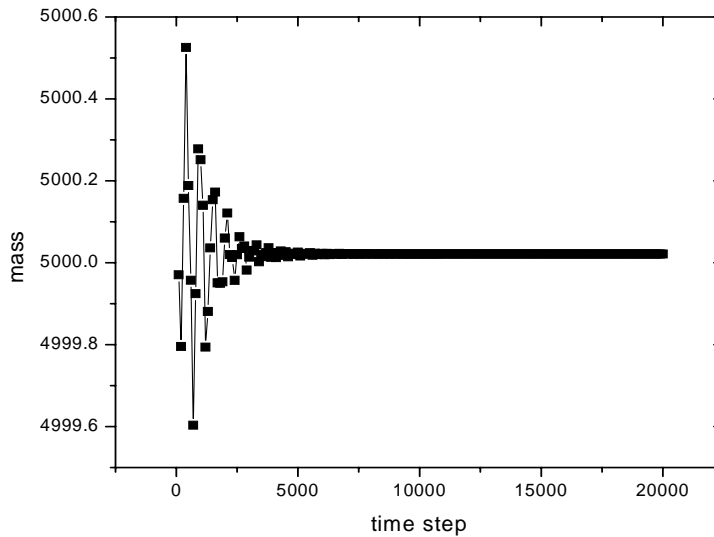


Figure 2.12: System mass changes with time using new BC.

In order to verify our new BC, simulations of the same problem specified in the previous subsection were conducted. Figure 2.12 shows the system mass change with time using the new BC. The mass of the system fluctuates at the beginning then goes to a constant value. Even at the smaller time steps, the fluctuation is very small.

The mass distribution at $x = nx/2$ when $t = 60000$ is plotted in Figure 2.13 together with simulation results obtained by using the halfway bounce-back BC and FH's BC. All three BCs give linear density distributions. Results of new BC match well with that of the halfway bounce-back scheme. However, the results of FH's BC differ considerably from the other two because of mass leakage.

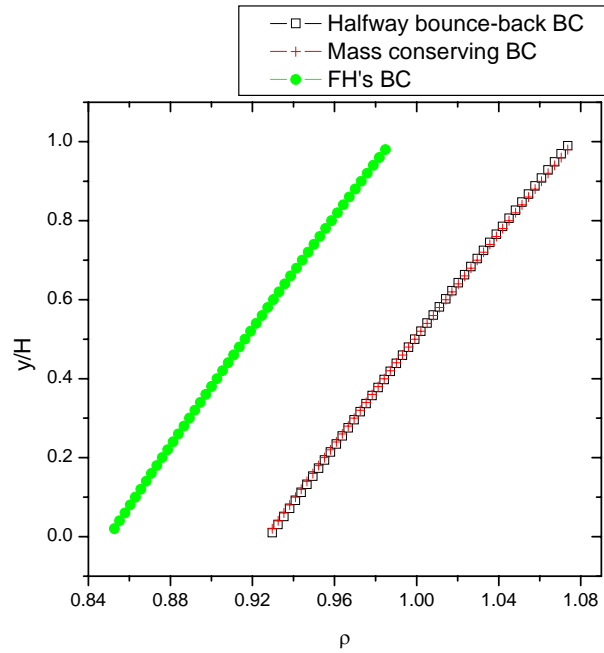


Figure 2.13: The mass distribution at $x = nx/2$ when $t = 60000$ obtained from different schemes.

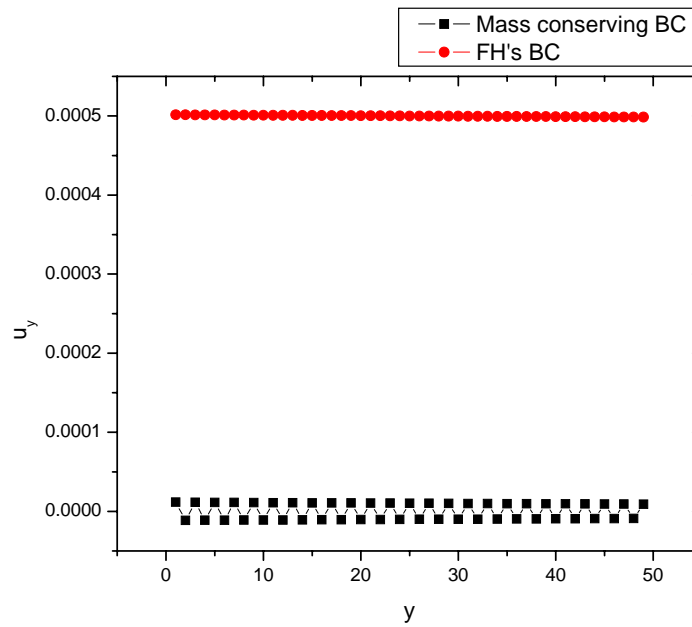


Figure 2.14: y -component of velocity at $x = nx/2$ when $t = 60000$ obtained from different schemes.

Theoretically, all of the x - and y -components of velocity should be zero. However, due to the compressibility of the scheme, one will get non-zero y velocities in the simulation. Comparison of y velocities between our new BC and FH's BC is given in Figure 2.14, where y velocities at $x = nx/2$ when $t = 60000$ are plotted. The y velocities generated by our new scheme are much smaller (about $1/50$) than those of FH's BC.

We have shown that our new BC not only can guarantee mass conservation but also produces more accurate results than FH's BC. Meanwhile, since the $f_\alpha^{(*)}(\mathbf{x}_b, t)$ term now correctly reflects the compressible effect, therefore the weighting coefficients of $\tilde{f}_\alpha(\mathbf{x}_f, t)$ and $f_\alpha^{(*)}(\mathbf{x}_b, t)$ term to find $\tilde{f}_\alpha(\mathbf{x}_b, t)$ become more flexible. In practice, both FH's approach (Eq. (2.9)) and MLS's approach (Eq. (2.10)) can give satisfactory if not entirely accurate results. We will discuss this in detail in the next subsection.

Using the same idea, i.e. setting $\sum_{outgoing} f = \sum_{incoming} f$, the new BC can be easily extended to other types of flat wall boundaries as well as curved wall boundaries. Figure 2.15 shows three types of flat wall boundaries in a 2-D configuration.

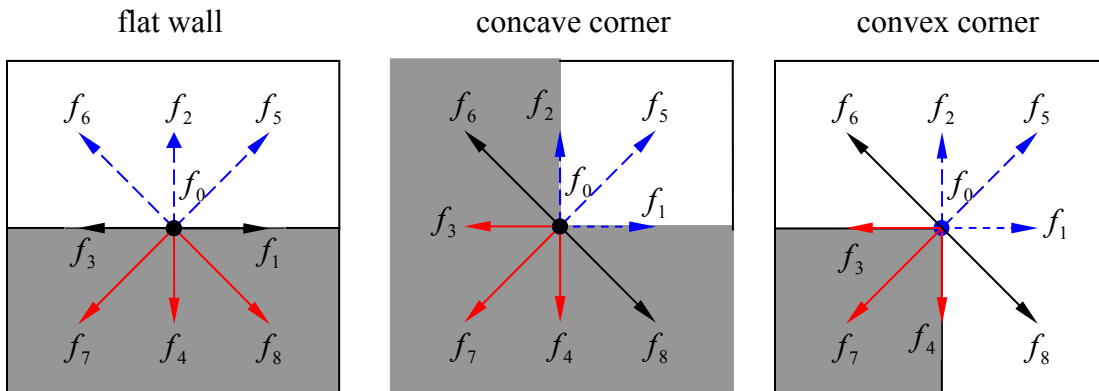


Figure 2.15: Three flat wall boundary configurations. Blue dashed arrows, red plain arrows and black plain arrows represent the incoming distribution, outgoing distribution and fluid-fluid (buried) distribution. Gray areas represent the solid part.

Both for the flat wall and convex corner boundaries, there is one pair of distributions that point into the flow (f_1 and f_3 for a flat wall; f_6 and f_8 for a convex corner), as illustrated by the black plain arrows. These we call fluid-fluid distributions. Since their values are known after streaming and they will not bring net mass change into the flow, we do not need to calculate their value nor need to include them in the procedure of finding the unknown distributions. In the concave corner case, there is one pair of distributions (f_6 and f_8), neither of which point to the flow. We call these buried distributions. Differing from fluid-fluid distributions, the buried distributions are not known after the streaming step. However, since they stream no mass into the flow, in the simulation we can simply switch their values as if they were bounce-back to the opposite direction or give the average value to each of them. Therefore, we do not need to include them in the procedure of finding the unknown distributions.

We use blue and red colors to denote incoming (unknown) and outgoing (known) distributions in the figure. After defining these distributions, it is clear that these three cases are essentially the same. Therefore, for determining the incoming distributions, we can follow the same procedure as described in the flat wall case, i.e. use outgoing distributions to find the $\rho(\mathbf{x}_w, t)$ term, then substitute it into Eq. (2.17) to calculate the incoming distributions.

The new mass conserving boundary treatment can be easily extended to the 3-D case as well as for a curved wall boundary. In doing so, one needs to distinguish the incoming, outgoing, and fluid-fluid (buried) distributions as discussed above. Also for the curved wall boundary, the fraction of the intersected link Δ is not a constant over the entire wall, so one need to decide its value for each boundary node.

2.3.4.3 Benchmark tests for the new boundary condition We have introduced our new mass conserving wall boundary condition in the previous section. The new boundary condition is as simple as FH and MLS's BC yet demonstrates a better performance in the testing example. In this subsection, we will use several benchmark problems to test this new BC further.

A. Fully developed 2-D channel flow

For the fully developed 2-D channel flow driven by the pressure gradient, the analytic solution is:

$$u_{exact}(y) = -\frac{1}{2} \frac{dp}{dx} \frac{H^2}{\rho\nu} (\eta^2 - \eta) \quad (2.20)$$

where $\frac{dp}{dx}$ is the pressure gradient, $H = ny - 2 + 2\Delta$ is the height of the channel and

$\eta = (j - 1 + \Delta) / H$. In order to evaluate the computational error of the scheme, the following

relative L_2 -norm error is defined:

$$E_2 = \frac{\left\{ \int_0^H [u_{LBE}(y) - u_{exact}(y)]^2 dy \right\}^{1/2}}{\left[\int_0^H u_{exact}^2(y) dy \right]^{1/2}} \quad (2.21)$$

where $u_{LBE}(y)$ is the LBE solution of the velocity.

First, we examine the accuracy of the new BC. Figure 2.16 shows the dependence of the relative L_2 -norm error on the lattice resolution for different Δ . Also shown in the figure are the magnitude of the slopes, k , obtained by linear fitting the error data for different Δ . By examining these k values, one can see that second order accuracy was indeed maintained. It has been proved that the LBE method gives second order accuracy for the interior points. Hence the overall second order accuracy obtained here means that the accuracy of boundary condition is at least of the second order.

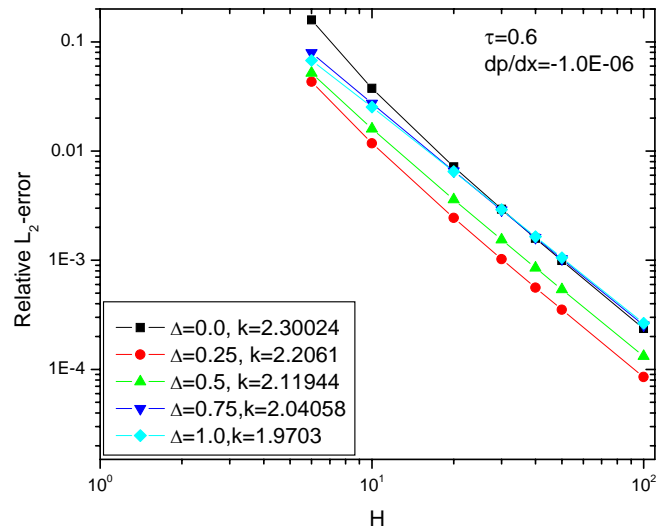


Figure 2.16: Dependence of relative L_2 -norm error on the lattice resolution for 2-D channel flow.

Figure 2.17 shows the relative L_2 -norm error as a function of Δ for 2-D channel flow, which gets its minimum value when $\Delta \approx 0.35$. For other Δ values, the error increases approximately linearly, which is similar to MLS's result.

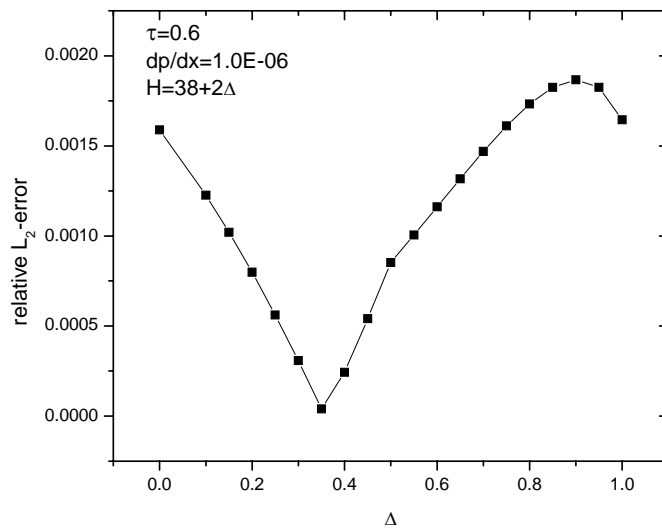


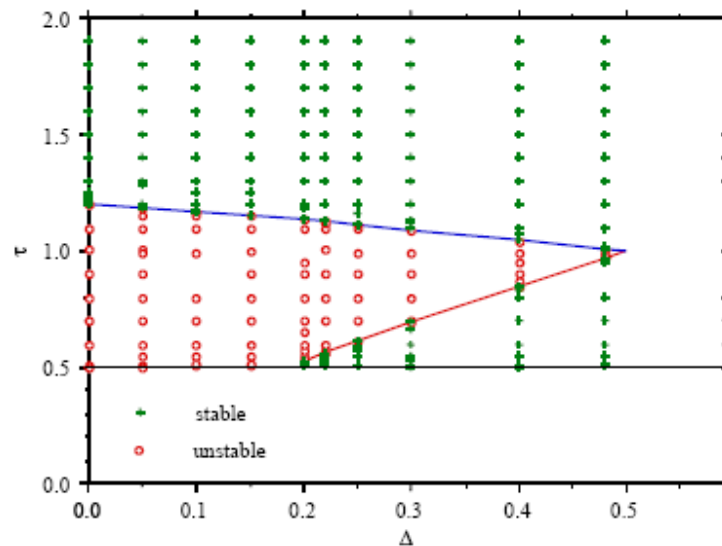
Figure 2.17: Relative L_2 -norm error as a function of Δ for 2-D channel flow.

Table 2.1 gives the L_2 -norm error obtained by different boundary conditions for $\Delta = 0.75$, $\tau = 0.6$. For the new boundary condition, both FH and MLS's approach of determining \mathbf{u}_{bf} were used, denoted by "New + FH" and "New + MLS" in the table. From the table, it is clear that using the same \mathbf{u}_{bf} , the new BC produces the same errors as MLS's BC and smaller errors than FH's BC at higher grid resolutions.

Table 2.1: The L_2 -norm error obtained by different boundary conditions.

BC \ ny	10	20	30	40	50
FH	2.7256083E-02	6.5637481E-03	2.8808801E-03	1.6132460E-03	1.3193971E-03
New + FH	2.7256083E-02	6.5637481E-03	2.8808800E-03	1.6103690E-03	1.0267685E-03
MLS	3.0453999E-02	7.3338629E-03	3.2188895E-03	1.8021873E-03	1.4392486E-03
New + MLS	3.0453999E-02	7.3338629E-03	3.2188895E-03	1.8021873E-03	1.4392486E-03

A main advantage of the new BC over FH and MLS's BC is its excellent stability. Figure 2.18 shows the stable and unstable regions in the LBE computation for fully developed 2-D channel flow using FH's BC and MLS's BC. For $\Delta < 1/2$, there exist a certain region of τ , under which the computation is not stable. For FH and MLS's BC, this region is around $\tau = 1$ and $\tau = 2$, respectively.



(a)

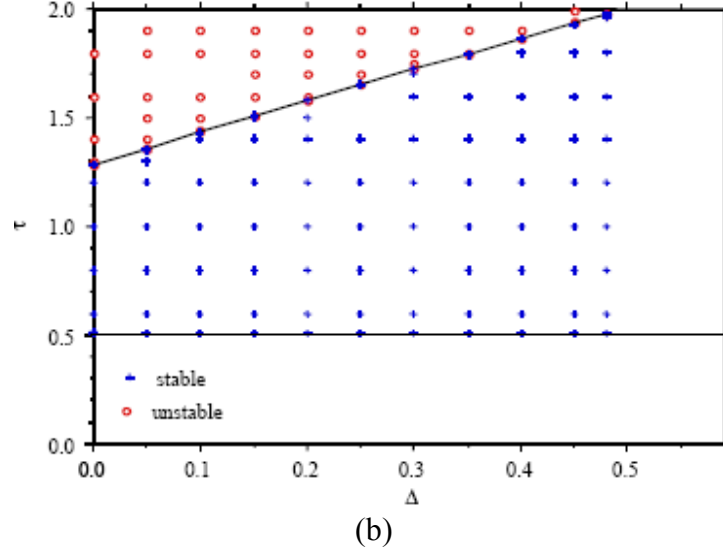


Figure 2.18: Regions of stability and instability in the LBE computation for fully developed 2-D channel flow (after [56]) (a) Using FH's BC, (b) Using MLS's BC .

We think this instability is due to the mass leakage. For FH's BC, when τ is close to 1.0, then the absolute value of weighting factor before the $f_{\alpha}^{(*)}(\mathbf{x}_b, t)$ term becomes very big, since $\chi = (2\Delta - 1)/(\tau - 1)$. We know that the mass leakage in FH's scheme is related to the $f_{\alpha}^{(*)}(\mathbf{x}_b, t)$ term, therefore large $|\chi|$ will result in large mass leakages of the system and finally make the simulation unstable. MLS noticed this problem and changed the definition of the weighting factor to $\chi = (2\Delta - 1)/(\tau - 2)$. This will make the simulation stable for τ values around 1.0; however, for τ values around 2.0, the simulation becomes unstable due to the same reason. To verify this, we performed simulations for a point inside the unstable region ($\Delta = 0.2$, $\tau = 1/0.55 = 1.8181$) using MLS's BC. Figure 2.19 gives the system mass as a function of time, which increases exponentially and finally makes the simulation blow up.

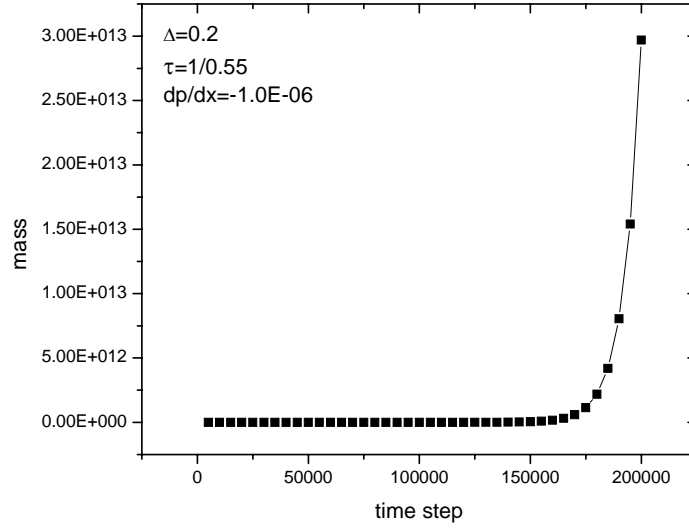


Figure 2.19: System mass as a function of time using MLS's BC.

Furthermore, we think for the MLS's BC there should exist an upper limit for the unstable region similar to that of FH's BC in Figure 2.18 (a), since essentially MLS's BC can be viewed as an revision of FH's BC by linearly shifting the weighting factor. This also has been verified in our simulation. For example, for $\Delta = 0.2$, the MLS treatment is unstable for: $\tau \leq \frac{1}{0.063} = 15.873$.

When $\tau \geq \frac{1}{0.062} = 16.129$, the system becomes stable again. MLS did not give this upper limit in their paper, probably because the large τ value will produce a large slip velocity (as we discussed before) and the simulation results therefore deviate from the analytical solution at this stage.

Figure 2.20 gives regions of stability and instability on the (Δ, τ) plane in the LBE computation for fully developed 2-D channel flow using the new BC. Note that the scale for the y-axis is much finer than in Figure 2.18. Because mass leakage is much smaller in the new BC, the unstable region is much smaller as well. That means in simulation one can use a τ value

which is very close to 2.0. Meanwhile, since mass conservation is guaranteed, different weighting factor will not greatly effect the simulation result. If we need to use $\tau = 2.0$, we can simply switch to FH's weighting factor to avoid the singular point.

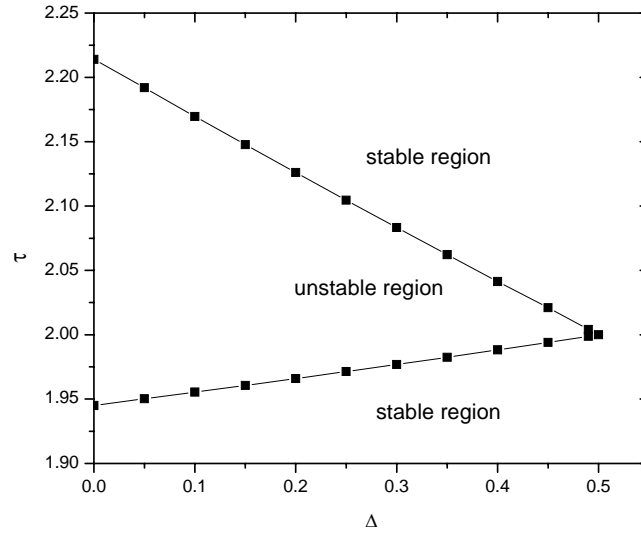


Figure 2.20: Regions of stability and instability in the LBE computation for fully developed 2-D channel flow using new BC.

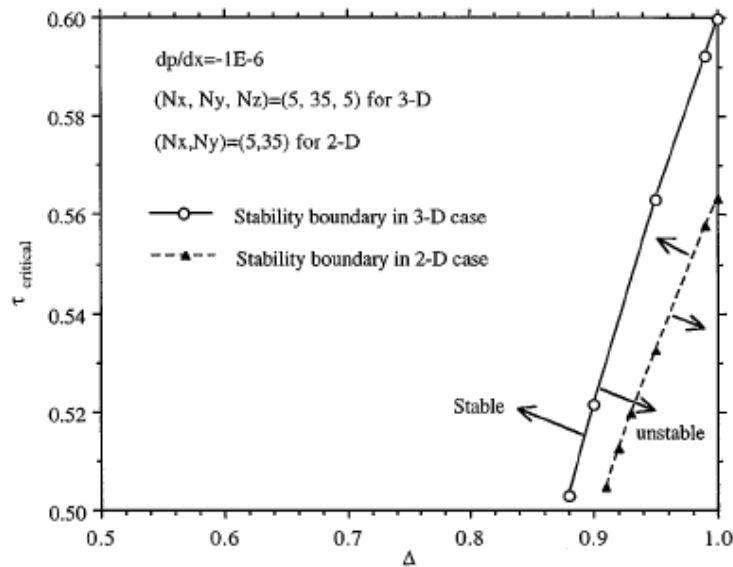


Figure 2.21: Stability boundary of the FH's scheme in a square duct flow for Δ near 1.0 (after [50]).

For $\Delta \geq 0.5$, FH's treatment encounters numerical instability too, as shown in Figure 2.21. By modifying χ and \mathbf{u}_{bf} , MLS's treatment encounters no numerical instability for $\Delta \geq 0.5$. In our new BC, due to mass conservation, there is no numerical instability encountered for $\Delta \geq 0.5$, no matter whether FH's or MLS's χ and \mathbf{u}_{bf} are being used.

We also compared τ_{\min} , the minimum value of τ at which the computation is stable for a given Δ , for the different schemes. It is reported in Guo *et.al.*'s paper [57] that for $\Delta = 0.1$, $\tau_{\min} = 0.509$ for the MLS treatment and 0.506 for his treatment. For $\Delta = 0.2$, $\tau_{\min} = 0.505$ for the MLS treatment and 0.50003 for his treatment. For $\Delta \geq 0.3$, the simulations are still stable for both treatments even as $\tau - 0.5 = 10^{-7}$. For our boundary treatment, under the same conditions, we found that even for $\Delta = 0.1$, the computations are still stable for $\tau - 0.5 = 2.5 * 10^{-11}$. Therefore, our BC has much better numerical stability than the other two methods. Furthermore, this very small achievable τ_{\min} is very useful in simulating flows with high Reynolds numbers.

B. 2-D channel flow with oscillating pressure gradient

The system set up is the same as before, but the pressure gradient is no longer constant, and oscillates with time: $\frac{dp}{dx} = p^* e^{-i\omega t}$, where p^* is the amplitude and ω is the frequency. The exact solution is given by [58]:

$$u_{exact}(y, t) = \text{Re} \left\{ \frac{p^*}{i\omega\rho} \left[1 - \frac{\cosh \left[\frac{1}{\sqrt{2}} (\alpha + i\alpha) \frac{y}{a} \right]}{\cosh \left[\frac{1}{\sqrt{2}} (\alpha + i\alpha) \right]} \right] e^{i\omega t} \right\} \quad (2.22)$$

where a is half of the channel width $a = H/2$ and α is the Womersley number defined by:

$\alpha = a \sqrt{\frac{\omega}{\nu}}$. "Re" denotes the real part of the solution. For a small Womersley number, Eq. (2.22)

reduced to $u_{exact}(y,t) \cong -\frac{1}{2} \frac{H^2}{\rho\nu} (\eta^2 - \eta) p^* \cos(\omega t)$, which is simply a quasi-steady flow and the velocity profile at any time is the same as that of Poiseuille flow with the corresponding forcing term. At large α , the velocity profile is no longer parabolic.

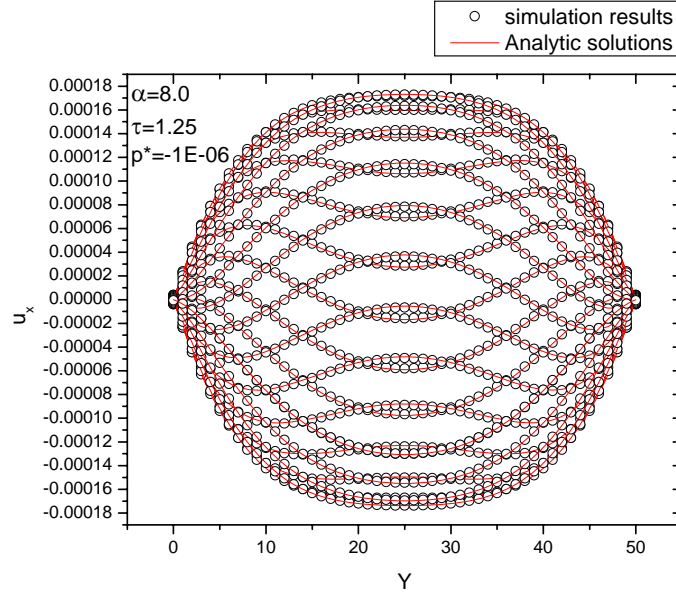


Figure 2.22: Obtained velocity profiles (black dots) over a complete period compared to the exact solution (red lines). The measurements are taken at the middle of the channel, at each $t = 0.04nT$ when $n = 0,1,\dots,25$.

Figure 2.22 shows obtained velocity profiles (dots) over a complete period, $T = 2\pi / \omega$, compared to the exact solution (lines) with $\tau = 1.25$, $\alpha = 1$ and $p^* = -1.0E - 06$. The measurements are taken at the middle of the channel, at each $t = 0.04nT$ when $n = 0,1,\dots,25$. Good agreement was achieved. Since the error will vary with time, a time averaged error over one period is used and defined by:

$$E_2 = \frac{\left\{ \int_0^T \int_0^H [u_{LBE}(y,t) - u_{exact}(y,t)]^2 dy dt \right\}^{1/2}}{\left[\int_0^T \int_0^H u_{exact}^2(y,t) dy dt \right]^{1/2}} \quad (2.23)$$

Figure 2.23 shows the dependence of the relative L_2 -norm error on the lattice resolution for oscillating 2-D channel flow. The slope of the line obtained by linear fitting is -2.17508, which indicates second order accuracy was maintained. Table 2.2 gives the L_2 -norm error obtained by the MLS and new boundary conditions for $\tau = 0.6$, $\alpha = 0.5$, and $p^* = -1.0E-06$. The new BC generally gives a slightly smaller error than the MLS's BC, since τ is not very small nor close to a singular point. Again, in terms of stability, our new BC performs much better, as discussed before.

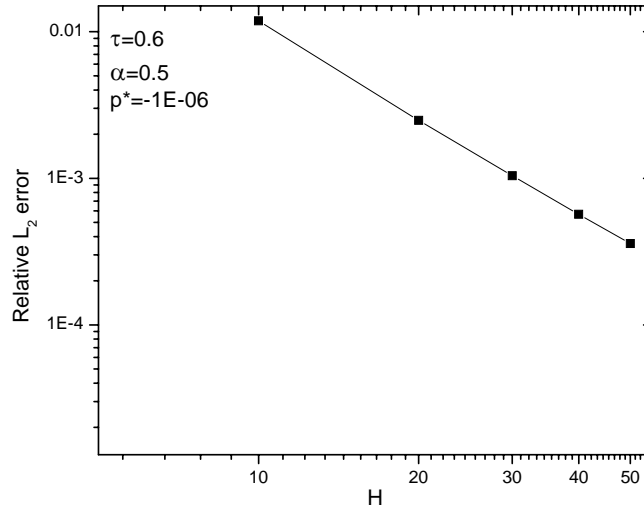


Figure 2.23: Dependence of relative L_2 -norm error on the lattice resolution for oscillating 2-D channel flow.

Table 2.2: L_2 -norm error obtained by different boundary conditions

ny \ L_2 error	New BC	MLS's BC
10	1.1870700E-02	1.1870700E-02
20	2.4790973E-03	2.4791020E-03
30	1.0415668E-03	1.0415659E-03
40	5.6822888E-04	5.6999016E-04
50	3.5878056E-04	3.5878056E-04

C. Stokes first problem: flow due to an impulsively started wall

For Stokes first problem, the wall is placed at $y = 0$ and is impulsively started. The exact solution is given by:

$$u_{exact}(y, t) = u_{wall} \left[1 - \operatorname{erf}\left(\frac{y}{2\sqrt{vt}}\right) \right] \quad (2.24)$$

where u_{wall} is the velocity of the wall and will be substituted into BC as \mathbf{u}_w term. As time increases, an unsteady Stokes layer with thickness $O(\sqrt{vt})$ develops near the wall. The LBE method is a fix-grid computation, with $\delta x = \delta y = \delta t = 1$, so therefore the error at small times is expected to be large due to insufficient spatial resolution. Figure 2.24 shows the velocity profiles at $t = 100$ (in lattice units) with different values of Δ . The error is smaller for $\Delta = 0.25$ than for 0.5 and 0.75 due to a better spatial resolution near the wall.

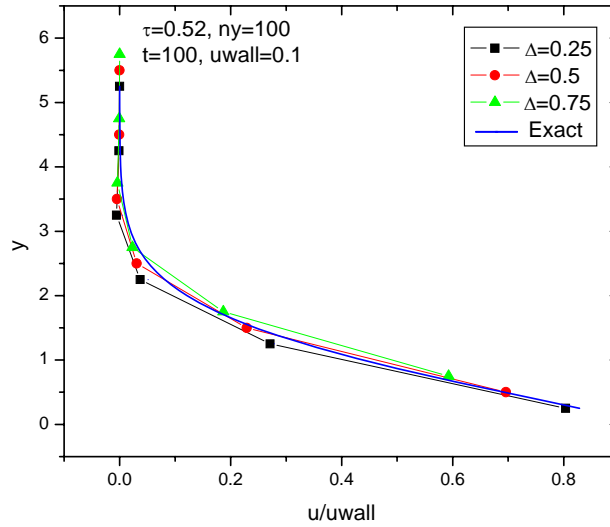


Figure 2.24: Velocity profiles at $t = 100$ (in lattice units) for Stokes first problem with different values of Δ .

We define the L_2 -norm error as:

$$E_2 = \frac{\left\{ \int_0^\infty [u_{LBE}(y,t) - u_{exact}(y,t)]^2 dy \right\}^{1/2}}{\left[\int_0^\infty u_{exact}^2(y,t) dy \right]^{1/2}} \quad (2.25)$$

Figure 2.25 gives the relative L_2 -norm error as function of time for different values of Δ . Also shown in the figure is the error obtained by using halfway bounce-back scheme (denote as BBL in the figure). We can clearly see that $\Delta = 0.25$ gives a smaller error than $\Delta = 0.5$ and 0.75 , especially at small time. The error decreases with time, which is because the spatial resolution becomes adequate after the Stokes layer grows to a certain thickness. The error of $\Delta = 0.5$ is very close to the error obtained by using halfway bounce-back scheme, which indicates the second order accuracy of the scheme.

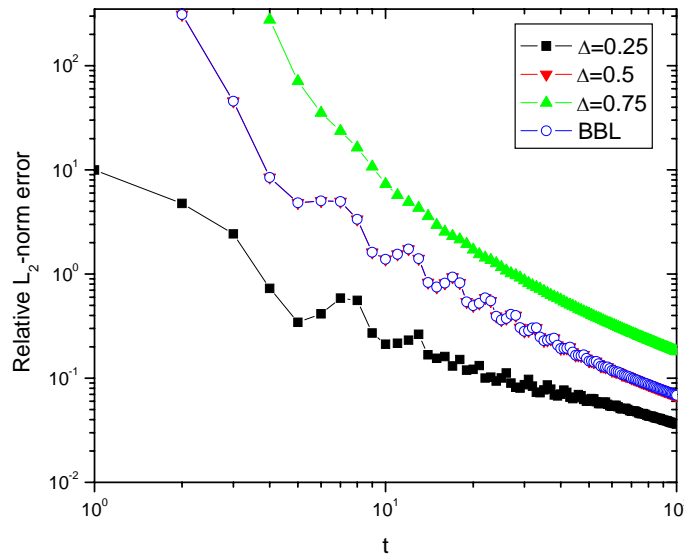


Figure 2.25: Relative L_2 -norm error as function of time for the Stokes first problem with different values of Δ .

D. 2-D lid-driven cavity flow

For 2-D lid-driven cavity flow, the right and left corner at the upper wall are singular points and will be treated as concave corners, as discussed in a previous subsection. We first compare the simulation results of $\Delta = 0.5$ with the halfway bounce-back scheme, which is known to give a result with second-order accuracy.

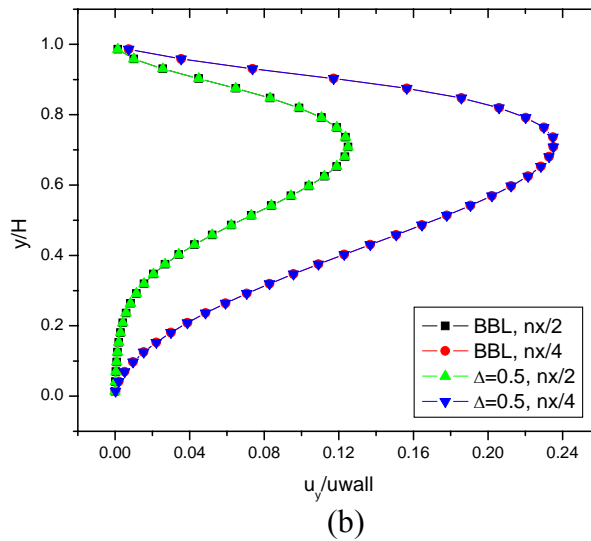
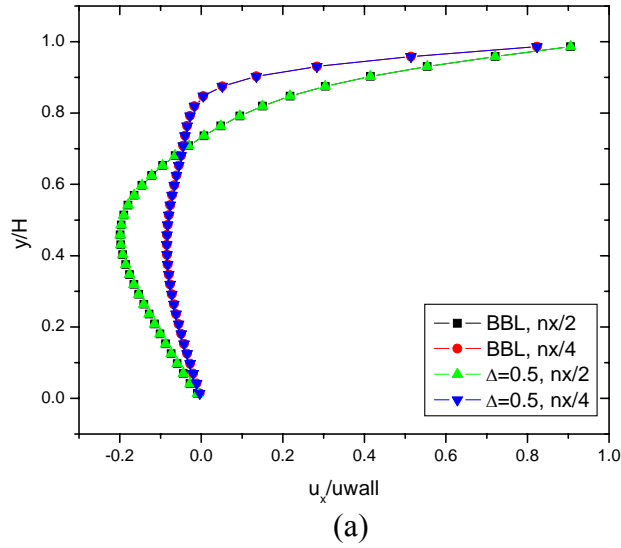


Figure 2.26: Velocity profiles at $nx/4$ and $nx/2$ in lid-driven cavity flow for $\Delta = 0.5$ and halfway bounce-back (denote as BBL: bounce-back at link in the figures) scheme. (a) x component of velocity, (b) y component of velocity.

Figure 2.26 shows the velocity profiles at $nx/4$ and $nx/2$ for $\Delta = 0.5$ and a halfway bounce-back scheme with $Re = 100$. Excellent agreement was obtained. Furthermore, the halfway bounce-back scheme becomes unstable when $\tau \leq 0.53$, while our new BC encounters no instability even at $\tau \leq 0.5001$. Figure 2.27 shows velocity profiles at $nx/4$ and $nx/2$ for different values of Δ .

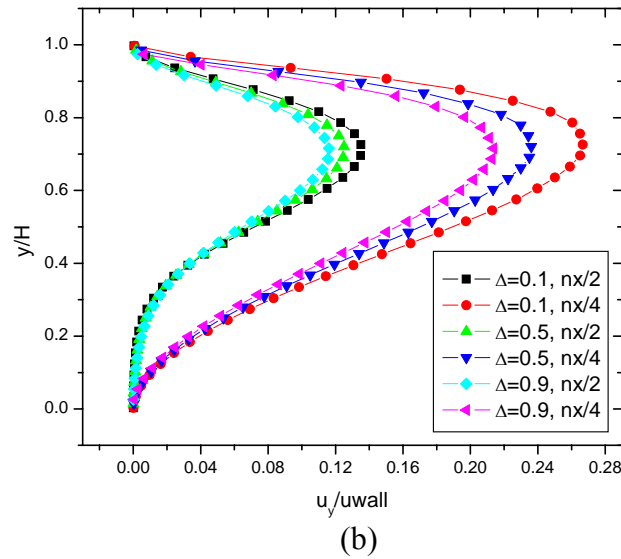
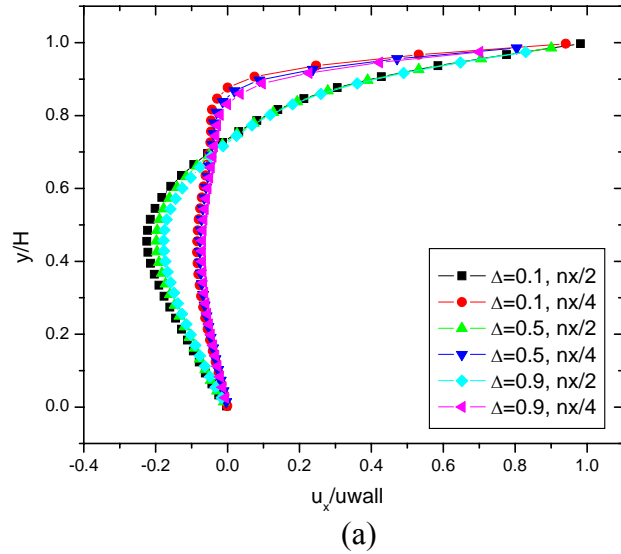


Figure 2.27: Velocity profiles at $nx/4$ and $nx/2$ for different values of Δ . (a) x component of velocity, (b) y component of velocity.

2.3.4.4 Conclusion In summary, we propose a second-order accurate mass conserving boundary condition for the LBE method. Several benchmark test problems involving steady and unsteady flows were used to validate the accuracy and examine the robustness of the proposed BC. Compared with the FH and MLS's BCs, our new BC has the following advantages: (1) The mass leakage is smaller than in other schemes and will not result in a constant mass leakage (as for other BCs) in some special cases. (2) It has much better stability than any other BC used in the simulations. Both the unstable region and the achievable minimum τ value are much smaller than those of other schemes. (3) In the normal region of Δ and τ , i.e. the stable region for all BCs, it gives second order accuracy and comparable or better results than other schemes. (4) It is not sensitive to the interpolation (weighting) factor and choice of \mathbf{u}_{bf} .

2.4 DISCUSSION

In this chapter, we demonstrated the different open boundary treatments and wall boundary treatments. For the wall BCs, FH and MLS BC are widely used in the LB simulations, due to their robustness, capability of handling curved wall boundary, and easy implementation. However, we found that these BCs will result to constant mass leakage in certain circumstance. We analyzed the source of the leakage. Based on this analysis, we proposed a second-order accurate mass conserving wall boundary condition for the LBE method. We have showed through several benchmark test problems involving steady and unsteady flows that our new BC not only solved the problem of constant mass leakage but also have many other advantages, like much wider stable region, over the FH and MLS BC. Furthermore, we think the idea of mass

conserving treatment can be extended to the open boundaries to develop corresponding boundary treatment, where further research is needed.

3.0 MULTIPHASE LBE MODEL

3.1 INTRODUCTION

The importance of understanding fluid flow and heat transfer with a change in phase arises from the fact that many industrial processes rely on these phenomena for materials processing or for energy transfer, e.g. petroleum processing, paper-pulping, power plants. There are many common examples of multiphase flow and heat transfer not only in industrial processes but also everyday life. Thus the understanding of multiphase flow is essential for both fundamental research and engineering applications. However, due to the complex nature of multiphase flow, theoretical solutions are generally limited to relatively simple cases. Meanwhile, the experimental approaches for multiphase flow are very expensive if not impossible, depending on the scale and/or fluid composition. Therefore, it is reasonable to say that numerical simulations are primarily useful in studying the underlying physics of multiphase flow and providing information about the details of processes that are difficult to obtain by theoretical analysis or by experiments.

3.2 COMPUTATIONAL APPROACHES USED IN TWO-PHASE FLOW SIMULATION

In simulating multiphase flow, there are several traditional CFD methods, most of which can be fitted in two categories: the front-capturing method and front-tracking method. We will briefly review these methods in this section and also introduce LB two-phase flow models.

3.2.1 Front capturing methods

Front-capturing methods track the movement of fluid and ‘capture’ the interface afterwards. In these methods, the two fluids are modeled as a single continuum with discontinuous properties at the interface. The fluid flow equations for both fluids are solved in the same Eulerian mesh. There are three types of front capturing methods: the Marker-and-Cell (MAC) method [59, 60], Volume-of-Fluid (VOF) method [61], and level set method [62], based on how the interface propagation is obtained thereafter.

In the Marker-and-Cell (MAC) method, the Lagrangian markers are used to represent the location of the liquid (one phase). The interface is then constructed based on the location of the markers. Physical properties, i.e. viscosity and density, for the fluid at each grid point are determined by the phase present. Figure 3.1 illustrates this concept. The MAC method is computationally very expensive, since in order to accurately determine the interface one needs to track a very large number of markers.

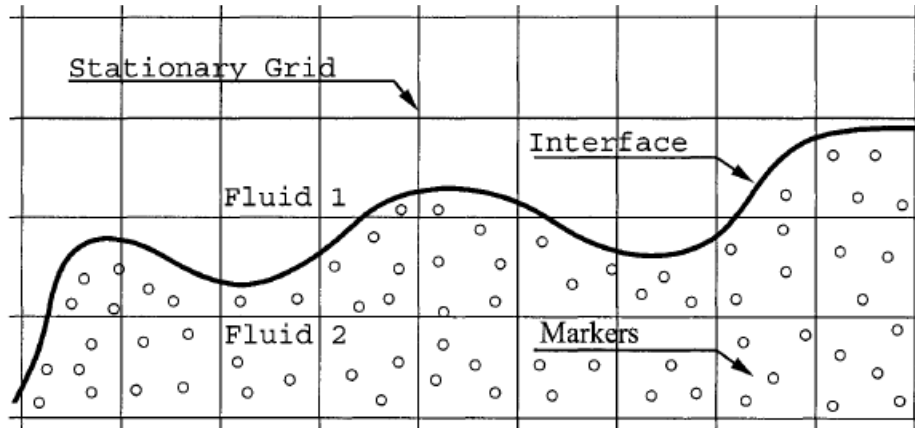


Figure 3.1: Schematic for the Marker-and-Cell method (after [63]).

The Volume-of-Fluid (VOF) method was introduced to reduce the heavy computational load of the MAC method. In the VOF method, instead of tracking a large number of markers, the volume fraction of fluid in each cell is used to track the movement of the liquid. Therefore, the computational cost is greatly reduced. However, the VOF method still has difficulties in determining the exact location of the interface.

The level set method uses two sets of equations to model the two-phase flow system. The first set, like the other two methods, is comprised of the single fluid N-S equations, which are employed to determine the momentum. The second set is a transient scalar advection equation which tracks a level set function. The level set function equals zero at the interface, a negative value for locations inside one phase, and a positive value for locations inside another phase. The location of the interface is determined by interpolating between the level set function values. In the level set method, the interface is much easier to determine compared to the MAC and VOF methods. However, it has some problems with mass conservation, because the advection of the level set function is not based on a strictly conservative equation.

Furthermore, the solution of front-capturing method is prone to numerical diffusion and dispersion problems, which are inherent in the numerical solution of hyperbolic equations by any discretization scheme when there are discontinuities in the solution.

3.2.2 Front-tracking methods

Front-tracking methods directly ‘track’ the location of the two-phase interface. Therefore they allow more accurate calculation of the curvature of the interface [64]. Most commonly used front-tracking methods are: the boundary-fitted grid method [65], Tryggvassions’s hybrid method [66], and Boundary Element Method (BEM) [67].

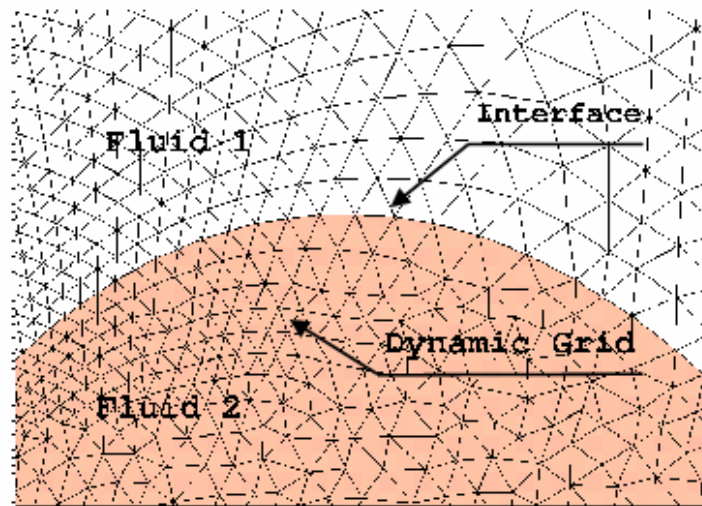


Figure 3.2: Schematic for boundary-fitted method (after [63]).

In the boundary-fitted grid method, two sets of N-S equations are solved—one for each fluid. The grid of the computational domain is constructed in such a fashion that the interface between two phases is located along a grid line, as shown in Figure 3.2, and the movement of the interface is determined by a force balance. In the hybrid method proposed by Tryggvason, two sets of grids are used, i.e.: a stationary grid used to determine the fluid flow and a lower

dimension grid used to track the interface. In the Boundary Element Method (BEM), a multitude of boundary nodes are employed to represent the two-phase interface. The movement of these boundary nodes is based on the potential function equations.

3.2.3 Lattice Boltzmann two-phase models

Although conceptually simple, it is more difficult to implement these traditional CFD methods in a two-phase flow simulation. The difficulties arise from the interface deformation and interaction. Computationally, one might be able to track a few, but hardly very many, interfaces in a system.

Recently, simulating multiphase flow with the LBE method has attracted much attention. Microscopically, the phase segregation and surface tension in multiphase flow are because of the interparticle forces/interactions. Due to its kinetic nature, the LBE method is capable of incorporating these interparticle interactions, which are difficult to implement in traditional methods. Therefore, the key step in developing the LBE multiphase model is to correctly incorporate the particle interactions into the evolution of PDFs so that macroscopically correct multiphase flow behavior can be obtained.

There have been a number of LB multiphase flow models presented in the literature. The first immiscible multiphase LB model proposed by Gunstensen *et al.* uses red- and blue- colored particles to represent two kinds of fluids [68]. The phase separation is then produced by the repulsive interaction based on the color gradient and color momentum. The model proposed by Shan and Chen (SC) imposes a non-local interaction between fluid particles at neighboring lattice sites [69-72]. The interaction potentials control the form of the equation of state (EOS) of the fluid. Phase separation occurs automatically when the interaction potentials are properly chosen. There is also the so-called free-energy-based approach proposed by Swift *et al.* [73, 74].

In this model, the description of non-equilibrium dynamics, such as Cahn-Hilliard's approach, is incorporated into the LB model by using the concepts of the free energy function. The free energy model has a sound physical basis, and, unlike the SC model, the local momentum conservation is satisfied. However, this model does not satisfy Galilean invariance and some unphysical effects will be produced [75] in the simulation. In the multiphase model proposed by He, Chen and Zhang (HCZ) [76, 77], two sets of PDFs are employed. The first PDF set is used to simulate pressure and velocity fields and another PDF set is used to capture the interface only, which makes this approach essentially close to the interface capturing methods in spirit. Their approach is more flexible in implementing the thermodynamics of the flow. A severe problem with their approach is its numerical instability.

3.3 SINGLE COMPONENT MULTIPHASE LATTICE BOLTZMANN MODEL

Among all of the LBE two-phase flow models, the SC model is widely used due to its simplicity and remarkable versatility: it can handle fluid phases with different densities, viscosities and wettabilities, and handle different equations of state as well. Originally, the SC model was proposed for the flow system with multiple phases and components. Later on, the model was also used in single component multiphase flow systems. In this study, we will employ the single component multiphase (two-phase) version of SC model.

Microscopically, the segregation of a fluid system into different phases is due to the interparticle forces [78]. In the single component multiphase LBE model proposed by Shan and Chen, a simple long-range interaction force between the particles at site \mathbf{x} and the particles at site \mathbf{x}' is introduced:

$$\mathbf{F}_f(\mathbf{x}) = -\psi(\mathbf{x}) \sum_{\mathbf{x}'} G(\mathbf{x}, \mathbf{x}') \psi(\mathbf{x}') (\mathbf{x}' - \mathbf{x}) \quad (3.1)$$

where $G(\mathbf{x}, \mathbf{x}')$ is Green's function and satisfies $G(\mathbf{x}, \mathbf{x}') = G(\mathbf{x}', \mathbf{x})$. It reflects the intensity of the interparticle interaction, with $G(\mathbf{x}, \mathbf{x}') < 0$ representing attractive forces between particles. $\psi(\mathbf{x})$ is called the “effective mass” and is defined as a function of \mathbf{x} through its dependency on the local density, $\psi(\mathbf{x}) = \psi(\rho(\mathbf{x}))$. In the SC model, the function of $\psi(\mathbf{x})$ can be varied, and different choices will give a different EOS.

In order to perform the numerical simulation, SC introduced the concept of the nearest neighbor interparticle force, which means that only the interactions between the nearest neighbors are considered:

$$G(\mathbf{x}, \mathbf{x}') = \begin{cases} g, & |\mathbf{x} - \mathbf{x}'| \leq c \\ 0, & |\mathbf{x} - \mathbf{x}'| > c \end{cases} \quad (3.2)$$

where c is the lattice spacing, and g represents the strength of interparticle interactions. It needs to be pointed out that, with the inclusion of the interparticle force, the collision operator does not conserve the momentum locally (i.e. at each site). However, the momentum of the whole fluid system is indeed conserved, since $G(\mathbf{x}, \mathbf{x}')$ is defined in Eq. (3.2) as a symmetric matrix. This non-conserved local momentum in the collision step distinguishes the SC model from other multiphase LBE models, e.g. the free energy model. With Eq. (3.2),

$$\mathbf{F}_f(\mathbf{x}) = -\psi(\mathbf{x}) \sum_{\alpha=0}^b g \psi(\mathbf{x} + \mathbf{e}_\alpha) \mathbf{e}_\alpha \quad (3.3)$$

In SC's original model, each lattice site has b nearest neighboring sites with equal distance c and resides on a D dimensional space. \mathbf{F}_f can be approximated by:

$$\mathbf{F}_f(\mathbf{x}) \cong -\frac{c^2 b}{D} \psi(\mathbf{x}) g \nabla \psi(\mathbf{x}) \quad (3.4)$$

It should be noted here that although Eq. (3.4) is derived by only using the interparticle forces of nearest neighbor sites in SC's original paper, it can be extended to include other neighboring sites as long as the gradient term $\nabla\psi(\mathbf{x})$ is properly specified. Therefore, for different lattice structures, Eq. (3.4) becomes:

$$\mathbf{F}_f(\mathbf{x}) \cong -c_0\psi(\mathbf{x})g\nabla\psi(\mathbf{x}) \quad (3.5)$$

where c_0 is the constant depending on the lattice structure. For the D2Q9 and D3Q19 lattices, $c_0 = 6.0$, and for the D3Q15 lattice, $c_0 = 10.0$.

An example will be presented for the way to numerically evaluate the gradient term $\nabla\psi(\mathbf{x})$ in a D2Q9 lattice. Suppose we use both nearest and next-nearest sites to evaluate this gradient term, which gives a six-point scheme for 2-D:

$$\begin{aligned} \frac{\partial\psi(i,j)}{\partial x} &= c_1[\psi(i+1,j) - \psi(i-1,j)] + c_2[\psi(i+1,j+1) - \psi(i-1,j+1) + \psi(i+1,j-1) - \psi(i-1,j-1)] \\ \frac{\partial\psi(i,j)}{\partial y} &= c_1[\psi(i,j+1) - \psi(i,j-1)] + c_2[\psi(i+1,j+1) - \psi(i+1,j-1) + \psi(i-1,j+1) - \psi(i-1,j-1)] \end{aligned} \quad (3.6)$$

where c_1 and c_2 are weighting coefficients for nearest and next nearest sites, respectively. For

the second order central difference scheme: $\frac{\partial\psi(i,j)}{\partial x} = \frac{\psi(i+1,j) - \psi(i-1,j)}{2\Delta x}$, since in the LBE

method, $\Delta x = \Delta y = 1$. By averaging terms of next nearest sites to nearest sites, we find that a

correct representation of the gradient term will require $c_1 + 2c_2 = \frac{1}{2}$. Meanwhile, for the purpose

of maintaining the isotropy of the scheme, the sites used in the calculation of the gradient term

should be symmetric about the axes $x = i$ and $y = j$. Finally, we require that $c_1 > c_2$, since

physically the closer sites will have more influence on the interaction.

Now we examine several schemes used in the literature. If we set $c_1 = 4c_2$, we find that this is essentially the “nearest and next-nearest scheme” used in Kang’s paper [79], where Eq. (3.1) is used and $G(\mathbf{x}, \mathbf{x}')$ is given by:

$$G(\mathbf{x}, \mathbf{x}') = \begin{cases} g', & |\mathbf{x} - \mathbf{x}'| = 1. \\ g'/4, & |\mathbf{x} - \mathbf{x}'| = \sqrt{2}. \\ 0, & \textit{otherwise}. \end{cases} \quad (3.7)$$

The only difference is that g' needs to be rescaled. Comparing Eqs. (3.1), (3.5) and (3.6), we find that:

$$g_f = c_0 c_1 g = 6 * \frac{1}{3} g = 2g \quad (3.8)$$

If we set $c_1 = 2c_2$, we can recover another scheme used by Sukop [80]. Again, one only needs to rescale g' accordingly. Using Eq. (3.1), different forms of $G(\mathbf{x}, \mathbf{x}')$ were proposed in the literature [81], which result in different critical values of g . However, by comparing them with Eq. (3.5), we can link all of these critical values together.

In calculating the gradient term, one can include more sites, but by doing so more weighting coefficients need to be added in Eq. (3.6). Determining these additional weighting coefficients is not straightforward. The “correct” scheme not only needs to satisfy the abovementioned criteria but also should generate the same density profiles for the flat interface case. The spurious currents (the unphysical velocities generated in the simulation), isotropy and stability of the scheme can differ considerably for different schemes, especially for the circular interface. We found that the 20-point scheme used in Qian’s paper [82] gives the smallest spurious currents and better isotropy for the circular interface. However, this scheme is computationally more expensive than the six-point scheme (for the 3-D case, it needs 44 neighboring sites) and is

further complicated when dealing with the wall boundary. Therefore, in this work we use the six-point scheme with $c_1 = 4c_2 = \frac{1}{3}$ for the D2Q9 model, which can provide more isotropy simulation results for a circular interface than any of the other six-point schemes. For 3-D simulations, we notice that the D2Q9 model can be viewed as a 2-D projection of the D3Q19 model, if we proceed with the same projection for the gradient term, we will find the corresponding scheme in the D3Q19 model requires $c_1 = 2c_2 = \frac{1}{6}$. The spurious currents produced by these two schemes are at the same level and are only slightly higher than that of the 20-point scheme. In most simulations, we will use these two schemes which include nearest and next-nearest neighbors and denote their strength of interparticle interactions as g_f hereafter.

If the interaction force is given by Eq. (3.5), using the Chapman-Enskog expansion, one can show that the EOS is given by:

$$p = c_s^2 \rho + \frac{c_0}{2} g[\psi(\rho)]^2 \quad (3.9)$$

where c_s is the speed of sound for the LB scheme. For the D2Q9 and D3Q19 models, $c_s = \frac{1}{\sqrt{3}}$. The above equation represents a non-ideal gas law, with non-ideality at the second term depending explicitly on the fluid-fluid interaction. In this study, following the SC approach, the $\psi(\mathbf{x})$ is first taken to be: $\psi(\mathbf{x}) = \rho_0 [1 - \exp(-\rho/\rho_0)]$, which gives a non-monotonic pressure-density relationship. Hence for a certain range of g_f values, at a single pressure, two densities of the same material can coexist. We will discuss other choices of $\psi(\mathbf{x})$ in next chapter.

At the fluid-solid interface, similarly, an interaction force between fluid particles and solid surfaces can be introduced into the SC model as follows [25, 83]:

$$\mathbf{F}_w(\mathbf{x}) = -\rho(\mathbf{x}) \sum_{\mathbf{x}'} G_w(\mathbf{x}, \mathbf{x}') \rho_w(\mathbf{x}') (\mathbf{x}' - \mathbf{x}) \quad (3.10)$$

where $G_w(\mathbf{x}, \mathbf{x}')$ reflects the intensity of the fluid-solid interaction and has the same form as $G(\mathbf{x}, \mathbf{x}')$. For the D3Q19 lattice model,

$$G_w(\mathbf{x}, \mathbf{x}') = \begin{cases} g_w, & |\mathbf{x} - \mathbf{x}'| = 1; \\ g_w / 2, & |\mathbf{x} - \mathbf{x}'| = \sqrt{2}; \\ 0, & \text{otherwise.} \end{cases} \quad (3.11a)$$

and for the D2Q9 model:

$$G_w(\mathbf{x}, \mathbf{x}') = \begin{cases} g_w, & |\mathbf{x} - \mathbf{x}'| = 1; \\ g_w / 4, & |\mathbf{x} - \mathbf{x}'| = \sqrt{2}; \\ 0, & \text{otherwise.} \end{cases} \quad (3.11b)$$

g_w controls the strength between fluid and the wall. g_w is positive for a nonwetting fluid, and negative for a wetting fluid. Adjusting the value of g_w can give a different wettability. $\rho_w(\mathbf{x}')$ is the wall density, which equals one at the wall and zero in the fluid. Since the fluid-solid interaction force $\mathbf{F}_w(\mathbf{x})$ only exists on the fluid-solid interface, therefore it does not change the macroscopic fluid equations [79], e.g. the EOS is still given by Eq. (3.9).

Finally, constant body forces such as gravity can be expressed as:

$$\mathbf{F}_b = \rho(\mathbf{x}) \mathbf{a} \quad (3.12)$$

where \mathbf{a} is the acceleration due to the body force.

All of these forces can be incorporated into the model by shifting the velocity in the equilibrium distribution. That means we replace velocity \mathbf{u} in Eq. (1.6) with [84]:

$$\mathbf{u}^{eq} = \mathbf{u} + \frac{\tau \mathbf{F}_{total}}{\rho(\mathbf{x})} \quad (3.13)$$

where $\mathbf{F}_{total} = \mathbf{F}_f + \mathbf{F}_w + \mathbf{F}_b$. Then, by averaging the moment before and after the collision, the whole fluid velocity \mathbf{U} is:

$$\rho(\mathbf{x})\mathbf{U} = \rho(\mathbf{x})\mathbf{u} + \frac{1}{2}\mathbf{F}_{total} \quad (3.14)$$

There are also other approaches for incorporating fluid-fluid interactions such as the direct body forcing approach, where the interaction is incorporated into the body force term of the Boltzmann equation by adding an additional term after the collision process [55, 85].

3.4 BENCHMARK TESTS

3.4.1 Single-phase flow tests for LBE model

Before performing the simulations for a two-phase LBE model, two simple tests were conducted to verify the accuracy and validity of the LBE method. First, numerical simulations were carried out for a 2-D lid-driven cavity flow for $Re = 400$ and 1000 on a 167×167 lattice. The driving lid is placed at the top with a uniform velocity of $\mathbf{u}_w = 0.1$ in lattice units (denoted as Lu). The no-slip boundary condition proposed in Chapter 2 was used at both the stationary wall and the moving wall.

Figure 3.3 shows the streamlines for $Re = 1000$. The flow structure is in good agreement with previous work. Figure 3.4 shows the x component of velocity at the vertical centerline ($x/H = 1/2$) of the cavity. To quantify the results, the maximum and minimum values of the stream functions and x and y coordinates of the primary and secondary vortex centers are listed in Table 3.1. The results predicted by the LBM agree well with other previous work [86].

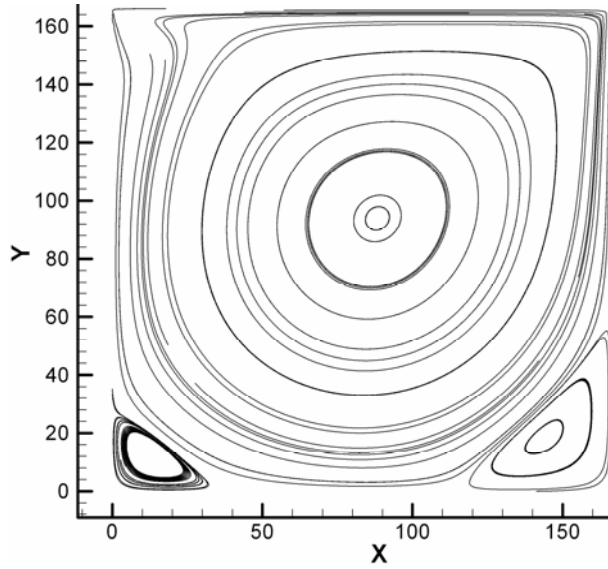


Figure 3.3: Streamlines of 2-D lid-driven cavity flow at $Re = 10^3$

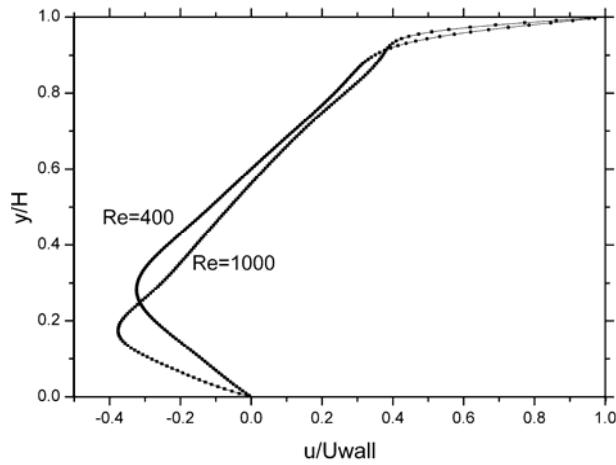


Figure 3.4: Velocity profiles for u along the vertical geometric centerline of the cavity

Table 3.1: Vortex centers: Stream function and location

Re	mesh=167*167	primary vortex			lower left vortex			lower right vortex		
		φ_{max}	x	y	φ_{min}	x	y	φ_{min}	x	y
400	U.Ghia	0.1139	0.5547	0.6055	-1.42E-05	0.0508	0.0469	-6.42E-04	0.8906	0.1250
	S. Hou	0.1121	0.5608	0.6078	-1.30E-05	0.0549	0.0510	-6.19E-04	0.8902	0.1255
	present work	0.1120	0.5551	0.6054	-1.28E-05	0.0505	0.0463	-6.15E-04	0.8858	0.1222
1000	U.Ghia	0.1179	0.5313	0.5625	-2.31E-04	0.0859	0.0781	-1.75E-03	0.8594	0.1094
	S. Hou	0.1178	0.5333	0.5647	-2.22E-04	0.0902	0.0784	-1.69E-03	0.8667	0.1137
	present work	0.1161	0.5319	0.5652	-2.13E-04	0.0821	0.0769	-1.66E-03	0.8652	0.1125

The other simple test was fully developed 2-D channel flow, driven by the pressure gradient. The analytic solution for this problem is given by Eq. (2.25) in Chapter 2. In our LBE simulation, we set $\frac{dp}{dx} = -1.0 \times 10^{-6}$, $\tau = 1.0$ and $\Delta = 1.0$.

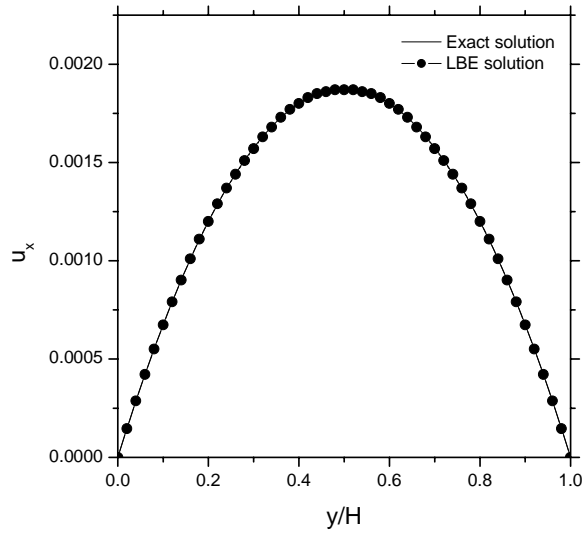


Figure 3.5: Comparison of axial velocity profile

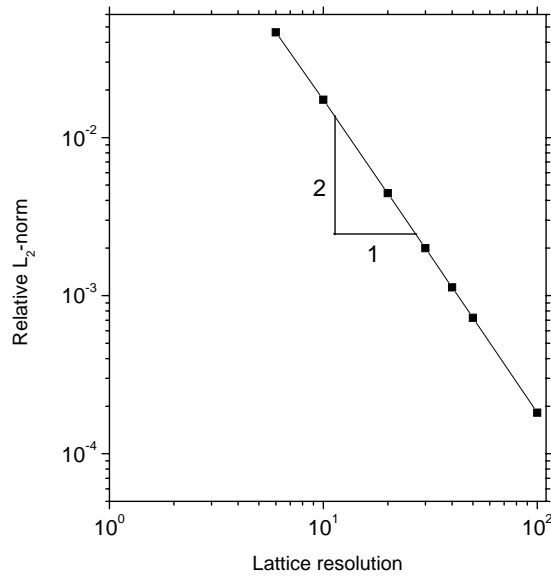


Figure 3.6: Dependence of relative L_2 -norm on lattice resolution

Figure 3.5 compares the exact axial velocity profile and the LBE solution using $n_x \times n_y = 50 \times 50$ grid points. Excellent agreement was obtained. Defining the L_2 -norm error as before, Eq. (2.26), Figure 3.6 shows the dependence of the relative L_2 -norm on the lattice resolution. The second order accuracy was indeed maintained.

3.4.2 Two-phase flow tests for LBE model

For the two-phase flow tests, we first look at the dynamics of the coalescence of two identical circular droplets. The second example is the relaxation of a deformed droplet driven by surface tension.

For the first example, initially two identical droplets with radius $R_i = 18.2$ were placed very close to each other with their centers at the centerline of computation domain $x = n_x/2$. The higher density/liquid phase is inside the droplet and lower density/vapor phase is outside. The computational resolution is 100×100 with periodical boundary conditions employed in all directions. When the simulation starts, the droplets will coalesce immediately. Figure 3.7 shows a snapshot of the droplet shapes at four different times. The symmetries about $x = n_x/2$ and $y = n_y/2$ are preserved. The droplet shape oscillation captured in Figure 3.7 is well known and is in agreement with other researchers' results [87].

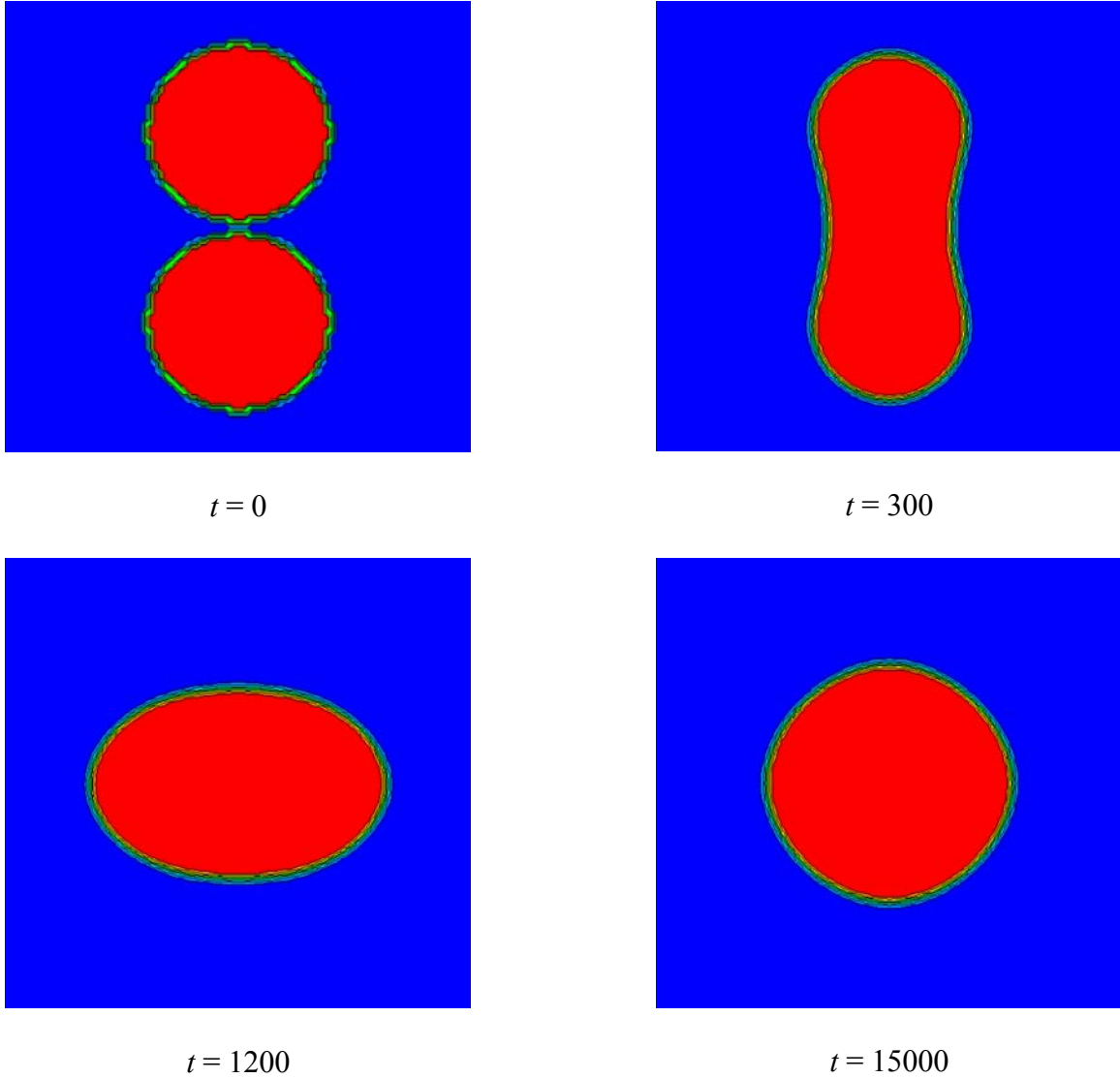


Figure 3.7: Snapshots of the droplet shape at different times ($\nu = 0.16667$, $\rho_l = 2.261$, $\rho_v = 0.122$). Red color represents liquid phase (high density) and blue color represents vapor phase (low density).

Figure 3.8 shows the droplet's radius at $y = ny/2$, i.e. the distance from the interface node at $y = ny/2$ (saddle node) to the center, as a function of time. The oscillation of the droplet shape is clearly observed, which is due to the surface tension. The relation $R_f = \sqrt{2}R_i$, where R_f is the final radius of droplet, and R_i is the initial radius (18.2) of two droplets, is maintained.

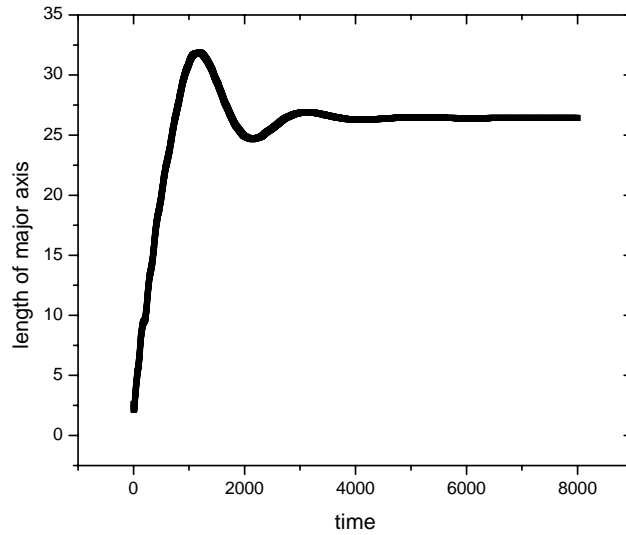


Figure 3.8: The radius at $y = ny/2$ as a function of time.

In the second test, a deformed droplet with an elliptical shape was placed initially at the center of the computational domain. The lengths of the major axis and minor axis are 20 and 10, located along the x and y axes, respectively. The computational domain used is 50×50 lattice units. Periodical boundary conditions are employed in all directions.

Due to the effect of surface tension, the deformed droplet will relax to a circular equilibrium shape with oscillation. Figure 3.9 illustrates the oscillations of the droplet. The separate frames show the shape of the droplet at different times, which oscillates by changing the length of the major axis and minor axis.

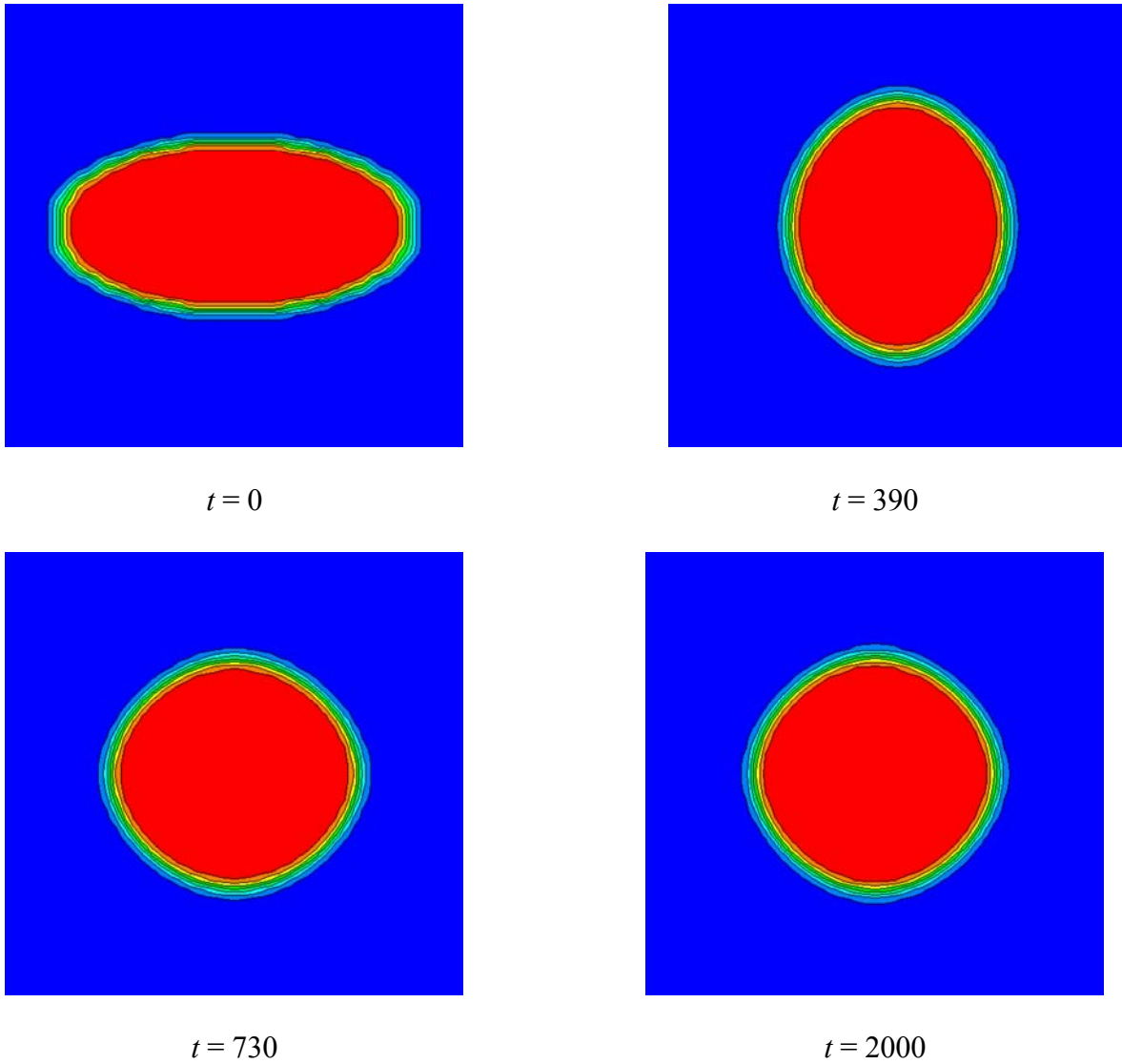


Figure 3.9: The oscillations of a deformed droplet with the initial shape of an ellipse at several times ($\nu = 0.16667$, $\rho_l = 2.307$, $\rho_v = 0.118$). Red color represents liquid phase (high density) and blue color represents vapor phase (low density).

The frequency of oscillation can be predicted by Lamb's equation [88]:

$$\omega = \sqrt{n(n^2 - 1) \frac{\sigma}{\rho_l a^3}} \quad (3.15)$$

where ω is the oscillation frequency, a in the equilibrium radius of the droplet, n represents the mode of the instability, and σ denotes surface tension. In his solution, Lamb didn't consider the

effects of the surrounding medium. Figure 3.10 shows the length of the major and minor axes changing with time and the oscillation can be clearly observed. However, we will not compare the quantitative results with Lamb's equation, because the surface tension is unknown. We will discuss the surface tension later in this chapter.

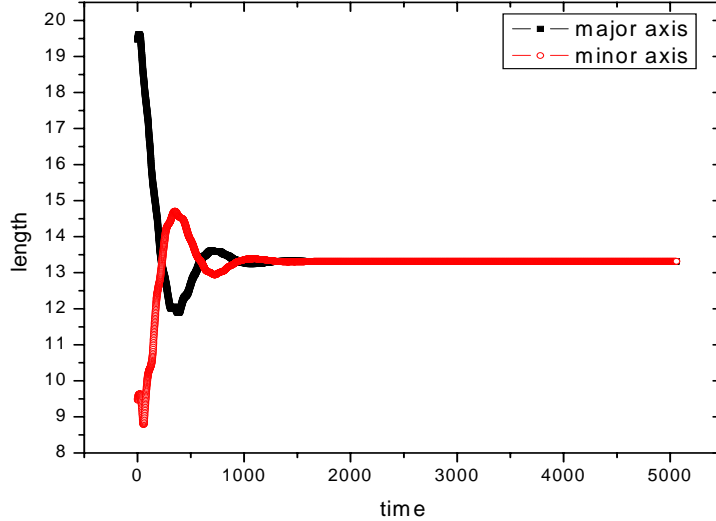


Figure 3.10: The evolutions of length of the major and minor axis with time.

3.5 PHASE EQUILIBRIUM AND WETTABILITY

To validate and illustrate the outcomes of the single component two-phase flow model, we now present some simulation results of a 3-D single component system. First, we observe the transitions from a single-phase fluid to a two-phase fluid. As mentioned before, the $\psi(\mathbf{x})$ is taken to be: $\psi(\mathbf{x}) = \rho_0 [1 - \exp(-\rho / \rho_0)]$, with $\rho_0 = 1.0$. Initially, the density is evenly distributed on a $50 \times 50 \times 50$ lattice with a small random perturbation. Periodical boundary conditions are applied in all three coordinate directions. Figure 3.11 shows the maximum and

minimum densities as functions of $|g_f|$, with $g_f < 0$ for the attraction between particles. When the fluid-fluid interaction strength g_f decreases under some critical value g_f^c , the system separates from a single phase into a heavier/liquid phase and a lighter/vapor phase. Figure 3.12 is the plot of the density ratio changing with $|g_f|$.

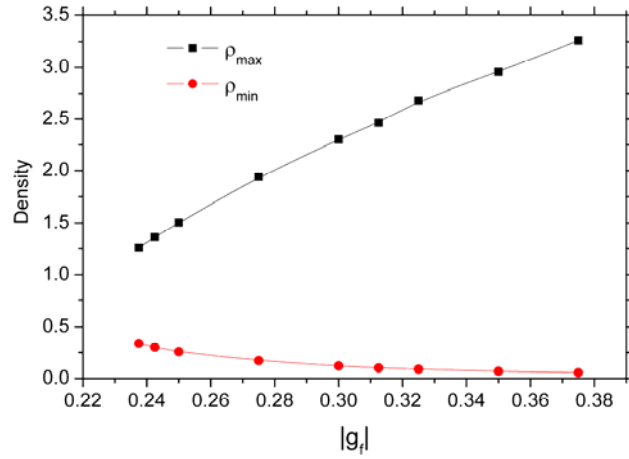


Figure 3.11: Maximum and minimum density values as a function of $|g_f|$.

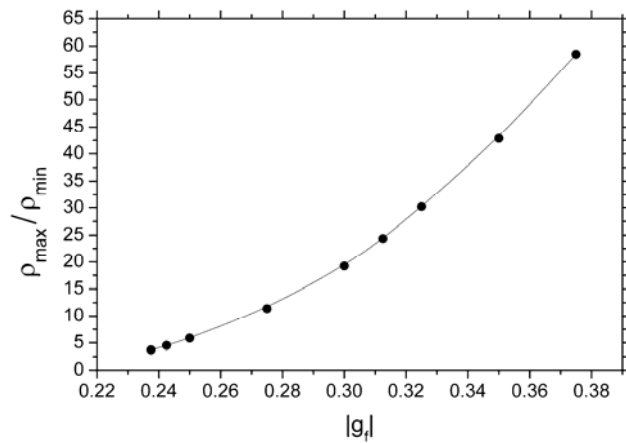


Figure 3.12: Density ratio as a function of $|g_f|$.

After finding the relation between the density ratio and the interaction strength g_f , we conducted some static bubble tests. Again, the $50 \times 50 \times 50$ lattice and periodical BCs are used in all of the tests. Initially, a droplet is placed at the center of the domain with a radius of $r_{init} = 10$. To ensure that the droplet's size will not expand or shrink too much, we specify that the initial density inside/outside the droplet is close to the maximum/minimum density obtained in the bifurcation test under the same g_f value. Otherwise, the droplet's radius is not controllable and the droplet may sometimes even expand to the boundaries. The droplet's radius oscillates for the first 800 time steps and then goes to a constant value. Each test was run for 10,000 time steps. At that point, the relative differences of the maximum magnitudes of the velocities at time step t and $t - 1000$ are on the order of 10^{-6} , which means that steady state is reached. For $g_f = -0.35$, the density and velocity fields in the xy -plane at $z = 25$ (the symmetry plane) are plotted in Figures 3.13(a) and 3.13(b), respectively. Other g_f values will give similar results.

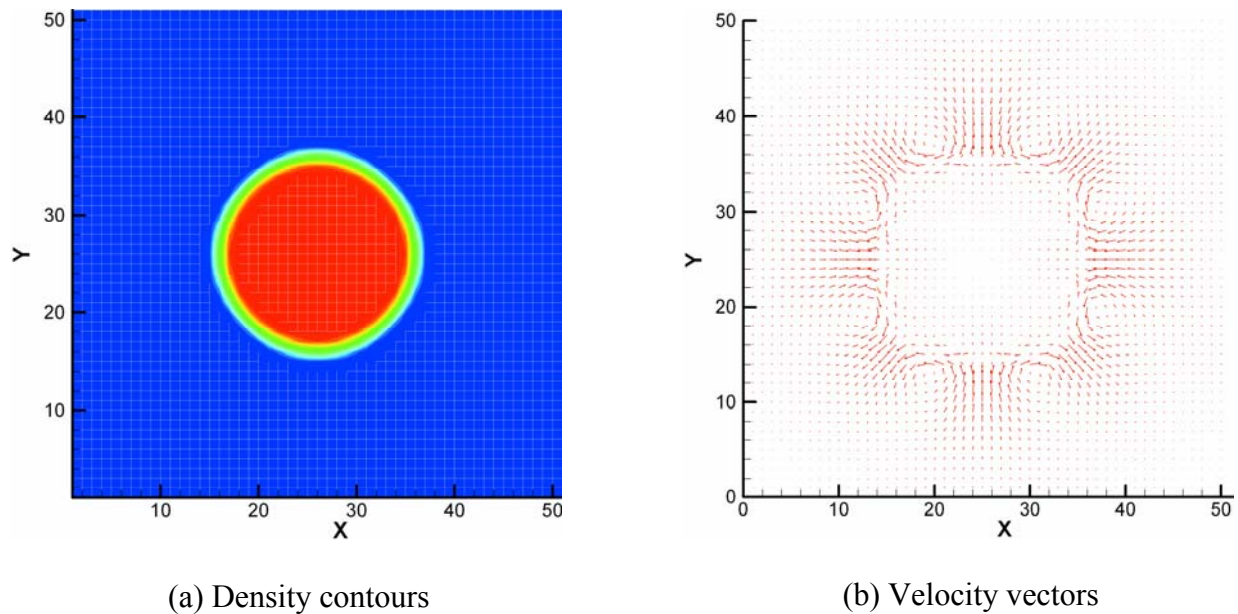


Figure 3.13: Density contours and velocity vectors in the xy -plane at $z = 25$.

The nonzero velocity vectors in Figure 3.13(b) indicate deviation from the real physical situation. These unphysical velocities are called spurious currents and reach their maximum value at the interface region [89]. The maximum magnitude of the spurious currents (hereafter denoted as $|\mathbf{u}^s|_{\max}$) as a function of $|g_f|$ is shown in Figure 3.14 (the dotted line is used to guide the eye). $|\mathbf{u}^s|_{\max}$ increases slowly before $|g_f|$ reaches 0.32 (the corresponding density ratio is around 30), and after that it grows rapidly. For $|g_f| = 0.3125$, its value is 0.01529, while for $|g_f| = 0.35$, the value is 0.05141. We know that the LBM is valid only in the incompressible limit $|\mathbf{u}|/c_s \rightarrow 0$, which requires that $|\mathbf{u}|$ is smaller than 0.13. In our later simulations, we restrict $|g_f| \leq 0.35$, with a highest density ratio of 42, which is adequate for many liquid-vapor systems. Some systems of interest, however, require a density ratio higher than 100. By changing the EOS, we can greatly reduce the spurious currents at these higher ratios. We will discuss this issue in chapter 4.

We also conducted some static bubble tests with a solid wall interaction by replacing the periodical BCs in the y and z directions with wall BCs. Similar density and velocity fields were obtained and the spurious currents did not increase.

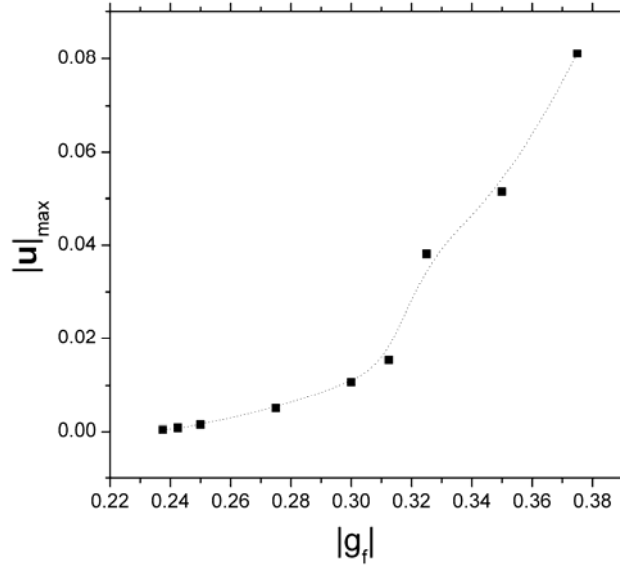


Figure 3.14: The maximum magnitude of spurious currents changing with $|g_f|$

A contact angle θ ($0 \leq \theta \leq 180^\circ$) is defined as the angle made at the point that the fluid-fluid and the fluid-solid interface meet (see Figure 3.15). The contact angle determines the degree of wettability of a fluid phase with respect to the solid phase. Usually, a fluid is regarded as wetting (the fluid tends to wet the surface) for a contact angle less than 90° , and nonwetting (the fluid has less affinity to the solid surface) if the contact angle is greater than 90° [90].

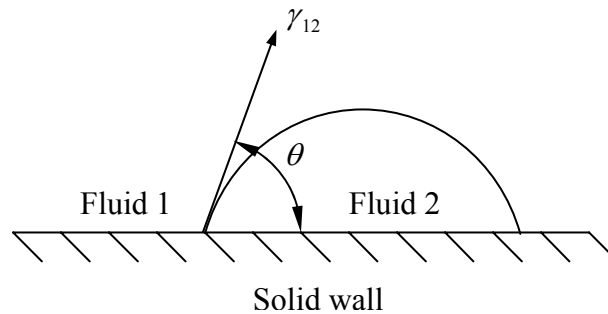


Figure 3.15: Contact angle between a fluid-fluid interface and a solid wall. γ denotes the interfacial tension between fluids, and θ denotes the contact angle.

In LB simulations, the static contact angle can be adjusted by changing the value of g_w (negative for a wetting fluid and positive for a nonwetting fluid) or even by changing the form of Eq. (3.10); say, e.g., changing the local density term in Eq. (3.10) to some function of local density. In this way, we can easily control the wettability.

We conducted several tests on the wettability of the fluid. In our simulations, initially a half-drop of liquid with radius 10.0 is placed at the bottom of solid wall with its center at the geometric center of the bottom wall. The lattice size is $50 \times 50 \times 50$ with periodical BCs in the x direction and solid wall BCs in the y and z directions. Figure 3.16 shows two contact angles obtained by adjusting g_w . Figure 3.17 gives the corresponding velocity fields. The maximum magnitude of the spurious current $|\mathbf{u}^s|_{\max}$ stays at the same level as in the static bubble test.

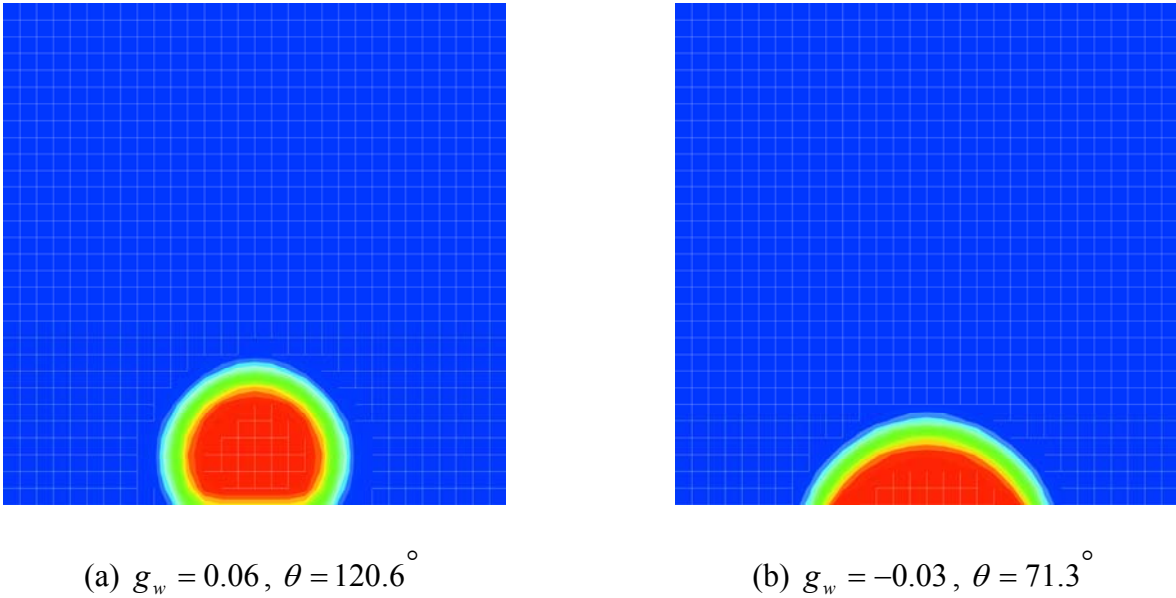


Figure 3.16: Density contours for different values of g_w (different wettabilities)

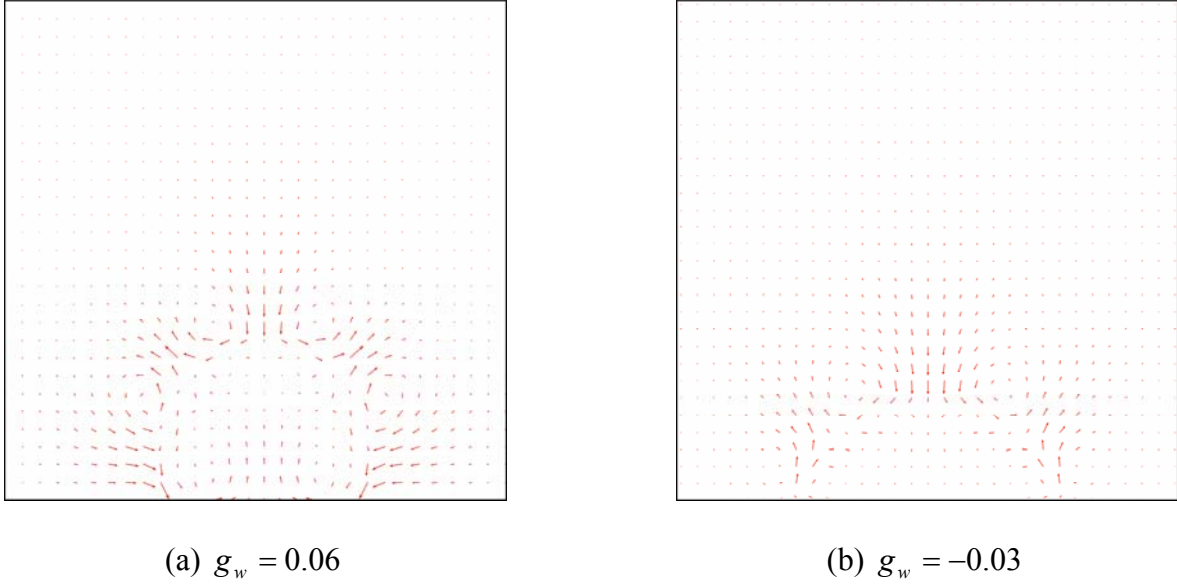


Figure 3.17: Velocity fields for different values of g_w

Figure 3.18 plots the contact angle varying with g_w , which is almost a linear relation. This is in agreement with the work of other researchers [91]. For large g_w values ($g_w > 0.08$), after the half liquid drop is placed on the bottom, because of the large interaction between the fluid and solid, the liquid phase in contact with the solid will shrink very fast and will generate some unphysical phenomena. In this case, g_w must be increased step by step until a stable contact angle is obtained.

We also conducted simulations for a different form of equation (3.10). For example, instead of using $\rho(\mathbf{x})$, we used the “effective mass” i.e., $\psi(\mathbf{x}) = \rho_0 [1 - \exp(-\rho / \rho_0)]$. For this case, the linear relation between the contact angle θ and the fluid-solid interaction strength g_w is still obtained. However, the slope will change. For the effective mass case, the slope is smaller than using the local density directly. Also, different values of g_w for the liquid and vapor phase can be used. If these values are properly specified, the linear relation between the contact angle θ

and the liquid-solid interaction strength g_w^l will again be obtained (in this case, the vapor-solid interaction strength g_w^v is fixed).

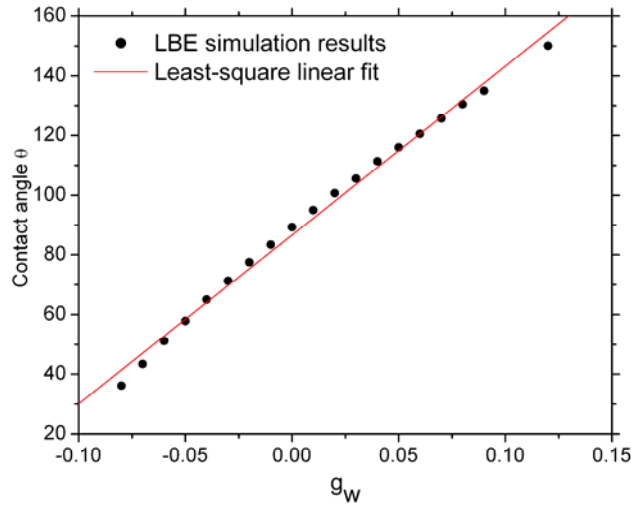


Figure 3.18: The relation between the contact angle θ of the drop and the fluid-solid interaction strength g_w .

One necessary point with respect to these results is that although any static contact angle can be obtained, there is no guarantee that the fluid dynamics near the contact line are correctly simulated [25]. The details of this fluid-solid interaction are not fully understood and require further research.

3.6 SURFACE TENSION IN THE LBE MODEL

Interfacial and surface tensions are important characteristics of two-phase flow systems since they influence many physico-chemical processes. In physical terms, the surface tension is an effect within the surface layer of a fluid that causes the layer to behave as an elastic sheet. Surface tension is caused by the attraction between the molecules of the fluid, due to the various

intermolecular forces. In this section, we will show the limitation of the SC LBE model in dealing with surface tension and then give our remedy.

3.6.1 Surface tension in original SC LBE model

It is argued that one limitation of the SC LBE model is related to the way it represents capillary effects, which can be quantified by the surface tension coefficient σ . Shan and Chen have shown that in the case of the flat interface, the surface tension coefficient can be calculated from the following equation [70]:

$$\sigma = \frac{c^2}{D+2} \int_{-\infty}^{+\infty} \sqrt{p^*} \frac{d^2 \sqrt{p^*}}{dn^2} dn \quad (3.16)$$

where c is the lattice constant, D is the dimension of space, n is the direction normal to the interface, and p^* is the non-ideal part of the EOS, defined as: $p^* = p - c_s^2 \rho$. This means the surface tension coefficient is coupled to the EOS through p^* . For a chosen “effective of mass” $\psi(\mathbf{x})$ and “strength of interparticle interactions” g_f , the σ is fixed and there is no freedom to vary it. In order to determine the surface tension numerically, we introduce the Laplace law [92], which states:

$$p_i - p_o = \frac{\sigma}{R} \quad (3.17)$$

where p_i and p_o are the pressure inside and outside the bubble/droplet, respectively, and R is the radius of the bubble/droplet. Therefore, in practice, the surface tension of the SC model is “empirically” determined by generating circular bubbles/droplets of different radii in a periodic domain, and evaluating the slope of the “pressure difference vs. inverse of radius” relation.

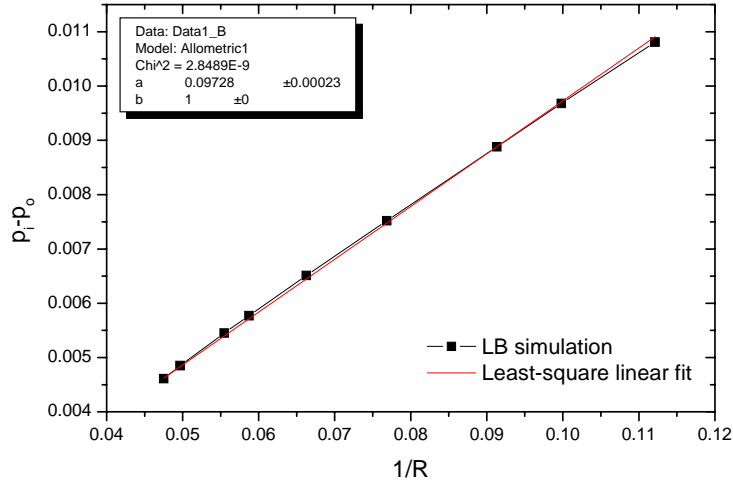


Figure 3.19: Test of the Laplace law. The slope (i.e. the surface tension) is 0.09728 and the coefficient of determination is 0.99943.

Figure 3.19 shows the verification of the Laplace law for $g_f = -0.3$, and the linear relation is well satisfied. By measuring the slope, the surface tension was found to be 0.09728 in lattice units and the coefficient of determination is 0.99943. However, since σ is related to g_f , one needs to change g_f in order to change surface tension, which is inconvenient, if not inappropriate. We therefore propose another way of changing surface tension.

3.6.2 Changing surface tension in the SC LBE model

Microscopically, surface tension is caused by the various intermolecular forces. Therefore, in order to obtain flexibility in modeling surface tension, one might choose to introduce an additional force term in the fluid-fluid interaction to mimic the contribution made by surface tension. We define

$$\mathbf{F}_s = \kappa \psi(\rho) \nabla \nabla^2 \psi(\rho) \quad (3.18)$$

as an additional force associated with the surface tension, where $\psi(\rho)$ is the effective mass, and κ determines the strength of the surface tension. It can be shown that by introducing \mathbf{F}_s into the fluid-fluid interaction term, the macroscopic equations recovered from the LBE using Chapman-Enskog expansion procedure are [72]:

$$\frac{\partial \rho}{\partial t} + \nabla \cdot (\rho \mathbf{u}) = 0 \quad (3.19a)$$

$$\rho \left[\frac{\partial \mathbf{u}}{\partial t} + (\mathbf{u} \cdot \nabla) \mathbf{u} \right] = -\nabla p + \nabla \cdot [\rho \nu (\nabla \mathbf{u} + \mathbf{u} \nabla)] + \mathbf{F} + \kappa \psi(\rho) \nabla \nabla^2 \psi(\rho) \quad (3.19b)$$

The above equations only differ from the N-S equations by the additional term, $\kappa \psi(\rho) \nabla \nabla^2 \psi(\rho)$, which contributes exclusively to the surface tension. Also the EOS remains the same.

For numerically evaluating the \mathbf{F}_s term, one can use the five-point scheme for the Laplace term $\nabla^2 \psi(\rho)$ and the six-point scheme discussed before for the gradient term $\nabla \psi(\rho)$ (both for 2-D case):

$$\nabla^2 \psi(\rho) = \psi(i+1, j) + \psi(i-1, j) + \psi(i, j+1) + \psi(i, j-1) - 4\psi(i, j) \quad (3.20)$$

Figure 3.20 shows the estimation of surface tension from the curvature (1/radius) and pressure difference between the inside and outside of simulated bubbles/droplets. By changing the strength of the surface tension κ , linear relations with different slopes were obtained, which means the surface tension coefficients are different for different κ values. For example, by measuring the slope, we found that for $\kappa = -0.3$, $\sigma = 0.08214$, and for $\kappa = 0.3$, $\sigma = 0.11096$.

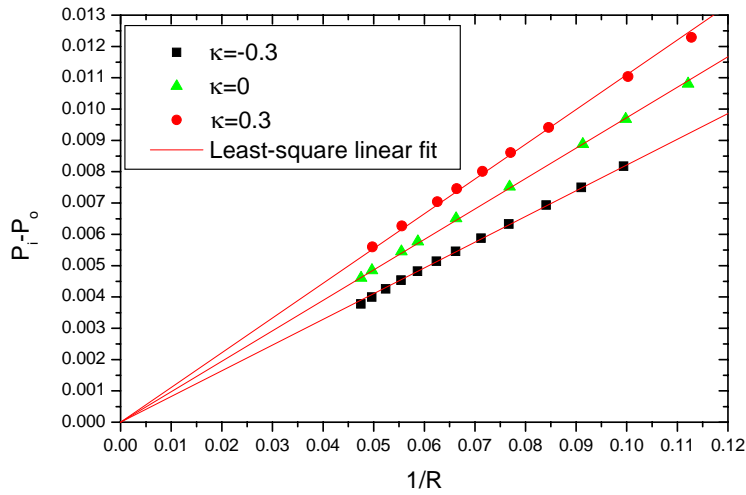


Figure 3.20: Estimation of surface tension from curvature (1/radius) and pressure difference between the inside and outside of simulated bubbles/droplets.

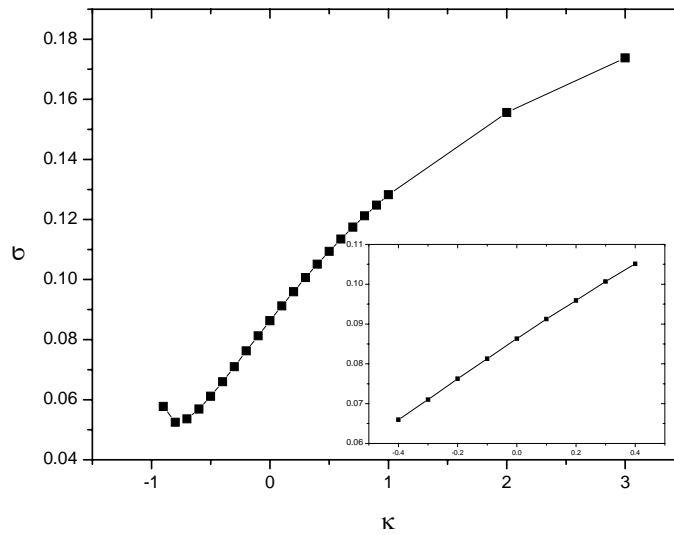


Figure 3.21: Surface tension coefficient σ as a function of the strength of the surface tension κ . The inset diagram shows the small κ values: $-0.4 \leq \kappa \leq 0.4$.

Figure 3.21 gives the surface tension coefficient σ as a function of the strength of the surface tension κ . The surface tension will increase when κ increases. In the small κ range ($-0.4 \leq \kappa \leq 0.4$), a linear relation exists between σ and κ , as shown in the inset diagram. For

small surface tension, a bubble/droplet can no longer hold a circular shape due to insufficient surface tension.

Figure 3.22 shows the density contours at $\kappa = -0.9$, and the non-circular shape can be clearly observed. The curvature is then different from that of the circular case, which results in an increase in surface tension as κ decreases, as shown in Figure 3.21 at small κ values.

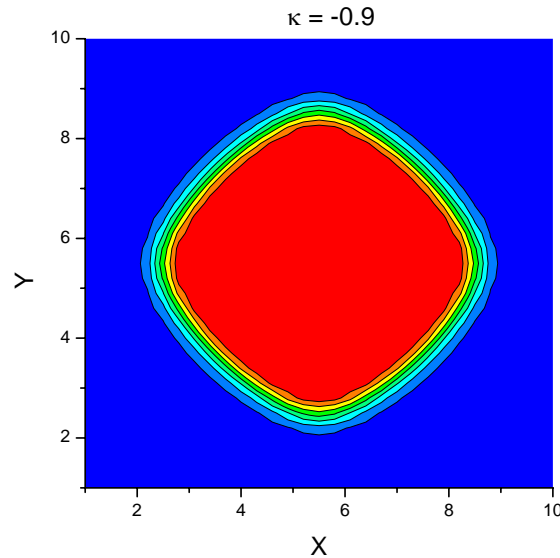


Figure 3.22: Density contours at $\kappa = -0.9$.

When the bubble/droplet shape is no longer circular, continuing to decrease κ will cause the code to become unstable and fail. We think the reason for this is that as surface tension decreases, the spurious current will increase, and finally the large spurious current will make the simulation unstable. Figure 3.23 gives $|\mathbf{u}^s|_{\max}$ as a function of κ , which verifies our speculation. For $g_f = -0.3$, the maximum and minimum achievable surface tensions are 0.17382 and 0.0525, respectively. Compared with the base case of $\kappa = 0$, we can increase σ by about 78.68% and decrease it by about 46.03%.

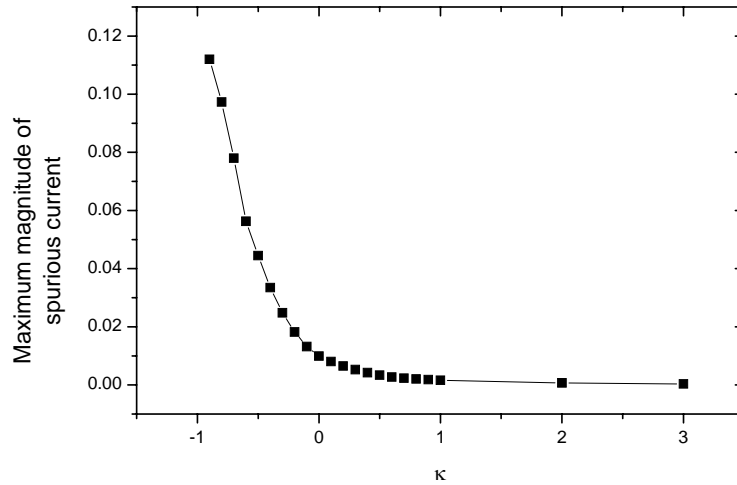


Figure 3.23: Maximum magnitude of spurious current as a function of κ .

The abovementioned tests were only conducted for the static bubbles/droplets. In order to test the dynamic behavior of surface tension, we conducted simulations of capillary wave dispersion. The 2-D system with length L and height H is periodical in both the x and y directions. Initially, a liquid phase was put in the center of the domain with a height equal to $H/4$. After the system reaches steady state, the position of the interface was measured. Then a wave was initialized as a sinusoidal curve around $y = H/2$ of one wavelength L and amplitude a , as seen in Figure 3.24. The system was then allowed to relax to equilibrium under the influence of capillary and viscous forces only (no gravity applied). At each time step, the position of the interface was measured and the result was a damped standing wave (see Figure 3.25). This curve was used to find the oscillation frequency and damping rate of the wave. In the simulation, the positions of the upper interface and lower interface are added together to filter out small fluctuations.

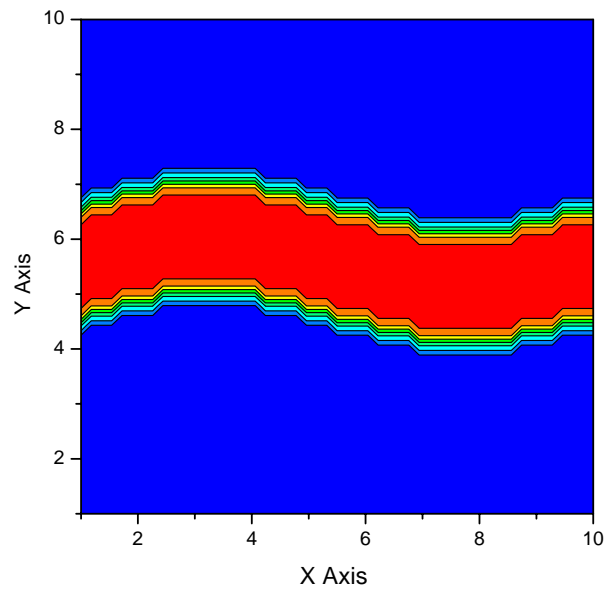


Figure 3.24: Simulation set up and wave initialization.

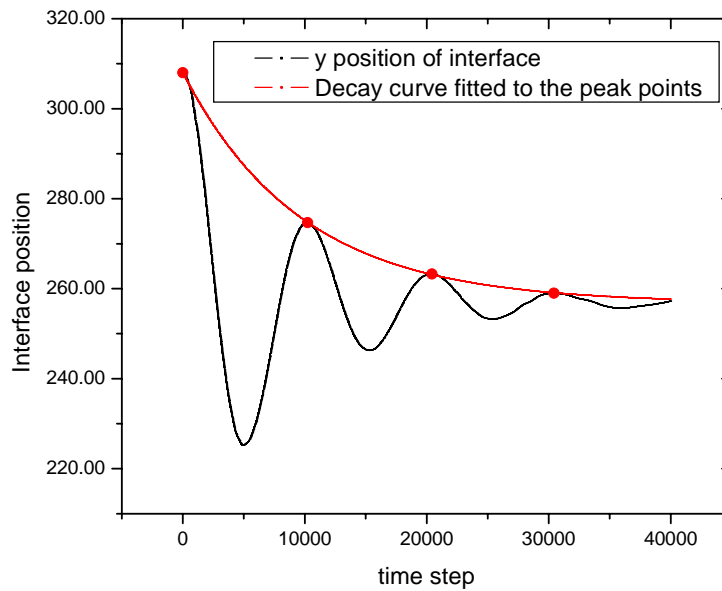


Figure 3.25: The y position of the capillary wave interface as a function of time. The red line is the exponential curve fitted to the peak points (dots).

For $a/L \ll 1$, the analytical solution of such a wave is obtained by potential flow theory [93]:

$$\omega^2 = \frac{\sigma}{\rho_1 + \rho_2} k^3 \quad (3.21a)$$

$$\gamma = 2\nu k^2 \quad (3.21b)$$

where ω is the wave frequency, γ is the damping rate, ρ_1 and ρ_2 are the densities of two phases, and k is the wave number given by $k = 2\pi/L$, where L is the wavelength. This relation therefore provides a dynamic measurement of surface tension. The oscillation of the wave can be expressed in the form of: $Ae^{-\gamma t} \cos(\omega t + \psi) + C$.

In Figure 3.25, the system resolution is 256×256 . The initial amplitude of the wave is $0.1 \times 256 = 25.6$ and viscosity is $1/12$. We first fit the peak points to the exponential decay curve in the form of: $y = y_0 + Ae^{-\gamma(t-t_0)}$. The parameters we obtained are: $y_0 = 256.85033$, $A = 51.14003$, $t_0 = -5.4925E-7$, and $\gamma = 1.02583E-4$. The γ predicated by the potential flow theory is: $2 \times \frac{1}{12} \times \left(\frac{2\pi}{256}\right)^2 = 1.003988E-4$. Comparing γ with the theoretical value, the relative error of simulation result is about 2.17%.

We then conducted simulations using different wavelengths. The simulation results of $k - \omega$ relation are given in Figure 3.26 together with the theoretical predictions obtained by Eq. (3.21a), with σ obtained from static bubble/droplet tests.

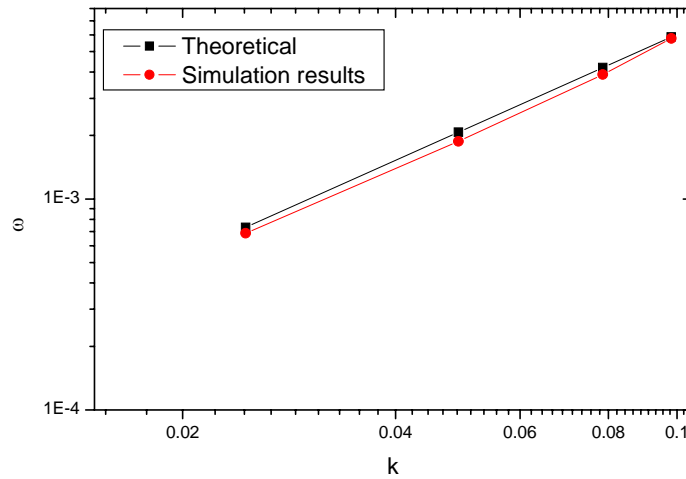


Figure 3.26: The dispersion relation (angular frequency ω vs. wave number k). Simulation results using $\kappa = 0$ are compared with the corresponding analytical solution from potential theory, Eq. (3.21a).

On the other hand, using Eq. (3.21a), we can find the surface tension coefficient by measuring the angular frequency of the wave. We found that for $\kappa = 0$, the error between surface tension measured statically and dynamically is 6.19% and for $\kappa = -0.3$ the error is 14.24%, both calculated using the static surface tension as base. Although the error is large for the $\kappa = -0.3$ case, it is comparable with other researchers' results [94]. Furthermore, this does reflect the trend of surface tension variation when changing the κ value. We think the statically measured surface tension is more accurate because there are more sources of error encountered in the dynamic case, which includes the error induced by the measurement of interface position, measurement of angular frequency, and error of initializing the wave. Furthermore, even the potential flow theory itself is an approximation and needs several assumptions, like a small wave amplitude, etc. Therefore, the static bubble/droplet test is preferred in an effort to determine the exact surface tension of the system.

3.7 DISCUSSION

In this chapter, we have demonstrated the applicability of the LBE method in simulating both single phase flow and two-phase flow systems. Second order accuracy was obtained for the single phase flow benchmark tests. Two-phase flow benchmark tests showed the relaxation process of the bubble/droplet, which is in agreement with other researchers. It is demonstrated that the SC single component two-phase LBE model has the ability to simulate phase separation, variable wettability, and different EOS as well as complex BCs. It is argued that one limitation of SC LBE model is that surface tension coefficient of this model is coupled to the EOS and there is no freedom to vary it. In order to achieve flexible surface tension, we proposed an additional force term $\mathbf{F}_s = \kappa\psi(\rho)\nabla\nabla^2\psi(\rho)$, which accounts for the contribution of surface tension, to be incorporated into the fluid-fluid interaction. We then measured the surface tension both statically and dynamically. It has been shown that by adopting this additional force term, we can increase surface tension by about 78.68% and decrease it by about 46.03% for the simulated case.

4.0 EQUATIONS OF STATE IN THE LBE MODEL

4.1 INTRODUCTION

Equations of state attempt to describe the relationship between temperature, pressure, and volume (or density) for a given substance or mixture of substances. Shown in Eq. (4.1) is the simplest EOS -- the ideal gas law, which is a linear relationship between pressure p and density ρ when temperature T is held constant and R is gas constant.

$$p = \rho RT \quad (4.1)$$

Although reasonably accurate for gases at low pressures and high temperatures, the ideal gas law becomes increasingly inaccurate at higher pressures and lower temperatures. This is due to the non-idealities coming from the non-negligible volume of gas molecules and from the attractive interactions between those molecules. In 1873, van der Waals considered these non-idealities and proposed the famous van der Waals (vdW) EOS [95]:

$$p = \frac{\rho RT}{1 - b\rho} - a\rho^2 \quad (4.2)$$

where a is the attraction parameter and b is the repulsion parameter (or effective molecular volume). Accordingly, the first term of the RHS is called the attraction term and the second term of the RHS is called the hard sphere term. Although this equation is superior to the ideal gas law and does predict the formation of a liquid phase, the agreement with experimental data is limited. Following the van der Waals equation, subsequent researchers proposed several other modern EOS, which have only slightly greater complexity but are much more accurate. Some well-

known ones include the Virial equation, Redlich-Kwong EOS, Peng-Robinson EOS, and Carnahan-Starling EOS.

To describe the implementation of an adaptable EOS, we will first return to our one-component two-phase LBE model. As discussed in Chapter 3, if the interaction force is given by Eq. (3.5), then the EOS of the system is given by:

$$p = c_s^2 \rho + \frac{c_0}{2} g[\psi(\rho)]^2. \quad (4.3)$$

If there is no interaction force, then the fluid will behave like an ideal gas. Theoretically, by changing the form of $\psi(\rho)$, different EOS can be obtained.

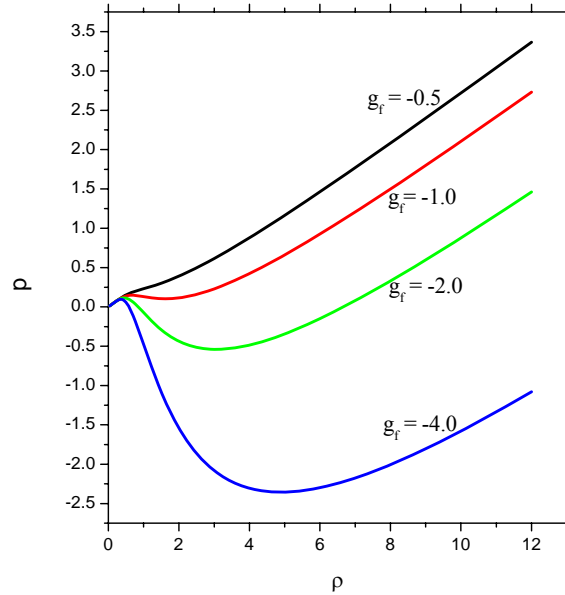


Figure 4.1: Pressure-density relationship of the SC EOS under different g_f values.

In the original paper of SC, the “effective mass” was taken to be: $\psi(\mathbf{x}) = \rho_0[1 - \exp(-\rho / \rho_0)]$. Therefore, the corresponding EOS (hereafter denoted as the SC EOS) is:

$$p = \frac{\rho}{3} + \frac{c_0}{2} g \rho_0^2 \left[1 - \exp\left(-\frac{\rho}{\rho_0}\right) \right]^2 \quad (4.4)$$

which gives a non-monotonic pressure-density relationship, as seen in Figure 4.1. From Figure 4.1, we can note that the SC EOS gives a high compressibility for the liquid phase, even higher than the vapor phase, which is unrealistic. It is argued that this is due to the lack of a repulsive potential between particles as the density increases in the SC model [96]. We also tested a different form of the “effective mass” mentioned in other papers, i.e. $\psi(\mathbf{x}) = \psi_0 \exp(-\rho_0 / \rho)$ [82]. Although this gives us flexibility in choosing ψ_0 and ρ_0 , this effective mass generates an EOS with a similar form and characteristics as the SC EOS, i.e. the unwanted high compressibility for the liquid phase.

Furthermore, after a thorough review of the literature, it appears that all of the papers using the SC model adopted only the SC EOS and no other EOS have been utilized [79, 80, 81]. There is also a lack of thorough investigations of different EOS for other multi-phase LB models [73, 97]. Therefore, it is worthwhile to study the performance of the SC model under different EOS. We will compare the performance of different EOS in this chapter by analyzing the simulation results and by comparing the results with real fluid properties.

4.2 CRITERIA USED IN EVALUATING EQUATIONS OF STATE

In this section, we will use the SC EOS to demonstrate the criteria related to the evaluation of an EOS. We know that at the critical point, both the first and second order pressure derivatives with respect to the density are zero, i.e.:

$$\left(\frac{\partial p}{\partial v}\right)_T = \left(\frac{\partial^2 p}{\partial v^2}\right)_T = 0 \quad (4.5)$$

For the SC EOS, one can obtain the critical properties as follow: $\rho_c = \rho_0 \ln 2$ and $g_f^c = -2/(9\rho_0)$. In the SC EOS, the role of temperature is dictated by the fluid-fluid interaction

strength g_f . We can define temperature in the SC EOS as $T = -\frac{1}{g_f}$, and the critical

temperature becomes $T_c = -\frac{1}{g_f^c} = 4.5\rho_0$. Hence for $g_f < g_f^c$, at a single pressure, two densities

of the same material can coexist. However, to make phase separation occur, another condition must be satisfied also, i.e. $\rho_v < \bar{\rho} < \rho_l$, where ρ_v and ρ_l are the vapor density and liquid density at the specified temperature, and $\bar{\rho}$ is the average density of the whole system. This condition guarantees that the system is in the two-phase region. Otherwise the system is in the single phase region and no phase separation will occur.

4.2.1 Spurious currents

We have shown in Chapter 3 that there exist nonphysical velocities in the SC LBE model with a maximum value near the interface region, which are the so called spurious currents. Reducing the spurious currents is very important for LB two-phase simulations for the following reasons.

First, as discussed before, the LBE method is valid only in the incompressible limit $|\mathbf{u}|/c_s \rightarrow 0$.

If $|\mathbf{u}^s|_{\max}$ is too large, since we cannot separate spurious currents from real flow velocities, we therefore cannot get meaningful results. Second, large spurious currents will make the simulation unstable. Finally, we will propose a thermal two-phase flow model based on the SC model in Chapter 5, where the flow velocity is taken as the advection velocity of the temperature field [98].

Therefore, a more accurate velocity field is required in order to calculate an accurate temperature field. By lowering the spurious currents, we can lower the temperature fluctuations near the interface region caused by the spurious currents and obtain better local temperature distributions.

In this work we will investigate the spurious current levels for circular interfaces under different EOS, because the circular interface is more often encountered in real applications. Furthermore, even if the interface is undergoing some deformation and becomes no longer circular, the $|\mathbf{u}^s|_{\max}$ stays at the same level, as has been verified in the simulations. However, for comparison, we also conducted simulations for a two-phase system with a flat interface. We found that in this case the $|\mathbf{u}^s|_{\max}$ is much smaller – on the order of 10^{-14} .

4.2.2 Stable temperature range

Ideally, one wants a two-phase model that can handle the entire two-phase region, which is from the triple point to the critical point. However, as the temperature decreases in the two-phase region, the density ratio increases and the surface tension also increases. The overall effect results in higher spurious currents. Therefore, at a certain temperature, the spurious currents become so large as to make the scheme unstable. Figure 4.2 shows the $|\mathbf{u}^s|_{\max}$ as a function of reduced temperature (T/T_c) for the SC EOS. We define the lowest temperature which maintains the stability of the scheme as T_{\min} and compare these temperatures under different EOS.

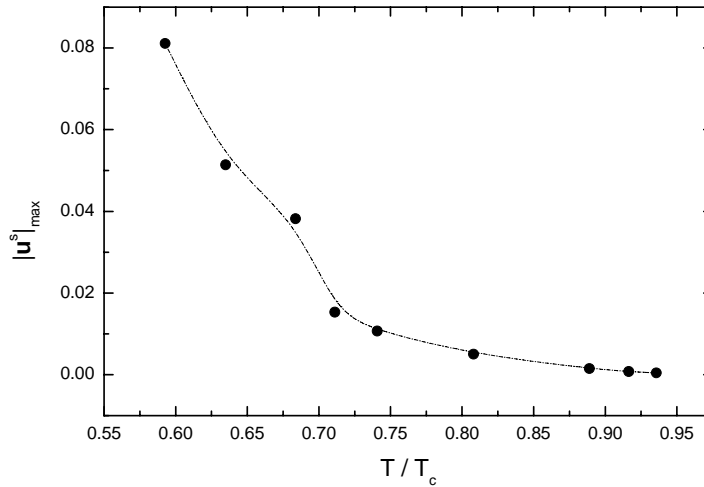


Figure 4.2: The maximum magnitude of spurious current changes with reduced temperature.

4.2.3 Coexistence curve

It has been argued that a serious limitation of the SC LBE model is that one cannot introduce a well-defined temperature, which is consistent with thermodynamics, into the model [75]. This is because the Maxwell equal-area construction [99] is not satisfied except for one special form of the effective mass, $\psi(\rho) = \psi_0 \exp(-\rho_0 / \rho)$, where ψ_0 and ρ_0 are arbitrary constants [70]. Therefore, to address the applicability of the SC model, it is important to check the deviation of the coexistence curve obtained from the simulation from the theoretical one that is predicted by the Maxwell equal-area construction.

4.2.4 Density ratio

In reality, for a vapor-liquid two-phase flow system, the density ratio between the liquid and vapor phase can easily be over 100:1. However, it is difficult for most LB schemes to deal with two phases with a high density ratio. For example, as reported in Swift's paper [74], the density

ratio obtained using the free-energy-based approach is less than 10:1, and the largest density ratio tested in the HCZ approach is 40:1 [97]. We found that by changing the EOS, one can reach density ratios higher than 1000:1. We will compare the achievable density ratios for different EOS accordingly.

4.3 INCORPORATING EQUATIONS OF STATE

In this work, we will compare the following EOS:

- (i) SC EOS
- (ii) vdW EOS
- (iii) Redlich-Kwong (R-K) EOS
- (iv) Redlich-Kwong Soave (RKS) EOS
- (v) Peng-Robinson (P-R) EOS
- (vi) Carnahan-Starling (C-S) EOS

Except for the SC EOS and C-S EOS, all of the other EOS are cubic in form. Furthermore, the vdW EOS and R-K EOS are two-parameter EOS, while the RKS EOS and P-R EOS are three-parameter EOS.

The vdW EOS, Eq (4.2), is the simplest and yet most famous cubic EOS. Although other modern EOS of only slightly greater complexity are much more accurate than the vdW EOS, we include it here to demonstrate some important concepts. From Eq. (4.3), we find that for any given EOS, the corresponding effective mass can be written as:

$$\psi(\rho) = \sqrt{\frac{2(p - c_s^2 \rho)}{c_0 g}} = \sqrt{\frac{2p^*}{c_0 g}} \quad (4.6)$$

where $p^* = p - c_s^2 \rho$ is the non-ideal part of the EOS. Substituting Eq. (4.2) into Eq. (4.6), we get:

$$\psi(\rho) = \sqrt{\frac{2\rho \left(\frac{RT}{1-b\rho} - a\rho - c_s^2 \right)}{c_0 g_f}} \quad (4.7)$$

The g_f value becomes unimportant in this case, because unlike in the SC EOS, we have a defined temperature in the vdW EOS. When calculating the interaction force and pressure using Eqs. (3.5) and (4.3), g_f is canceled out. The only requirement for g_f is to ensure that the whole term inside the square root is positive. This argument holds for other EOS also if the temperature is not a function only of g_f . For the vdW EOS, the critical properties are given by:

$$\rho_c = \frac{1}{3b}, \quad p_c = \frac{a}{27b^2}, \quad T_c = \frac{8a}{27Rb} \quad (4.8)$$

In our simulations, we set $a = \frac{9}{49}$, $b = \frac{2}{21}$ and $R = 1$. Then the critical density is $\rho_c = \frac{7}{2}$ and the critical temperature is $T_c = \frac{4}{7}$, both of which are in lattice units.

In an effort to relate these values to real physical properties, we use the concept of reduced properties [100]:

$$\rho_R = \frac{\rho}{\rho_c}, \quad p_R = \frac{p}{p_c}, \quad T_R = \frac{T}{T_c} \quad (4.9)$$

where the subscripts “ R ” and “ c ” denote the reduced property and critical property, respectively. According to the law of corresponding states, the reduced properties should be the same no

matter what kind of units are used, therefore: $\rho_R = \frac{\rho^{Lu}}{\rho_c^{Lu}} = \frac{\rho^{real}}{\rho_c^{real}}$, which gives $\rho^{real} = \rho^{Lu} \frac{\rho_c^{real}}{\rho_c^{Lu}}$.

Similarly, $p^{real} = p^{Lu} \frac{p_c^{real}}{p_c^{Lu}}$ and $T^{real} = T^{Lu} \frac{T_c^{real}}{T_c^{Lu}}$, where the superscripts “*real*” and “*Lu*” denote

real units and lattice units, respectively. In this way, one can easily convert a lattice property to a real property.

The other EOSs used in this paper are given below [101]:

R-K EOS:

$$p = \frac{\rho RT}{1 - b\rho} - \frac{a\rho^2}{\sqrt{T}(1 + b\rho)} \quad (4.10)$$

with $a = \frac{0.42748R^2T_c^{2.5}}{p_c}$, $b = \frac{0.08664RT_c}{p_c}$.

RKS EOS:

$$p = \frac{\rho RT}{1 - b\rho} - \frac{a\alpha(T)\rho^2}{1 + b\rho} \quad (4.11)$$

$$\alpha(T) = \left[1 + (0.480 + 1.574\omega - 0.176\omega^2)(1 - \sqrt{T/T_c})\right]^2 \quad (4.12)$$

with $a = \frac{0.42748R^2T_c^2}{p_c}$, $b = \frac{0.08664RT_c}{p_c}$.

P-R EOS:

$$p = \frac{\rho RT}{1 - b\rho} - \frac{a\alpha(T)\rho^2}{1 + 2b\rho - b^2\rho^2} \quad (4.13)$$

$$\alpha(T) = \left[1 + (0.37464 + 1.54226\omega - 0.26992\omega^2)(1 - \sqrt{T/T_c})\right]^2 \quad (4.14)$$

with $a = \frac{0.45724R^2T_c^2}{p_c}$, $b = \frac{0.0778RT_c}{p_c}$.

C-S EOS [102]:

$$p = \rho RT \frac{1 + b\rho/4 + (b\rho/4)^2 - (b\rho/4)^3}{(1 - b\rho/4)^3} - a\rho^2 \quad (4.15)$$

with $a = \frac{0.4963R^2T_c^2}{p_c}$, $b = \frac{0.18727RT_c}{p_c}$.

In the above EOS, the R-K EOS, RKS EOS and P-R EOS are classified as cubic EOS, in which the R-K EOS is a two-parameter EOS, using two parameters (T_c, p_c) ; the RKS EOS and P-R EOS are three-parameter EOS, with an additional parameter ω , which is the acentric factor. This additional parameter gives us more flexibility in modeling different fluids. For all of these cubic EOS, we set $a = \frac{2}{49}$, $b = \frac{2}{21}$ and $R = 1$ in our simulations. The C-S EOS is different from the above cubic EOS in that it modifies the hard sphere term of the vdW EOS, while all of the other cubic EOS modify the attraction term of the vdW EOS. For the C-S EOS, we set $a = 12$, $b = 4$, and $R = 1$ in our simulations.

4.4 SIMULATION RESULTS

In this section, we first compare the simulation results of three types of EOS, i.e. the SC EOS, vdW EOS and C-S EOS. Next, we compare the simulation results of all of the cubic EOS. Finally, we will compare our simulation results with some real fluid data.

4.4.1 Comparison of different types of equations of state

Figure 4.3 shows the variation of $|\mathbf{u}^s|_{\max}$ with the density ratio for the vdW EOS, which is close to a linear relation. The lowest temperature we can reach is $T_{\min} = 0.445 = 0.77875T_c$, since the scheme becomes unstable at temperatures lower than that value.

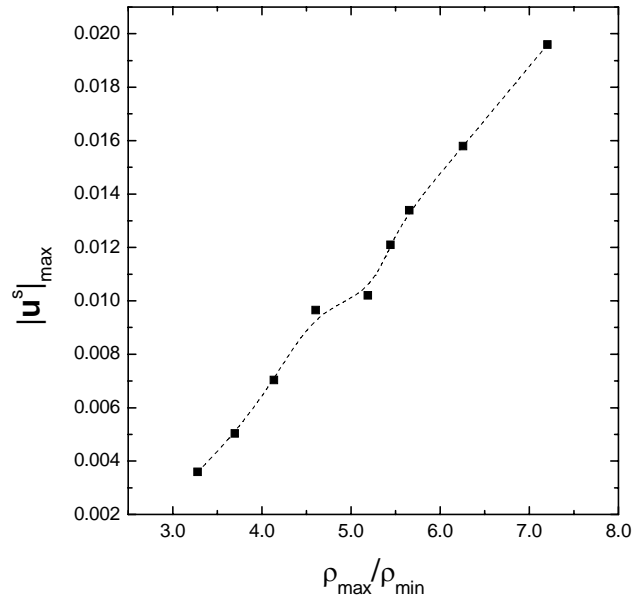


Figure 4.3: The maximum magnitude of the spurious current varying with the density ratio for the vdW EOS.

Figure 4.4 shows $|\mathbf{u}^s|_{\max}$ changing with the density ratio for the SC EOS and C-S EOS. The inset diagram shows the $|\mathbf{u}^s|_{\max}$ variation for density ratios smaller than 50. As can be seen from the inset, for a given density ratio, the C-S EOS generates much smaller spurious currents than the SC EOS. Furthermore, the C-S EOS provides a larger range of density ratios; e.g., when the density ratio equals 103.74, $|\mathbf{u}^s|_{\max}$ for the C-S EOS is only 1.74E-02, while for the SC EOS, when the density ratio equals 58.497, $|\mathbf{u}^s|_{\max}$ already reaches 8.11E-02. The critical temperature

for the C-S EOS is $T_c = 0.3773a/bR$. Therefore, the lowest temperature we can achieve for the C-S EOS is $T_{\min} = 0.2a/bR = 0.53T_c$, which is much lower than that of the vdW EOS.

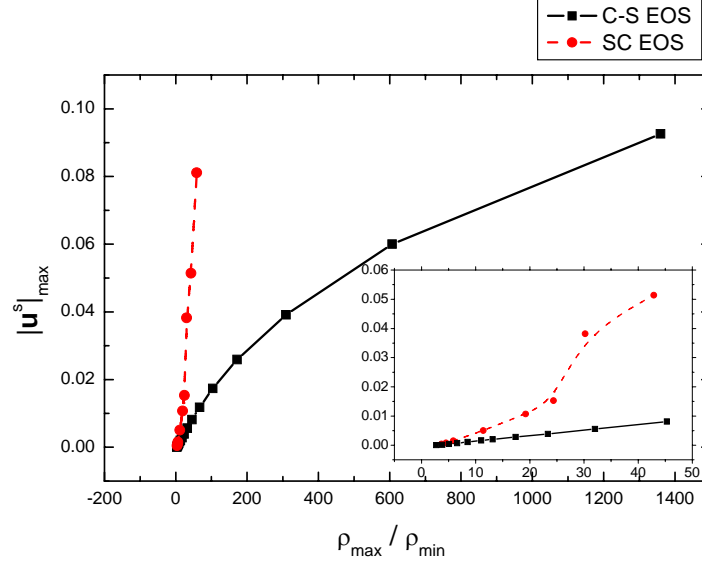


Figure 4.4: Maximum magnitude of the spurious current varying with the density ratio for the SC EOS and C-S EOS.

Table 4.1: Properties at T_{\min} for different EOS

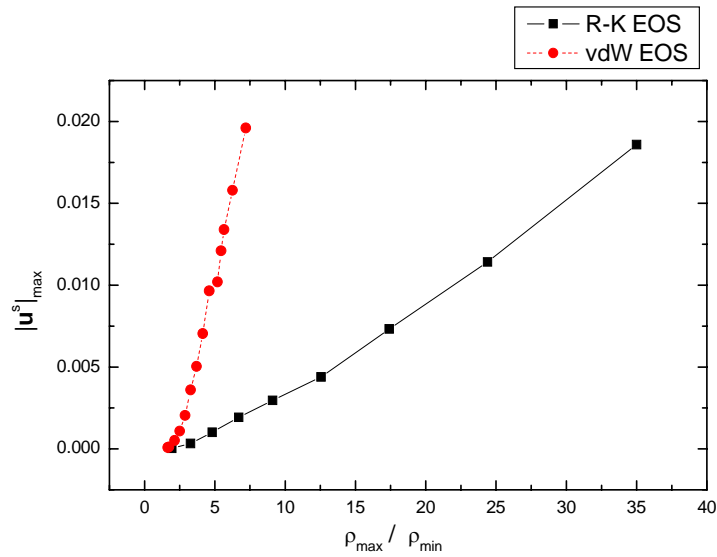
EOS	Critical Temperature (T_c)	T_{\min} / T_c	$ u^s _{\max}$	$\rho_{\max} / \rho_{\min}$
SC EOS	4.5	0.59259	0.0811	58.49753
vdW EOS	4/7	0.77875	0.019599	7.202862
C-S EOS	0.3773a/bR	0.5301	0.092571	1359.497

In Table 4.1, we compare the properties at T_{\min} for different EOS. We can see that at T_{\min} , the $|u^s|_{\max}$ for the vdW EOS is much smaller than that of the SC EOS and C-S EOS. We believe that unlike the other two EOS, where instability results from large spurious currents, for the vdW EOS, the instability comes from the EOS itself. Therefore, the vdW EOS is not suitable for a vapor-liquid system with temperatures much lower than the critical one. However, by replacing

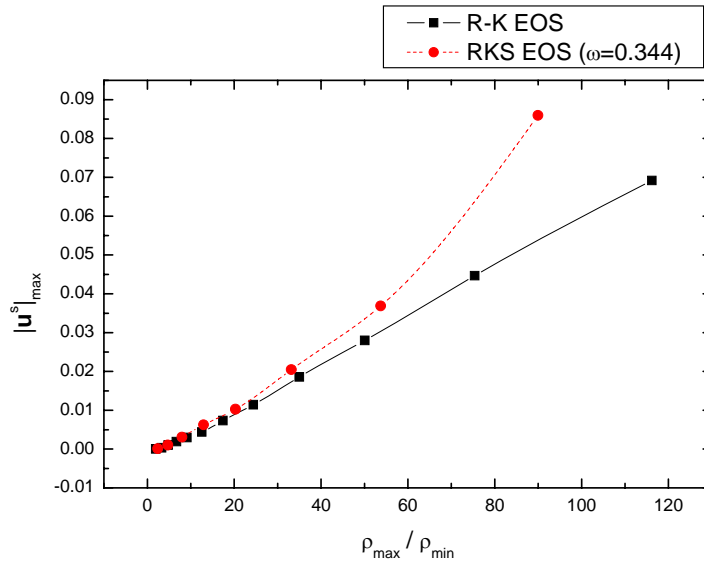
the vdW EOS with a more realistic modified form such as the C-S EOS, we will get a much better performance with a wider temperature range, higher density ratio and much smaller spurious currents. Furthermore, the C-S EOS is capable of handling a density ratio as high as 1000, which is large enough for most real applications.

4.4.2 Comparison of different cubic equations of state

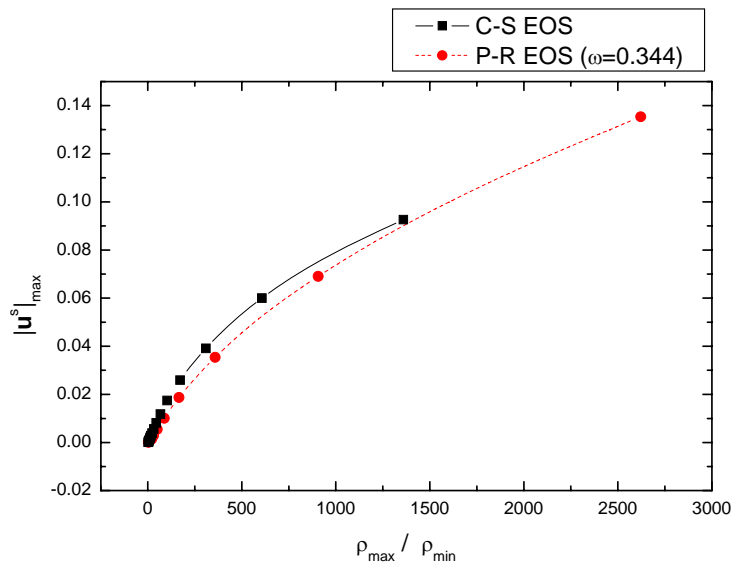
Since the C-S EOS, which is a modification of the vdW EOS, has a much better performance in simulating two-phase flow than the original vdW EOS, we now consider another way of modifying the vdW EOS, i.e. modifying the attraction term of the vdW EOS, which results in several cubic EOS.



(a) Comparison between the vdW EOS and the R-K EOS



(b) Comparison between the R-K EOS and the RKS EOS



(c) Comparison between the P-R EOS and the C-S EOS

Figure 4.5: The maximum magnitude of the spurious current variation with density ratio for different EOS.

Figure 4.5 gives the $|u^s|_{\max}$ variation with the density ratio for different cubic EOS. For the RKS EOS and P-R EOS, we set $\omega = 0.344$, which is the acentric factor of water. From Figure

4.5, we can see that at the same density ratio, all of the modified EOS have smaller $\left| \mathbf{u}^s \right|_{\max}$ values than the vdW EOS. The $\left| \mathbf{u}^s \right|_{\max}$ of the P-R EOS is even smaller than that of the C-S EOS. The P-R EOS can also handle a density ratio as high as 1000, with $\left| \mathbf{u}^s \right|_{\max} = 0.06902$ when the density ratio equals 905.9411. The $\left| \mathbf{u}^s \right|_{\max}$ values for the R-K EOS and RKS EOS are close to each other at lower density ratios. When density ratio is higher than 50, the R-K EOS gives a smaller $\left| \mathbf{u}^s \right|_{\max}$.

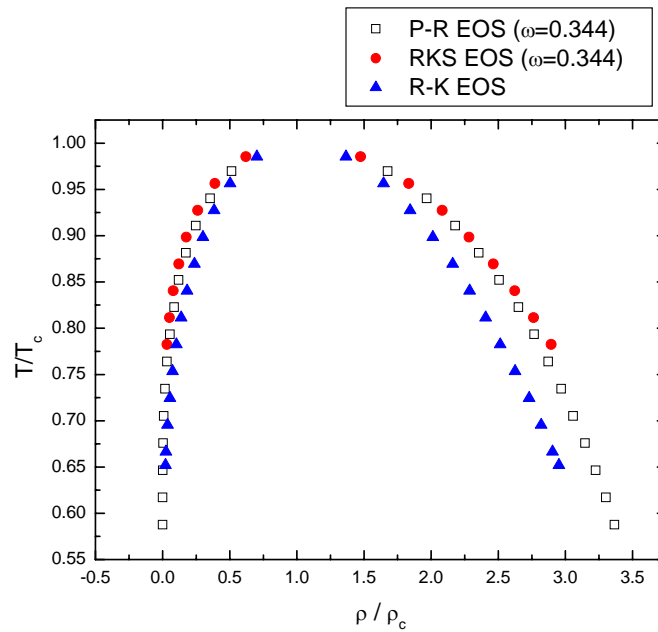


Figure 4.6: Coexistence curves for three EOS.

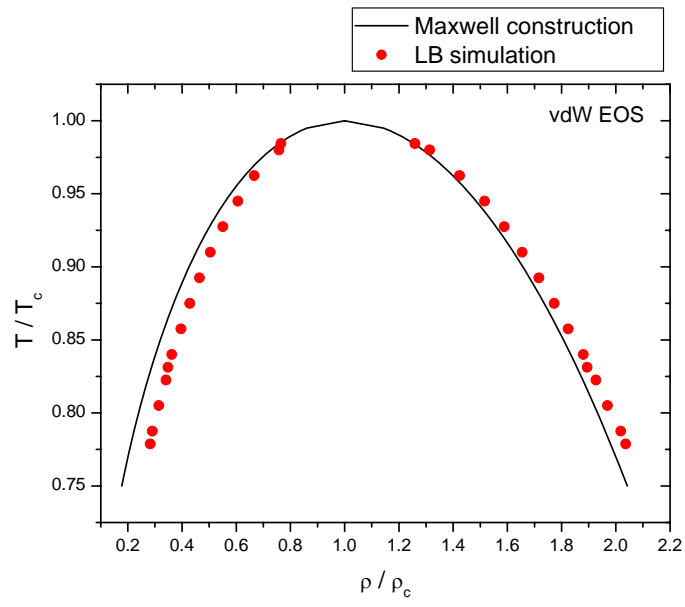
Figure 4.6 gives the coexistence curves obtained from the simulations for the various EOS. The coexistence curves of the RKS EOS and P-R EOS are quite close, which is to be expected, since we use the same acentric factor for these two EOSs. However, the P-R EOS can utilize a wider temperature range than the RKS EOS, because the P-R EOS has a much smaller $\left| \mathbf{u}^s \right|_{\max}$

under the same density ratio. The smallest reduced temperature (T_{\min} / T_c) is 0.64920, 0.78252 and 0.58771 for the R-K EOS, RKS EOS, and P-R EOS, respectively.

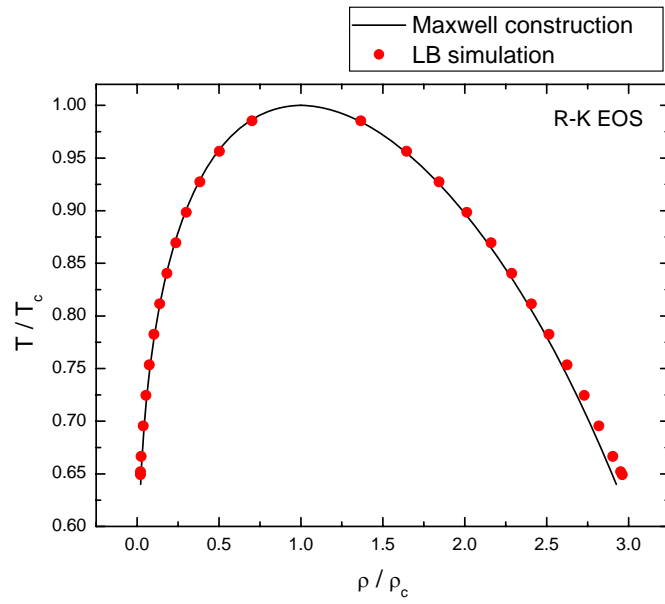
As discussed previously, it is very useful to evaluate these EOS by comparing the coexistence curves obtained from the simulations with the theoretical curves predicted by the Maxwell equal-area construction [103]. This comparison is given in Figure 4.7. From Figure 4.7(a), we can see that the simulated coexistence curve for the vdW EOS deviated remarkably from the theoretical values, especially at low temperatures. At T_{\min} , the relative error of the

density, i.e. $\frac{|\rho_{LB} - \rho_{exact}|}{\rho_{exact}}$, is 2.813% for the liquid branch and 33.83% for the vapor branch. As

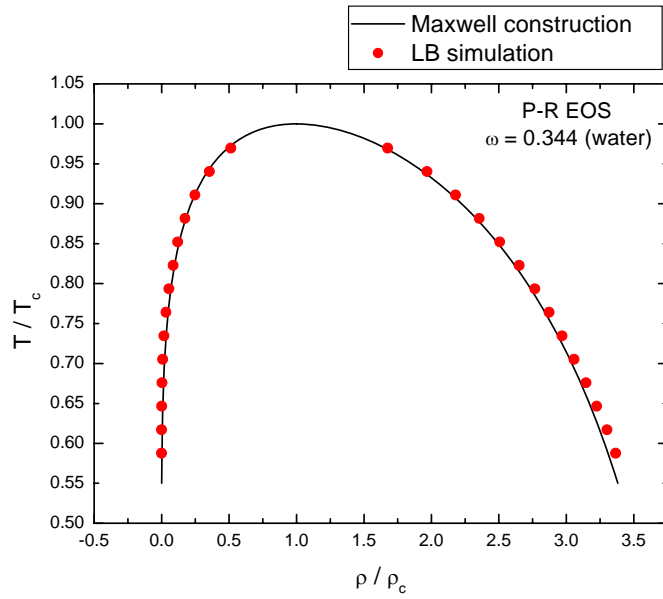
can be seen from Figures 4.7(b) and 4.7(c), for the R-K EOS and P-R EOS, the simulated coexistence curves fit well with the theoretical values. At T_{\min} , the relative error of density for the liquid branch is less than 2%. However, for the vapor branch, the relative error of the density can be quite large, although the absolute difference is very small. This is due to the nature of the EOS, since when the temperature is much lower than the critical temperature, the density ratio becomes quite high. For the P-R EOS, the density ratio can be higher than 1000, where even very small changes in the liquid density can cause large fluctuations of the vapor density. For this reason, we plot the coexistence curve of the vapor branch separately for the R-K EOS and P-R EOS in Figures 4.8(a) and 4.8(b). We can see although the coexistence curves deviated from the theoretical values, the trends of density changing with temperature are the same. Figure 4.9 shows the coexistence curve of the C-S EOS from simulation and the theoretical one obtained by equating the chemical potentials. Again, good agreement is obtained. For P-R EOS, the acentric factor can also be specified to fit the real fluid properties. Figure 4.10 gives the coexistence curve of the P-R EOS for $\omega = 0.011$, which is the acentric factor of methane.



(a) Coexistence curve of the vdW EOS

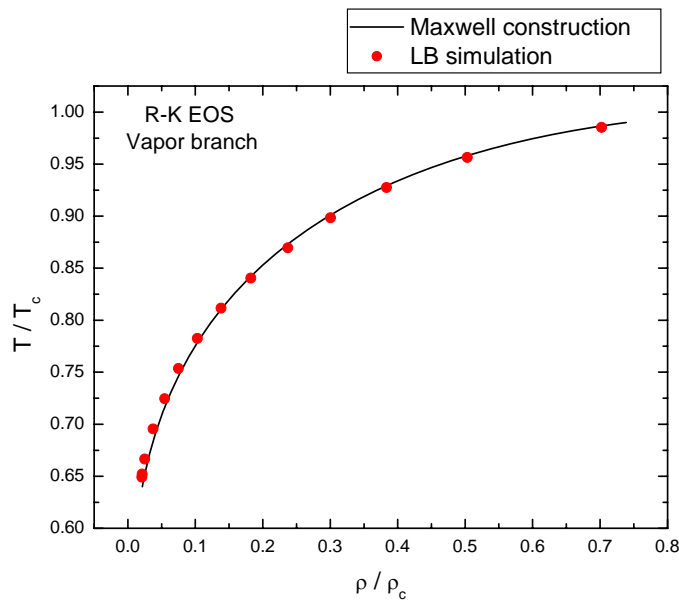


(b) Coexistence curve of the R-K EOS

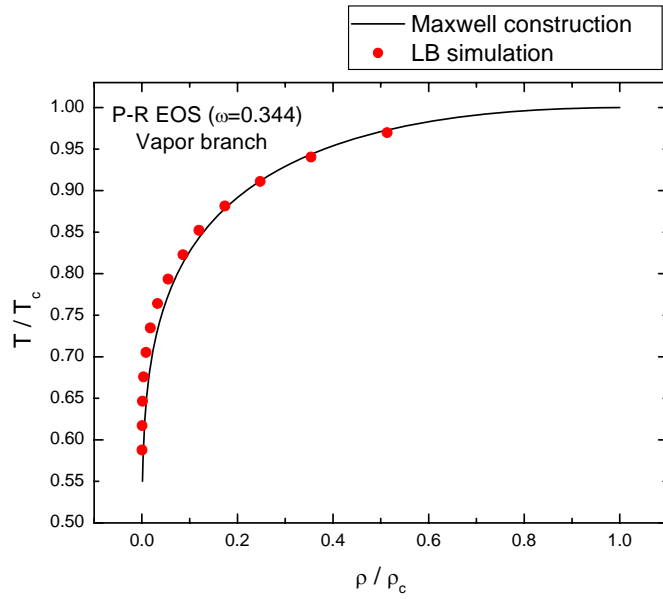


(c) Coexistence curve of the P-R EOS

Figure 4.7: Comparison of coexistence curves obtained from simulations with theoretical values for different EOS.



(a) Vapor branch of the coexistence curve of the R-K EOS



(b) Vapor branch of the coexistence curve of the P-R EOS

Figure 4.8: Comparison of the vapor branch of the coexistence curves obtained from simulations for R-K EOS and P-R EOS.

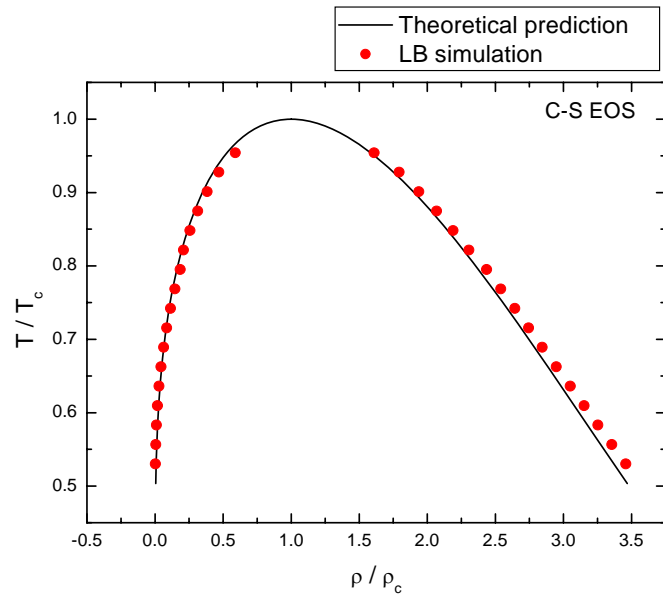


Figure 4.9: Comparison of coexistence curves obtained from simulations with theoretical values obtained by equating the chemical potentials for C-S EOS.

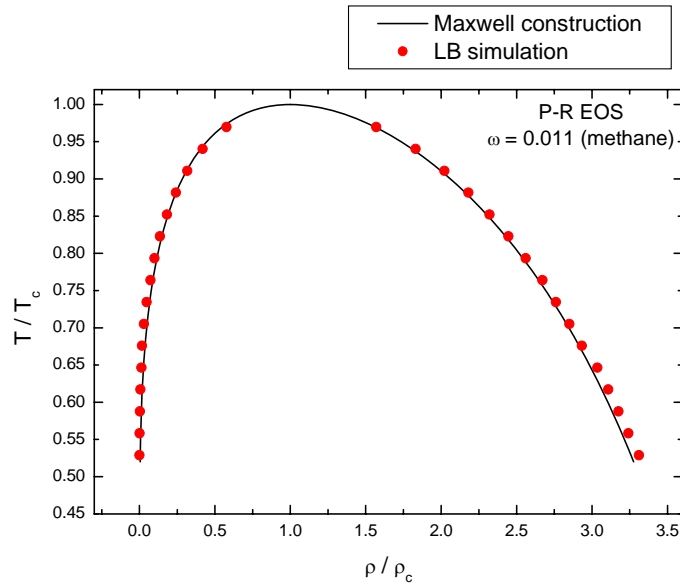
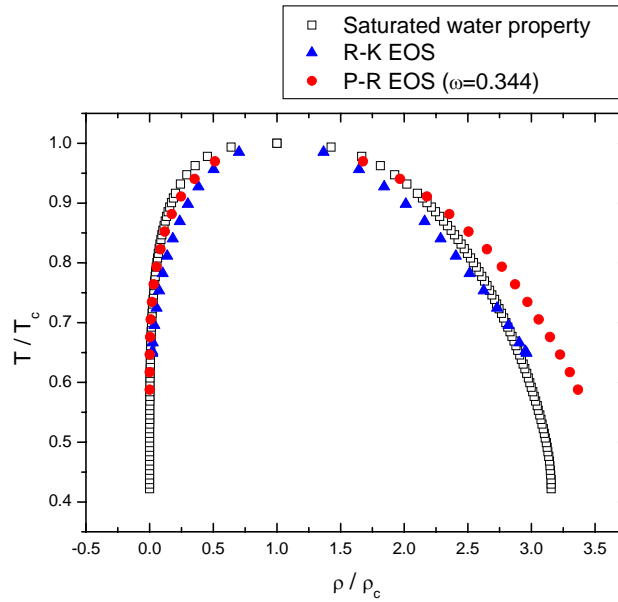


Figure 4.10: Comparison of coexistence curve obtained from simulations with theoretical values for P-R EOS with $\omega = 0.011$.

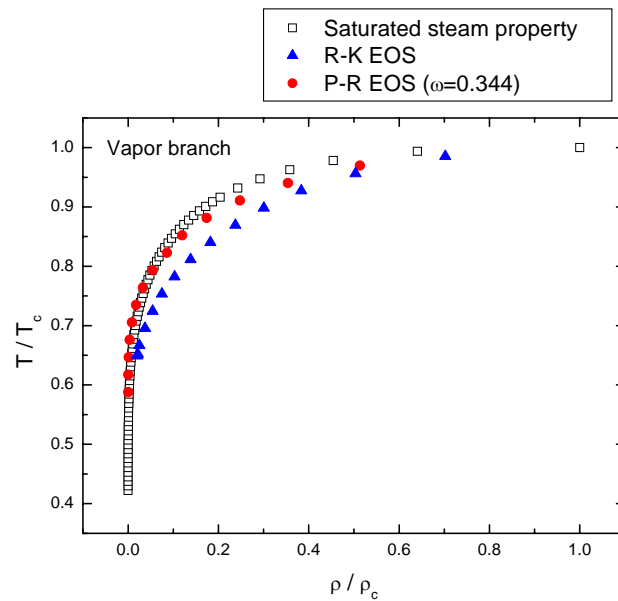
4.4.3 Comparison of equations of state and actual fluid properties

Finally, we compare our simulation results with some real fluid data. We chose the most commonly used fluid: water. The acentric factor for water is 0.344. Figure 4.11 gives the comparison of the saturated density obtained from simulations for the R-K EOS and P-R EOS with experimental data from the steam table. From this comparison with experimental data, we can see that for the liquid density, the R-K EOS gives better results, while for the vapor density, the P-R EOS gives better results. At T_{\min} , the relative error of the liquid density is 11.815% for the P-R EOS. However, we still generally consider the P-R EOS to be superior to the R-K EOS because the P-R EOS allows for a wider temperature range and can handle higher density ratios. Furthermore, unlike the P-R EOS, the R-K EOS is a two-parameter EOS. Therefore, no matter what fluid is being simulated, the R-K EOS gives the same coexistence curve for the reduced properties. The P-R EOS is a three-parameter EOS, and the third parameter (the acentric factor)

gives us more flexibility in simulating different fluids. For example, by setting $\omega = 0.011$, we are essentially using the properties of methane. The simulated coexistence curve for this value of the acentric factor is given in Figure 4.10, and fits well with the theoretical values.



(a) Vapor and liquid branch



(b) Vapor branch

Figure 4.11: Comparison of the saturated density of water obtained from simulations with experimental data from the steam table for different EOS.

4.5 DISCUSSION

It has been argued that a serious problem of the SC LBE model is that one cannot introduce a thermodynamically well-defined temperature. However, from our simulations, we can see that by properly choosing the EOS, one can introduce temperature explicitly (in the SC EOS, there is indeed no explicitly defined temperature), and also have a coexistence curve very close to the theoretical prediction, which is thermodynamically well defined.

We have demonstrated the applicability of the LBE method in simulating two-phase flow using a variety of EOS. While suitable for some applications, the vdW EOS generally does not give satisfactory results. However, the C-S EOS and P-R EOS, which are revisions of the vdW EOS for the hard sphere term and attraction term respectively, demonstrate much better performance in terms of spurious currents, temperature ranges and density ratios. Other revisions, like the R-K EOS and RKS EOS also give better simulation results. Therefore, we can say that as the selected EOS becomes more realistic, a better performance will be obtained from the LBE simulation.

For the coexistence curves, the simulation results of the vdW EOS significantly deviate from the theoretical values. The simulation results of the R-K EOS, P-R EOS and C-S EOS fit quite well with the theoretical values, however. Therefore, by properly choosing an EOS, we can both introduce temperature explicitly and develop a coexistence curve that is very close to the theoretical prediction.

Furthermore, by comparing the simulation results with experimental data for saturated water/steam, the R-K EOS gives better results for the water density and the P-R EOS gives better results for the steam density. There is a noticeable difference, particularly for the liquid leg, but this is due to the EOS itself, since the coexistence curve obtained from the simulation fits well

with theoretical values. Therefore, a translation from the simulation results might be needed in this case. For future research, an investigation of other more realistic EOS, such as those with corrections for both the attraction and hard sphere terms of the vdW EOS [104] is very promising (as well as computationally challenging), and can greatly enlarge the applicability of the LBE method in two-phase flow simulation.

5.0 THERMAL LBE MODEL

5.1 INTRODUCTION

Despite the progress made by LBE models in simulating multiphase and multicomponent flows, there is a crucial missing part: the lack of a satisfactory thermal model for multiphase flows. The entire multiphase LBE models mentioned in Chapter 3 are limited to regimes where the temperature dynamics are either negligible or their effects on the flow are unimportant. However, the thermal effects are ubiquitous and sometimes dominant in multiphase flow systems. For example, when phase transition occurs in the flow system, like in boiling and condensation processes, the evolution of the temperature field and flow field will be directly coupled with each other. One cannot solve one field without knowing the other. Therefore, it is very important to develop the thermal LBE (TLBE) multiphase model, which is capable of simulating the thermal effects simultaneously with the fluid dynamics. We will discuss this issue in this chapter.

For single-phase flow, there are several LB thermal models, which generally fall in two categories, namely: the multispeed approach [105, 106] and the passive-scalar approach [107]. The multispeed approach is a straightforward extension of LBE isothermal models. It implements energy conservation by adding additional speeds and by including the higher-velocity terms in the equilibrium distribution. Although theoretically possible, the multispeed approach suffers from severe numerical instability [108, 109, 110]. Meanwhile, the temperature

range it can handle is rather limited and usually the computation is more expensive because more PDFs need to be tracked.

In the passive scalar approach, the temperature field is passively advected by the fluid flow and can be simulated as an additional component of the fluid system. This means that in order to solve for the temperature field in the multiphase isothermal LBE framework, one only needs to solve an auxiliary LBE. Thus, the overall complexity of the scheme does not significantly increase. Additionally, unlike for the multispeed approach, the thermal diffusivity is independent of the viscosity in the passive scalar approach, which results in a changeable Prandtl number in simulations. Most importantly, the passive scalar approach does not explicitly implement energy conservation, and therefore has the same stability as the isothermal LBE models. We will derive our multiphase TLBE model based on the passive scalar approach.

5.2 SINGLE-PHASE TLBE MODEL

5.2.1 Numerical method

First we begin with the single-phase TLBE model using the passive scalar approach. In a thermal fluid system, if the viscous and compressive heating effects are negligible, the temperature field satisfies a much simpler passive-scalar equation:

$$\frac{\partial T}{\partial t} + \mathbf{u} \cdot \nabla T = \nabla \cdot (\alpha \nabla T) + \Psi \quad (5.1)$$

where \mathbf{u} is the whole fluid velocity; α is the thermal diffusivity; and Ψ is the source term. After solving the fluid dynamics part by using Eqs. (1.11) and (1.6), Eq. (5.1) can be solved in the LB framework by again using those equations, except that τ will be replaced by τ_T (the

dimensionless single relaxation time for temperature). The summation of the PDFs of temperature will therefore give the temperature value. Similarly, $\alpha = (\tau_T - \frac{1}{2})c_s^2\delta t$, and, thus, the Prandtl number will be

$$\text{Pr} = \frac{\nu}{\alpha} = \frac{2\tau - 1}{2\tau_T - 1} \quad (5.2)$$

By changing τ and/or τ_T , we can generate a different Prandtl number.

5.2.2 Boundary conditions

Two different thermal BCs were tested in our simulations. Here we explain them in the context of a D2Q9 model.

i) Isothermal wall: Suppose the temperature is fixed as T_b at the bottom wall. After streaming, f_2 , f_5 , and f_6 are unknowns. Assume these unknown PDFs equal their equilibrium distribution given by Eq. (1.6) with ρ replaced by some unknown temperature T' . Summing these three PDFs together, we have [111]:

$$f_2 + f_5 + f_6 = \frac{1}{6}T'(1 + 3u_y + 3u_y^2) \quad (5.3)$$

where u_y is the velocity normal to the wall. If we know T' , we will be able to solve for f_2 , f_5 , and f_6 . Meanwhile, we notice that for the isothermal wall, $\sum_{\alpha=0}^8 f = T_b$. Substituting Eq. (5.3) into

this, T' then can be calculated as follows:

$$T' = \frac{6}{1 + 3u_y + 3u_y^2} (T_b - f_0 - f_1 - f_3 - f_4 - f_7 - f_8) \quad (5.4)$$

Finally, f_2 , f_5 , and f_6 can be obtained by substituting T' into Eq. (1.6). This method can be easily extended to the 3-D case.

ii) Heat flux BC: After streaming, the temperature of the inner domain can be obtained. A second-order finite difference scheme is used to get the temperature on the wall [112], i.e., for

the bottom wall at $y = 0$, $\left. \frac{\partial T}{\partial y} \right|_{i,1} = \frac{4T_{i,2} - T_{i,3} - 3T_{i,1}}{2\Delta y}$. After finding the wall temperature, the

same procedure as described in the isothermal wall case is used to calculate the unknown PDFs.

5.2.3 Benchmark tests

Two simulation studies were conducted to validate our single phase TLBE model: Rayleigh-Bénard convection (RBC) and heat generation inside a square domain.

A good benchmark test for a thermal fluid system is (RBC), where a horizontal layer of viscous fluid is heated from the bottom and the top boundary is maintained at a lower temperature [113]. When the temperature difference between the bottom and top boundary exceeds some threshold, the static conduction becomes unstable. Any small perturbation will make the system become convective.

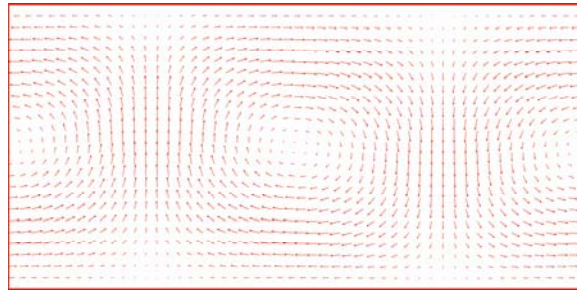
We simulate 2-D and 3-D RBC by using the D2Q9 and D3Q19 models, respectively. In the 2-D simulation, the temperatures at the bottom wall ($y = 0$) and top wall ($y = 1$) are kept at $T_B = 1$ and $T_T = 0$, respectively. So, $\Delta T = T_B - T_T = 1.0$. A lattice size of 101×50 is used in the simulation. The two non-dimensional terms used to describe the system are the Prandtl number and the Rayleigh number. The Prandtl number is defined in equation (5.2). The Rayleigh number is defined as

$$\text{Ra} = \frac{g\beta\Delta T(ny)^3}{\nu\alpha} \quad (5.5)$$

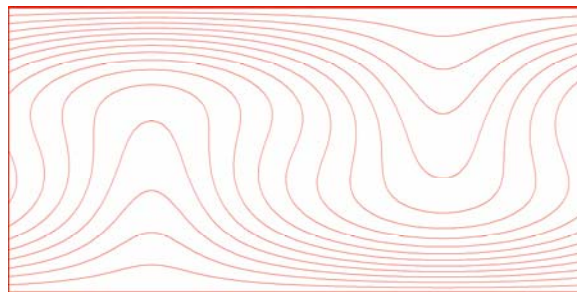
where g is the acceleration due to gravity, β is the thermal expansion coefficient, and ny is the lattice size in the y direction. The Boussinesq approximation is used, which assumes that the material properties are independent of temperature except in the body force term. For the gravitational term, the density is assumed to be a linear function of the temperature. Also, part of the gravity force is absorbed in the pressure term to eliminate the buoyancy force in the conduction state, which leads to the following expression of the external force

$$\rho\mathbf{G} = \rho\beta g(T - T_0)\mathbf{j} \quad (5.6)$$

where $T_0 = T_B - y\Delta T$. We calculated the RBC at different Ra and Pr numbers. Figure 5.1 plots the typical velocity vectors and isotherms at Ra = 5000 and Pr = 1.0.



(a) Velocity vectors



(b) Isotherms

Figure 5.1: Velocity vectors and isotherms at Ra = 5000, Pr = 1.0

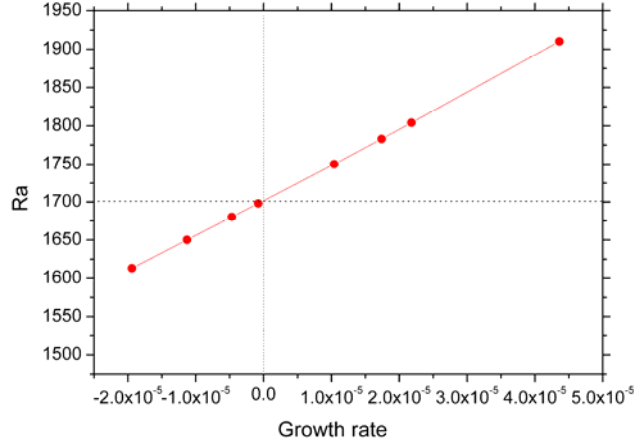


Figure 5.2: Growth rate of instability vs. Ra number

In order to evaluate the accuracy of the method, the onset of RBC is also tested. To determine this, the simulation is conducted at different Ra numbers around the critical Ra number Ra_c . After that, the growth rate (rate of increase of the maximum velocity in the y direction) is measured. The results are shown in Figure 5.2, in which the growth rates are plotted against the Ra number. The zero growth rate corresponds to the critical Ra number. Using a least-squares fit, the critical Ra number is found to be 1702.436, which agrees well with the theoretical value of 1707.762 obtained by linear stability theory. The relative error is 0.3119%.

Another useful test for code validation is a 2-D heat conduction problem with heat generation inside the domain. A square domain (length $L = 1.0$, height $H = 1.0$) with an adiabatic BC at the top and right walls, a uniform temperature $T_L = 2.0$ at the left wall, and a uniform temperature $T_B = 1.0$ at the bottom wall is calculated in a 50×50 mesh. Additionally, there is heat generation q''' inside the domain. The domain initially has a uniform temperature of 2.0.

To represent heat generation properly in the LB context, we compare the non-dimensional heat generation in a real problem and in the LBE method. These two values should, of course, be equal. This means that:

$$q^* = \frac{q^m L^2}{k T_0} = \frac{q_{Lu}^m L_{Lu}^2}{k_{Lu} T_{0,Lu}} = \frac{q_{Lu}^m L_{Lu}^2}{\alpha_{Lu} \rho_{Lu} c_{V,Lu} T_{0,Lu}} \quad (5.7)$$

where the subscript “ Lu ” denotes a lattice unit, T_0 is some reference temperature, and k is the thermal conductivity. In the LBM, we only specify the thermal diffusivity α . Hence ρ_{Lu} and $c_{V,Lu}$ are set to be unity. Then

$$q_{Lu}^m = \frac{q^* \alpha_{Lu} T_{0,Lu}}{L_{Lu}^2} \quad (5.8)$$

Similarly, the time step in the LBM can be related to the physical time through:

$$t^* = \frac{\alpha t}{L^2} = \frac{\alpha_{Lu} t_{Lu}}{L_{Lu}^2} \quad (5.9)$$

Figure 5.3 shows the isotherms at steady state obtained by the LBE method. Figure 5.4 shows the Nusselt number at the top wall (adiabatic wall) with respect to the time step in the LBE simulation, which is a very small value. This test shows that the heat flux BC and heat source term are properly incorporated in the LBE method. Furthermore, the heat source term can be related to the viscous and compressive heating terms, which will greatly extend the scope of the method.

For comparison, the finite difference (FD) method is also used to evaluate the same problem. Using the same grid resolution, the average relative error is $E \approx 8.4 \times 10^{-4}$, where E is defined by:

$$E = \frac{\sqrt{\sum_x \sum_y [T_{LBE}(x, y) - T_{FD}(x, y)]^2}}{\sqrt{\sum_x \sum_y T_{FD}^2(x, y)}} \quad (5.10)$$

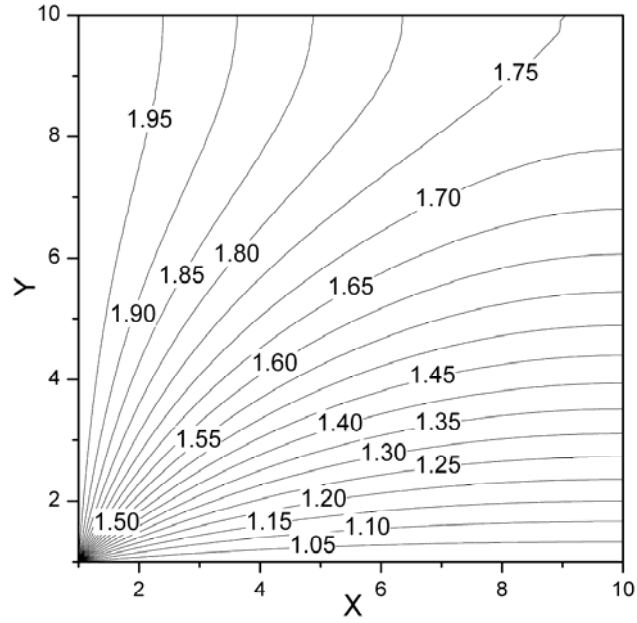


Figure 5.3: Isotherms at steady state obtained by the LBE method.

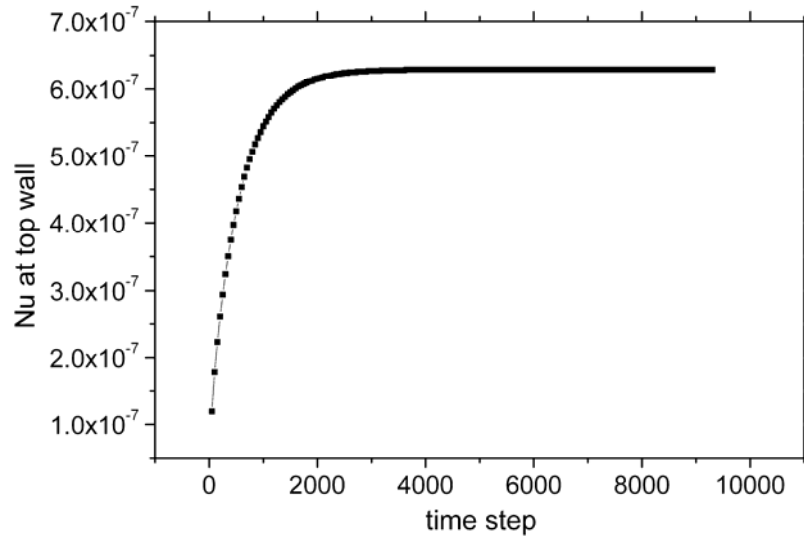


Figure 5.4: Nusselt number at the top wall with respect to the time step obtained by the LBE method.

5.3 MULTIPHASE TLBE MODEL

Combining the previous single component multi-phase LBE model and passive scalar TLBE model, the single component two-phase TLBE model is proposed. In this model, the fluid dynamics are simulated by an isothermal LBE with the interparticle potential incorporated. The temperature field is determined by an additional passive scalar equation and the coupling of these two parts is through a suitably defined body force term in the isothermal LBE.

Eqs. (1.6), (1.9) and (1.11) with Eqs. (3.3), (3.7) and (3.10) – (3.14) are used to simulate the flow field. Equation (5.1) is used to simulate the temperature field. The buoyancy term induced by the gravity and temperature difference can be expressed as:

$$\rho(\mathbf{x})\mathbf{G} = \rho(\mathbf{x})g\left(1 - \frac{\langle \rho \rangle}{\rho(\mathbf{x})}\right)\mathbf{k} - \beta\rho g(T - T^*)\mathbf{k} \quad (5.11)$$

where $\langle \rho \rangle$ is the average density of the mixture in the entire domain; g is the acceleration due to gravity; T^* is the reference temperature, which is usually equal to the temperature at the pure conduction state; and β is the thermal expansion coefficient, which we assume is equal for the two phases. However, β can also easily be specified to be different values for different phases. In Eq. (5.11), the first term on the RHS represents the buoyancy force due to the density difference. The second term on the RHS represents the buoyancy force due to the temperature difference.

Although conceptually very simple, this model can produce a non-ideal gas EOS and capture the temperature field at the same time. In comparison to other multi-phase TLBE models, it is easy to realize and more stable, because it doesn't require adding more particle speeds or tracking the energy evolution. The stability is determined by the fluid dynamics, and the

temperature field has no influence on it. Also, the energy source term Ψ reserves the space for adding viscous and compressive heating terms in the future.

An important point to note is that we have not considered phase transition and latent heat in the current model. In general, the phase transition phenomena are strongly related to the thermodynamics and their mechanics are very complicate. The phase transition rate is a function of thermodynamic properties such as temperature and pressure. In order to consider phase transition in the LB context, one needs to consider how to link the phase transition rate with these thermodynamic properties and how to incorporate latent heat into the scheme. Some pioneering work has been done by using simple approximations. For example, Kono and Ishizuka [114] specify a constant phase change rate in their model and relate it to the latent heat. Miller and Succi [115] studied anisotropic crystal growth from melt. They use a phase-field equation to simulate the phase transition and consider latent heat as an extra force term. It may be possible to adapt these treatments to our methodology.

5.4 SIMULATION RESULTS

5.4.1 Initial flow field and temperature setting

We simulated a thermal two-phase system in a rectangular channel under different conditions (different Reynolds number, different Rayleigh number, and different boundary conditions). Most of the simulations were conducted on a $50 \times 50 \times 50$ lattice size with a periodical boundary condition (BC) in the x direction, and wall boundary conditions (BCs) in the y and z directions for the fluid dynamics. Grid independency was checked for all of the different resolutions used in the paper by varying the lattice sizes.

A body force in the x direction is also included in the simulation:

$$\mathbf{F}_x = \rho(\mathbf{x})a\mathbf{i} \quad (5.12)$$

where a is the acceleration due to the body force. Defining the characteristic velocity U' (in lattice units) as $U' = \frac{\rho(\mathbf{x})a(nz)^2}{\mu} = \frac{a(nz)^2}{\nu}$, the Reynolds number will hence be:

$$\text{Re} = \frac{U'nz}{\nu} = \frac{a(nz)^3}{\nu^2} \quad (5.13)$$

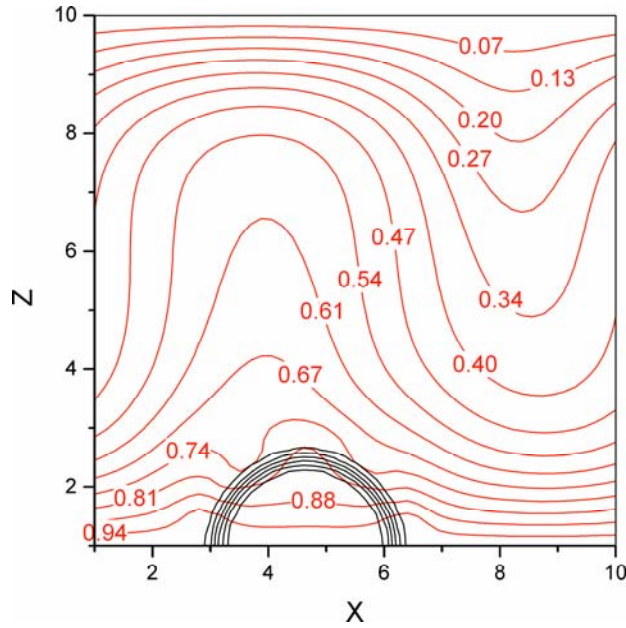
In the simulation, the bottom wall and top wall are kept at fixed temperatures of 1.0 and 0.0, respectively. The vertical walls are adiabatic. Therefore, the Rayleigh number has the same form as equation (5.5) except that in 3-D, ny should be replaced by nz .

Initially, a droplet is placed at the center of the domain with no force on it. After several hundred time steps, the droplet reaches equilibrium. This equilibrium process is needed; otherwise, the code fails to converge. Next the buoyancy force in the z direction and the body force in the x direction will be turned on, and the droplet will fall until it reaches the bottom wall. Due to different wettabilities at the wall, it can form different contact angles. If the relative difference of the maximum magnitude of the velocities at time step t and at $t-100$ is smaller than a given tolerance, steady state is considered to be reached (in this case, all other variables also have a small relative change). If steady state cannot be reached (in this case, usually the system will exhibit some periodical feature), the duration of the simulation (more than 20,000 time steps in lattice units) will produce statistical results.

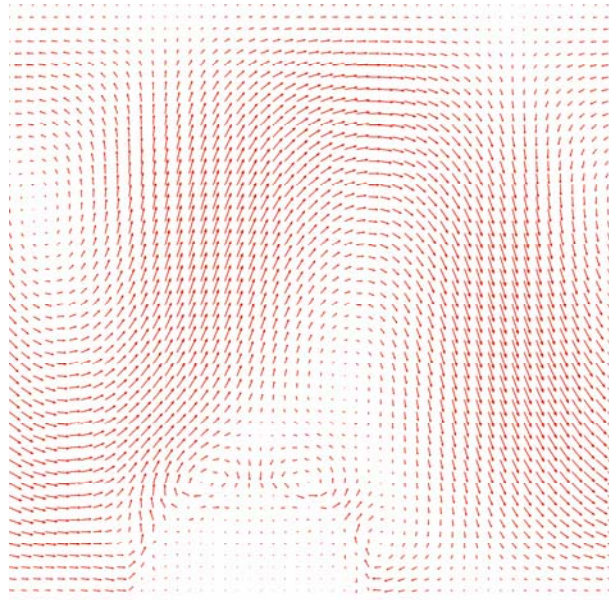
5.4.2 Multiphase thermal flow base case

First, we present our simulation results for two-phase flow at given Rayleigh numbers. Since the SC EOS produces the greatest unphysical variation of all the EOS presented in the previous

chapter, we will use this for all of our simulations (with $g_f = -0.35$) to show the extrema of the possible errors from spurious currents in this method. The initial droplet radius is 7.0. The Reynolds number is held at 100.



(a) Isotherms and density contours



(b) Velocity vectors

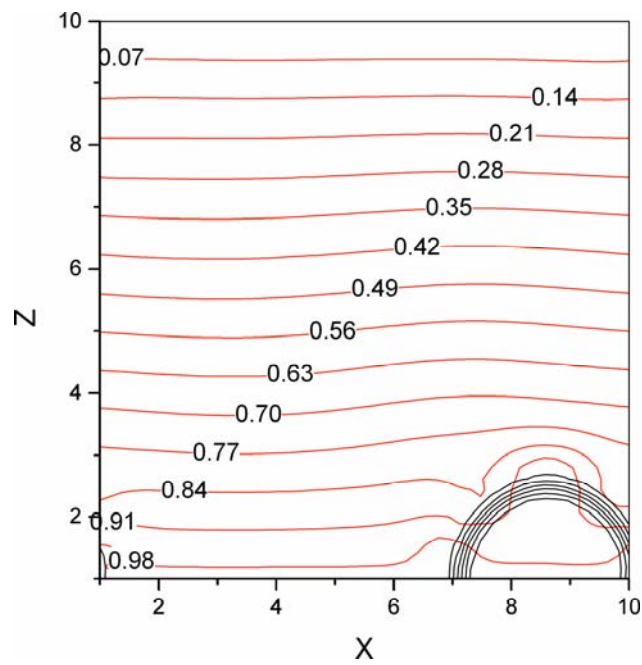
Figure 5.5: Isotherms, density contours and velocity vectors at $Ra = 10000$, $Re = 100$.

Figure 5.5 shows the isothermal contours, density contours and velocity vectors in the xz -plane at $y=25$ (the symmetric plane) for $Ra = 10,000$ and $Re = 100$. The isotherms form ascending and descending fluid sheets in the vapor phase. In the liquid phase, the isotherms are flattened. This is mainly because the buoyancy force due to the temperature difference is balanced by the buoyancy force due to the density difference in the liquid phase. In this example, the liquid and vapor phases in our model have the same properties except for densities. As discussed in Chapter 4, however, the code has the potential for specifying different properties for different phases and also specifying different EOS.

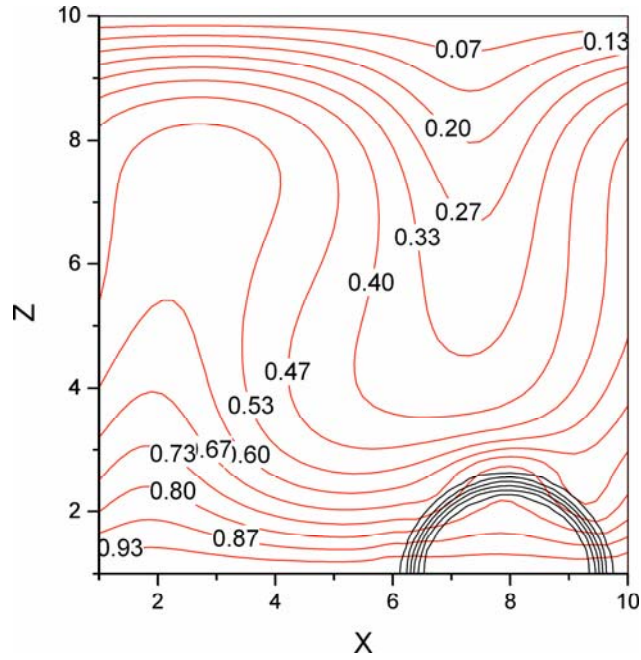
In our static bubble test, we observed the existence of spurious currents. The spurious currents have an influence on the temperature field and will affect local heat transfer results. This is verified because we are using the velocity of the flow as the advection velocity of the temperature. The fluctuation of the isotherms near the top interface of the droplet shows this influence. However, as for the large scale or overall heat transfer results, we can ignore this influence for two reasons. First, these spurious currents are mostly constrained to be in the interface region and will not extend to a distance far away from the interface. Second, for $|g_f| \leq 0.35$, compared with the main flow velocity, the magnitude of the spurious currents is relatively small and can be neglected. Also, as shown in Chapter 4, by changing the EOS, we can greatly reduce the spurious currents. The incorporation of these more realistic EOS into TLBE model will therefore produce more accurate temperature distributions, especially in the region near the interface.

5.4.3 Effect of varying Rayleigh number

Figure 5.6 shows the isotherms and density contours in the xz -plane at $y = 25$ for $Ra = 5,000$ and $15,000$. As the Rayleigh number increases, the temperature gradient near the wall becomes sharper: in the $Ra = 5,000$ case, the isotherms are almost straight lines and evenly distributed, while in the $Ra = 15,000$ case the isotherms are highly curved and much thicker near the wall. Also, as the Rayleigh number increases, the ascending and descending fluid sheets become narrower.



(a) $Ra = 5000$



(b) Ra = 15000

Figure 5.6: Isotherms and density contours at different Rayleigh numbers

5.4.4 Nusselt number variation

The Nusselt number of the bulk flow is defined as:

$$Nu = 1 + \frac{\langle u_z (T - T^*) \rangle N_z}{\alpha \Delta T} \quad (5.14)$$

where u_z is the velocity in the z direction; T^* is the reference temperature, here using the temperature at the pure conduction state; N_z is the lattice size in the z direction; and $\langle \cdot \rangle$ represents the average over the whole flow domain.

The Nusselt numbers of the bulk flow, at the top wall, and at the bottom wall as functions of the time step are shown in Figure 5.7, with Ra = 10,000 and Re = 100. Instead of approaching a constant value, all three values have small fluctuations throughout the simulation. The

fluctuation exhibits periodical features. The characteristic Nusselt number can be obtained by averaging the instantaneous values over time.

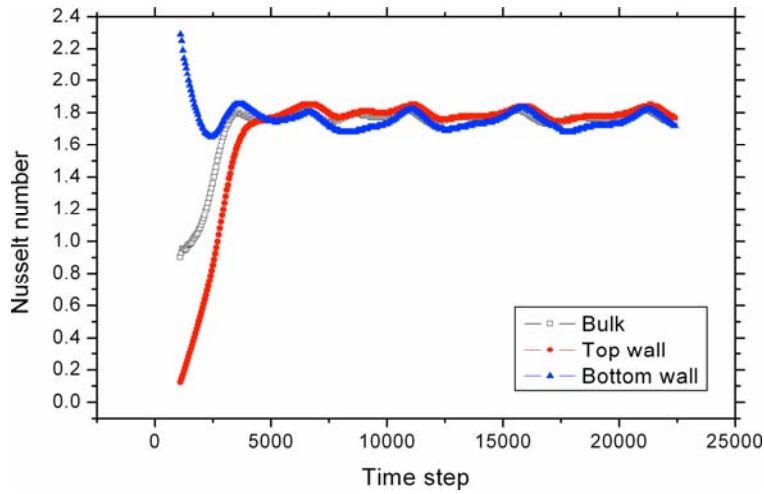


Figure 5.7: Nusselt numbers of the bulk flow, at the top wall, and at the bottom wall as functions of the time step ($Ra = 10000$, $Re = 100$).

Figure 5.8 shows the bulk Nusselt number changing with the time step at different Rayleigh numbers. The bulk Nusselt number increases as the Rayleigh number increases. The magnitude of the fluctuations also increases with increasing Rayleigh number.

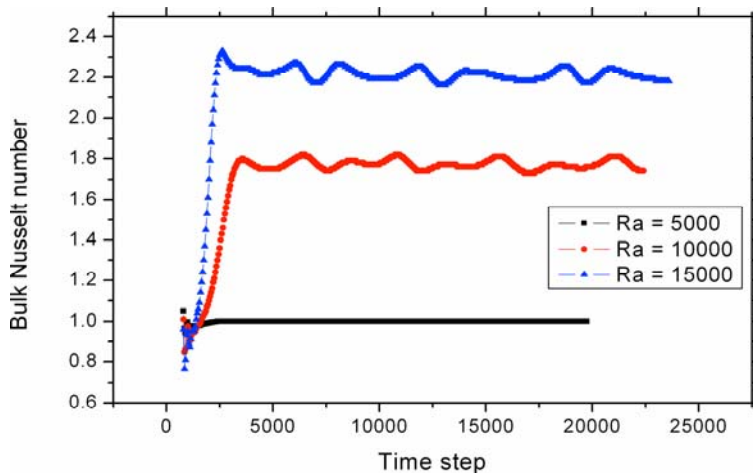


Figure 5.8: The bulk Nusselt number changing with the time step at different Rayleigh numbers.

The two-phase flow system under different Reynolds numbers is also simulated. The Rayleigh number is fixed at 10,000 and the Reynolds number takes the values 20, 100 and 500, respectively. Figure 5.9 shows the bulk Nusselt number changing with the time step at different Reynolds numbers. For $Re = 20$, the bulk Nusselt number is 1.808, which is slightly higher than that of $Re = 100$ (1.771), and the fluctuation is much smaller (almost a constant value). For $Re = 500$, the bulk Nusselt number (1.493) as well as the Nusselt number at the top and bottom walls is smaller than the $Re = 100$ case.

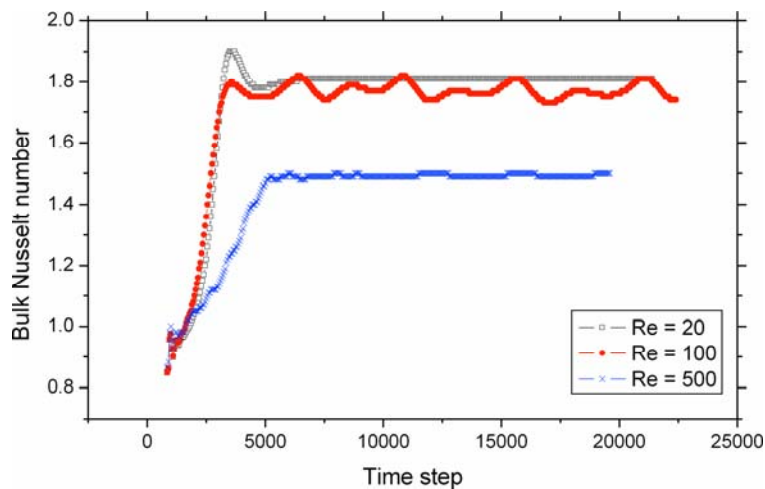
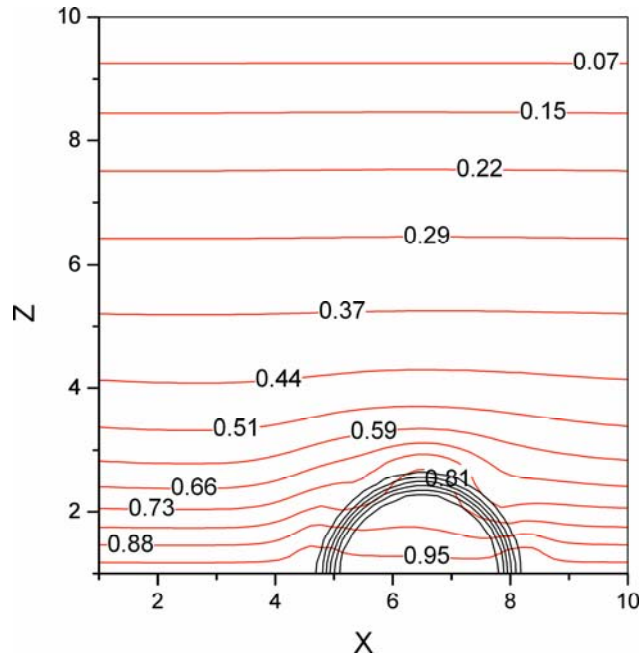


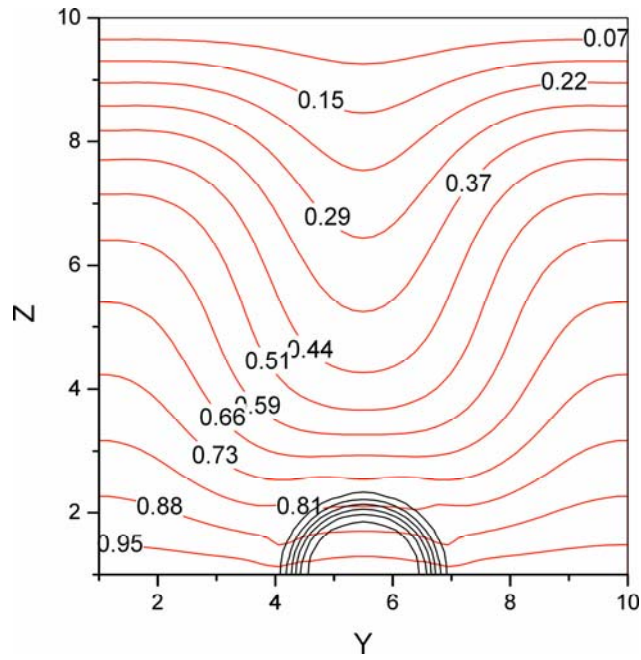
Figure 5.9: The bulk Nusselt number changing with time step at different Reynolds numbers.

These results seem counterintuitive. We believe the main reason is that the larger velocity in the x -direction suppresses the convection in the z -direction. In this problem, the temperature difference between the upper wall and lower wall is the main driving force for the heat transfer. Therefore, better convection in the z -direction will result in a higher Nusselt number. However, as the Reynolds number increases, the convection in the z -direction decreases, which can be seen from the isotherms of the xz -plane ($y = 25$) in Figure 5.10 ($Re = 500$ case), where the isotherms are almost straight lines in the x -direction. Also shown in Figure 5.10 are the isotherms in the yz -

plane ($x = 25$), which form some ascending and descending fluid sheets. Compared with Figure 5.5 (a) ($Re = 100$ case), these fluid sheets are wider and flatter.



(a) xz -plane ($y = 25$)



(b) yz -plane ($x = 25$)

Figure 5.10: Isotherms and density contours at $Ra = 10000$, $Re = 500$.

5.4.5 Effect of fluid-solid interaction strength

The influence of the fluid-solid interaction on the system is also investigated. Different g_w values (0.06 and -0.03) are used, which represent a typical non-wetting and wetting fluid. The contact angles for these two cases are 120.6° and 71.3° , respectively. The Reynolds number and Rayleigh number are fixed at 100 and 10,000. Table 5.1 lists the Nusselt numbers of the bulk flow, at the top wall, and at the bottom wall under different g_w values. Because of the fluctuation, the Nusselt number is averaged over the time steps. Compared to the no fluid-solid interaction case, the wetting case ($g_w = -0.03$) has a higher Nusselt number at the top wall, a lower Nusselt number at the bottom wall, and the bulk Nusselt number is increased. On the other hand, the non-wetting case ($g_w = 0.06$) has a lower Nusselt number at the top wall, a higher Nusselt number at the bottom wall, and the bulk Nusselt number is decreased.

An explanation for this phenomenon is that as the g_w value increases, the contact area between the droplet and the wall decreases, and the height of the droplet increases. This will increase the convection at the bottom wall since more area is exposed to the convection of the vapor phase. However, the bulk Nusselt number is decreased because the droplet extends deeper to the center and hampers the convection in that region.

Table 5.1: Nusselt numbers at different g_w values

$g_w \backslash$ Nu	Bulk	Top wall	Bottom wall
-0.03	1.852	1.918	1.698
0	1.771	1.797	1.741
0.06	1.733	1.722	1.954

5.5 DISCUSSION

In this chapter, we have proposed a thermal two-phase LBE model. In this model, the fluid dynamics is simulated by an isothermal single component multiphase LBE, and the temperature field is determined by an additional passive-scalar equation. The coupling of these two parts is through a suitably defined body force term in the isothermal LBE. The applicability of our model is demonstrated through numerical simulations. This new model can simulate a thermal two-phase flow system with a non-ideal gas EOS. Because the coupling is external, the new model has the same stability as the isothermal LBE model. Furthermore, it is simple and easy to code. Our studies show that different EOS, variable wettability, gravity and buoyancy effects, and relatively high Rayleigh numbers can be readily simulated by the new model. Also, the new model has the ability to handle complex BCs. For the future, further research is needed in properly incorporating a means to describe phase transition.

6.0 CONCLUSIONS AND FUTURE WORK

6.1 MAJOR ACCOMPLISHMENTS

In this dissertation, we have made several contributions to the study of two-phase flow using the LBE method. The following is a summary of our major accomplishments.

1. Development of a new TLBE two-phase model

We have successfully developed a new TLBE two-phase model for a single component system. In our new model, the fluid dynamics is simulated by an isothermal single component two-phase LBE (the SC model), and the temperature field is determined by an additional passive-scalar equation. The coupling of these two parts is through a suitably defined body force term in the isothermal LBE. Because the coupling is external, the new model has the same stability as the isothermal LBE model. Given a proper fluid-fluid interaction, this new model can simulate a thermal two-phase flow system with a non-ideal gas EOS. Furthermore, since the passive-scalar equation can also be solved in the framework of the LB method, the new model is simple and easy to code. The applicability of our model is demonstrated through numerical simulations. Our studies show that different EOS, variable wettability, gravity and buoyancy effects, as well as relatively high Rayleigh numbers can be readily simulated by the new model.

2. Incorporation of different EOS into the two-phase LBE model

We have demonstrated the applicability of using different EOS to simulate two-phase flow by the LBE method. We have showed that while suitable for some applications, the vdW EOS generally does not give satisfactory results, e.g. the coexistence curves obtained from the simulation using the vdW EOS significantly deviate from the theoretical values. However, the C-S EOS and P-R EOS, which are revisions of the vdW EOS for the hard sphere term and attraction term respectively, demonstrate much better performance in terms of spurious currents, temperature ranges and density ratios. Other revisions, like the R-K EOS and RKS EOS also give better simulation results. Furthermore, the simulation results of the R-K EOS, P-R EOS and C-S EOS fit quite well with the theoretical values, which means by properly choosing an EOS, we can both introduce temperature explicitly and develop a coexistence curve very close to the theoretical prediction. Therefore, we can say that as the selected EOS becomes more realistic, a better performance will be obtained from the LBE simulation. By comparing the simulation results with experimental data for saturated water/steam, the R-K EOS gives better results for the water density and the P-R EOS gives better results for the steam density. There are discrepancies, particularly for the liquid leg, but this is due to the EOS itself, since the coexistence curve obtained from the simulation fits well with theoretical values. Therefore, a translation from the simulation results might be needed in this case.

3. Addition of a flexible surface tension

It is argued that one limitation of the SC LBE model is that the surface tension coefficient of this model is coupled to the EOS and there is no freedom to vary it. In order to achieve a flexible surface tension, we proposed an additional force term $\mathbf{F}_s = \kappa\psi(\rho)\nabla\nabla^2\psi(\rho)$, which accounts for

the contribution of the surface tension, to be incorporated into the fluid-fluid interaction force. We then measured the surface tension both statically and dynamically. It has been shown that by adopting this additional force term, we can increase the surface tension about 78.68% and decrease it about 46.03% from the SC LBE base case for the simulated case.

4. Development of a new mass conserving boundary condition for the LBE method

We proposed a second-order accurate mass conserving boundary condition for the LBE method. Several benchmark test problems involving steady and unsteady flows were used to validate the accuracy and examine the robustness of the proposed BC. Compared with the FH and MLS BCs, our new BC has the following advantages: (1) The mass leakage is smaller than other schemes, and it will not result in the constant mass leakage seen in other BCs in some special cases. (2) It has much better stability than any other BC used in the simulations. Both the unstable region and the achievable minimum τ value are much smaller compared with other schemes. (3) In the normal region of Δ and τ , i.e. the stable region for all BCs, it gives second order accuracy and comparable or better results than other schemes. (4) It is not sensitive to the interpolation (weighting) factor and choice of \mathbf{u}_{bf} .

6.2 FUTURE WORK

Several possible future tasks are listed below. We have conducted preliminary research in some of these areas.

1. Multicomponent multiphase LBE model

Originally, the SC model was proposed for multiphase and multicomponent systems. In their multicomponent approach, the different components were included in the model by introducing different sets of PDFs, with each set of PDFs corresponding to one component. Accordingly, the fluid-fluid interaction force was also expanded to include interactions between different components. For the immiscible components, the attractive forces between particles of the same component (g_f^{11} and g_f^{22}) and repulsive forces between different components (g_f^{12}) were introduced. Using this approach, we have conducted some research on a two-phase two-component flow system. We found that the biggest problem for this approach is that the density ratio cannot be high [116]. The highest density ratio we can achieve is only about 2.0. If the density ratio is higher than that, the simulation will fail. Before reaching the blowup point, the densities approach infinity, which is called a mass collapse. However, in common gas-liquid bubbly flows, like an air-water system, the density ratio can be higher than 1000. In order to simulate such systems, we think one possible way of achieving a high density ratio is to specify a more realistic EOS for at least one component (particularly in the liquid phase) instead of using the SC EOS, as discussed in Chapter 4. The EOS of the other component (or the gas phase) can be described by the ideal gas law, SC EOS or other more realistic EOS, depending on the situation. Then the high density ratio is mainly guaranteed by the EOS of the liquid phase. The fluid-fluid interaction force g_f^{12} between the liquid and gas phases will therefore be used to separate the two phases and not to achieve a high density ratio, which will benefit the stability of the scheme, since a large g_f^{12} always results in instability in the simulation.

2. Mesh refinement

In order to increase efficiency while maintaining accuracy in numerical simulations, high resolution is always preferred in the high gradient regions, like the near wall region, and coarse resolution can be used in other regions. In N-S solvers, this can be realized by using grid-stretching techniques. However, as discussed before, the standard LBE uses a uniform lattice, $\delta x = \delta y = 1$, which poses difficulty in fulfilling the resolution requirement. To overcome this difficulty, different approaches have been proposed, e.g. the LBE method using a non-uniform grid [117, 118], the interpolation scheme, etc. In order to preserve the inherent advantage of LBE, however, it is preferable to use the uniform grid. For single-phase flow, Filippova and Hänel [52] proposed a local refinement method using a uniform grid with a higher resolution in the refined region. Patches of fine grids are used in certain regions, for example, near the solid boundary. At the interface, the post-collision PDFs of the coarse grid were rescaled to satisfy the conservation of mass and momentum and continuity of stresses across the interface and then sent to the fine grid. After proceeding n “streaming-collision” steps on the fine grid, where n is the refinement ratio, the post-collision PDFs of the fine grid were sent back to the coarse grid. Interpolations in space and time were needed during these processes. Yu [45] later revised this method by using interlaced coarse and fine grid. We have introduced Yu’s method to both our TLBE model and multiphase LBE model. The expansion to the single component TLBE model was straightforward and produced some promising results. However, the extension to the multiphase LBE model was unsuccessful, due to the difficulty in correctly incorporating the fluid-fluid interaction force in the refined region. It seems that the scheme is very sensitive to the interaction force, and even higher order interpolation of this force will result in mass leakage and eventually make the scheme unstable. Therefore, further research is needed in this area.

3. Viscous and compressive heating and phase transition phenomena

As discussed before, in the passive scalar approach, viscous and compressive heating effects were neglected. Efforts should be made to develop a more accurate thermal model, which can take viscous and compressive heating effects into account. One possibility is using the energy source term Ψ to represent viscous and compressive heating terms, as mentioned in Chapter 5. Generally, phase transition phenomena are strongly related to the thermodynamics and are very complicated with respect to the flow mechanics. The phase transition rate is a function of properties such as temperature and pressure. As a simplified means of incorporating these phenomena, one can specify a constant phase transition rate and include it in the energy source term. For a higher-accuracy model of transition regimes, however, the mechanics of the phase transition must be better quantified, both through experimental and computational means.

4. Parallel computation of the multi-phase TLBE model

One of advantage of the LBE method is that it is very suitable for parallel computation. The collision step is exactly local and the streaming step is almost local, and only needs information from the neighboring sites. In the SC multi-phase model, although the fluid-fluid interaction force theoretically requires information from all other sites, by restraining this force inside the next-nearest neighbors, as we discussed in Chapter 3, the overall operation is still suitable for parallel computation. Parallel computation has been applied to the SC two-phase flow model by several researchers [81, 82]. In our two-phase TLBE model, the addition of the temperature field will also not affect the applicability of parallel computation, since the temperature field itself is obtained from local variables. Therefore, parallel computation is also suitable for our two-phase

TLBE model and a great reduction in computational time is expected by implementing parallelization.

5. Surface tension and its effects.

Although we have proposed a method of varying surface tension in the SC LBE model, the influence of surface tension on the flow dynamics has not been thoroughly investigated yet. In order to incorporate even greater flexibility in varying and modeling surface tension, other computational techniques should also be explored.

6.3 APPLICATIONS OF THE MODEL

In this work, we proposed a new TLBE two-phase model for a single component system. Given a proper fluid-fluid interaction, the new model can be used to calculate fluid dynamics as well as heat transfer effects for a single component two-phase (vapor/liquid) flow system. Since previously the LBE method was used only for isothermal simulations, our new model therefore greatly enhances the applicability of the LBE method. Also demonstrated in this work is that by using proper EOS, a density ratio between the two phases as high as 1000 can be readily modeled, which is enough for most engineering applications. Furthermore, much smaller spurious currents and a more accurate coexistence curve were also obtained as a result of using a proper EOS, which guarantees more accurate simulation results.

In an effort to cure the formerly “fixed” surface tension in the SC LBE model, we proposed a method of varying surface tension in the SC LBE model. In our method the contribution of the surface tension was incorporated into the fluid-fluid interaction as an additional force term and

variable surface tension was obtained by varying this force term. The variable surface tension is very useful and sometimes essential for many applications, such as capillary flow [94], effects of a surfactant [119], and flow under microgravity [120].

We proposed a new mass conserving boundary treatment, which will not result in constant mass leakage when compressibility was encountered in the simulation and more importantly it has a much better stability than other boundary treatments and easy to implement at the same time. Therefore, it can be used in simulations with complex boundaries, such as flow in porous media, particle suspension flow, and flow in vascular structures [121].

Since dispersed two-phase gas-liquid flows, like air-water flow, are ubiquitous in the engineering processes, such as flow in chemical reactors, therefore, in the future, a multiphase, multicomponent model capable of simulating density ratio reaching 1000 is needed, which will greatly enrich the capability of the LBE method. Meanwhile, our new TLBE two-phase model is need to be modified to satisfy the simulation requirement of more complex systems, such as flow with phase change (boiling, condensation, etc), flow with compressive heating, and flow with a chemical reaction [122, 123]. All these modifications put challenges on the model not only theoretically but also computationally, since these kinds of simulations are highly demanding in computational resources. In an effort to lower computation cost, further research in the parallel computation of LBE method is needed [124]. Development of parallel computation will also pave the way for the LBE method's applicability in other areas, where traditional CFD methods are computationally very expensive, such as flow in porous media [81], turbulent flow [125], and particle suspension flow [126].

APPENDIX A

FROM THE LBE TO THE N-S EQUATIONS

In the section 1.4, we showed how to derive the LBE model from the continuum Boltzmann equation with the BGK approximation. In this Appendix, we will show how to recover the N-S equations from the LBE. Our starting point is Eq. (1.11)--the LBGK model with SRT. Performing a Taylor series expansion in time and space with small parameters $\delta x = \delta t$ to the second order, we obtain:

$$\delta t \frac{\partial f_\alpha}{\partial t} + \delta t e_{\alpha k} \frac{\partial f_\alpha}{\partial x_k} + \frac{(\delta t)^2}{2} \left[\frac{\partial^2 f_\alpha}{\partial t^2} + 2e_{\alpha k} \frac{\partial^2 f_\alpha}{\partial t \partial x_k} + e_{\alpha k} e_{\alpha n} \frac{\partial^2 f_\alpha}{\partial x_k \partial x_n} \right] + \frac{1}{\tau} (f_\alpha - f_\alpha^{(eq)}) = 0 \quad (\text{A.1})$$

In order to derive the N-S equations from LBE, the Chapman-Enskog expansion [6], which in essence is a standard multi-scale expansion, is used as follows:

$$\frac{\partial}{\partial t} = \varepsilon \frac{\partial}{\partial t_1} + \varepsilon^2 \frac{\partial}{\partial t_2} \quad (\text{A.2a})$$

$$\frac{\partial}{\partial \mathbf{x}} = \varepsilon \frac{\partial}{\partial \mathbf{x}_1} \quad (\text{A.2b})$$

where ε is a small parameter, $\varepsilon \ll 1$. Eq. (A.2a) means that the convection time scale t_1 is much smaller than the diffusion time scale t_2 (low-frequencies assumption). And the PDF f_α can be expanded similarly as:

$$f_\alpha = f_\alpha^{(0)} + \varepsilon f_\alpha^{(1)} + \varepsilon^2 f_\alpha^{(2)} + O(\varepsilon^3) \quad (\text{A.3})$$

Inserting Eqs. (A.2) and (A.3) into Eq. (A.1), we obtain:

$$\begin{aligned} & \varepsilon^2 \left\{ \delta t \left[\frac{\partial f_\alpha^{(1)}}{\partial t_1} + \frac{\partial f_\alpha^{(0)}}{\partial t_2} + e_{ak} \frac{\partial f_\alpha^{(0)}}{\partial x_{1k}} \right] + \frac{(\delta t)^2}{2} \left[\frac{\partial^2 f_\alpha^{(0)}}{\partial t_1^2} + 2e_{ak} \frac{\partial^2 f_\alpha^{(0)}}{\partial t_1 \partial x_{1k}} + e_{ak} e_{cn} \frac{\partial^2 f_\alpha^{(0)}}{\partial x_{1k} \partial x_{1n}} \right] + \frac{1}{\tau} f_\alpha^{(2)} \right\} \\ & + \varepsilon \left[\delta t \frac{\partial f_\alpha^{(0)}}{\partial t_1} + \delta t e_{ak} \frac{\partial f_\alpha^{(0)}}{\partial x_{1k}} + \frac{1}{\tau} f_\alpha^{(1)} \right] = -\frac{1}{\tau} [f_\alpha^{(0)} - f_\alpha^{(eq)}] \end{aligned} \quad (\text{A.4})$$

Collecting the terms in the ascending order of ε :

$$O(\varepsilon^0): \quad f_\alpha^{(0)} = f_\alpha^{(eq)} \quad (\text{A.5})$$

$$O(\varepsilon^1): \quad f_\alpha^{(1)} = -\tau \delta t \left[\frac{\partial f_\alpha^{(0)}}{\partial t_1} + e_{ak} \frac{\partial f_\alpha^{(0)}}{\partial x_{1k}} \right] \quad (\text{A.6})$$

$$O(\varepsilon^2): f_\alpha^{(2)} = -\tau \delta t \left[\frac{\partial f_\alpha^{(1)}}{\partial t_1} + \frac{\partial f_\alpha^{(0)}}{\partial t_2} + e_{ak} \frac{\partial f_\alpha^{(0)}}{\partial x_{1k}} \right] - \tau \frac{(\delta t)^2}{2} \left[\frac{\partial^2 f_\alpha^{(0)}}{\partial t_1^2} + 2e_{ak} \frac{\partial^2 f_\alpha^{(0)}}{\partial t_1 \partial x_{1k}} + e_{ak} e_{cn} \frac{\partial^2 f_\alpha^{(0)}}{\partial x_{1k} \partial x_{1n}} \right] \quad (\text{A.7})$$

Using Eq. (A.6) and performing some algebra, Eq. (A.7) can be simplified to be:

$$O(\varepsilon^2): \quad f_\alpha^{(2)} = -\tau \delta t \frac{\partial f_\alpha^{(0)}}{\partial t_2} + \left(\frac{1}{2} - \tau \right) \delta t \left[\frac{\partial f_\alpha^{(1)}}{\partial t_1} + e_{ak} \frac{\partial f_\alpha^{(1)}}{\partial x_{1k}} \right] \quad (\text{A.8})$$

Eq. (A.5) means that the PDF f_α is not far from the equilibrium state. We can re-write Eq. (A.3)

as follows:

$$f_\alpha = f_\alpha^{(eq)} + \varepsilon f_\alpha^{(1)} + \varepsilon^2 f_\alpha^{(2)} + O(\varepsilon^3) \quad (\text{A.9})$$

The equilibrium distribution function satisfies the following constraints:

$$\rho = \sum_\alpha f_\alpha^{(eq)} \quad \rho \mathbf{u} = \sum_\alpha \mathbf{e}_\alpha f_\alpha^{(eq)} \quad (\text{A.10})$$

which lead to the following constrains:

$$\sum_\alpha f_\alpha^{(k)} = 0 \quad \sum_\alpha \mathbf{e}_\alpha f_\alpha^{(k)} = 0 \quad (k = 1, 2, \dots) \quad (\text{A.11})$$

Summing over all α for both Eq. (A.6) and Eq. (A.8), multiplying by e_{cn} and summing over all α for both Eq. (A.6) and Eq. (A.8), and using the constraints given by Eq. (A.10–11), we can obtain the following macroscopic equations:

$$O(\varepsilon^1): \quad \frac{\partial \rho}{\partial t_1} + \frac{\partial \rho u_k}{\partial x_{1k}} = 0 \quad (\text{A.12})$$

$$O(\varepsilon^1): \quad \frac{\partial \rho u_n}{\partial t_1} + \frac{\partial}{\partial x_{1k}} \sum_{\alpha} e_{cn} e_{ck} \frac{\partial f_{\alpha}^{(eq)}}{\partial x_{1k}} = 0 \quad (\text{A.13})$$

$$O(\varepsilon^2): \quad \frac{\partial \rho}{\partial t_2} = 0 \quad (\text{A.14})$$

$$O(\varepsilon^2): \quad \frac{\partial \rho u_n}{\partial t_2} + \left(1 - \frac{1}{2\tau}\right) \frac{\partial}{\partial x_{1k}} \sum_{\alpha} e_{cn} e_{ck} \frac{\partial f_{\alpha}^{(1)}}{\partial x_{1k}} = 0 \quad (\text{A.15})$$

Combining Eq. (A.12) and (A.14), the continuity equation is recovered to the second order of ε :

$$\frac{\partial \rho}{\partial t} + \frac{\partial \rho u_k}{\partial x_k} = 0 \quad (\text{A.16})$$

Combining Eq. (A.13) and (A.15), the momentum equation is recovered to the second order of ε :

$$\frac{\partial \rho u_n}{\partial t} + \frac{\partial}{\partial x_{1k}} \sum_{\alpha} e_{cn} e_{ck} \frac{\partial f_{\alpha}^{(eq)}}{\partial x_{1k}} + \left(1 - \frac{1}{2\tau}\right) \frac{\partial}{\partial x_{1k}} \sum_{\alpha} e_{cn} e_{ck} \frac{\partial f_{\alpha}^{(1)}}{\partial x_{1k}} = 0 \quad (\text{A.17})$$

Substituting Eq. (A.16) into Eq. (A.17), the momentum equations becomes:

$$\frac{\partial \rho u_n}{\partial t} + \frac{\partial}{\partial x_{1k}} \sum_{\alpha} e_{cn} e_{ck} \frac{\partial f_{\alpha}^{(eq)}}{\partial x_{1k}} + \left(\tau - \frac{1}{2}\right) \sum_{\alpha} \left[e_{cn} e_{ck} \frac{\partial^2 f_{\alpha}^{(eq)}}{\partial t_1 \partial x_{1k}} + e_{cn} e_{ck} e_{cm} \frac{\partial^2 f_{\alpha}^{(eq)}}{\partial x_{1k} \partial x_{1m}} \right] = 0 \quad (\text{A.18})$$

From Eq. (A.17), we can identify that the momentum flux tensor is:

$$\Pi_{\alpha\beta} = \Pi_{\alpha\beta}^{(0)} + \Pi_{\alpha\beta}^{(1)} = \sum_i e_{i\alpha} e_{i\beta} \left[f_i^{(eq)} + \left(1 - \frac{1}{2\tau}\right) f_i^{(1)} \right] \quad (\text{A.19})$$

with the zero order momentum tensor and first order momentum tensor given by the following equations:

$$\Pi_{\alpha\beta}^{(0)} = \sum_i e_{i\alpha} e_{i\beta} f_i^{(eq)} \quad \Pi_{\alpha\beta}^{(1)} = \sum_i e_{i\alpha} e_{i\beta} \left(1 - \frac{1}{2\tau}\right) f_i^{(1)} \quad (\text{A.20})$$

To specify the detailed form of $\Pi_{\alpha\beta}$, the lattice structure and corresponding equilibrium distributions have to be specified. The D2Q9 lattice is considered here. Derivation for other lattice structures can be obtained using similar fashion. For the D2Q9 model, the following identities are observed:

$$\sum_{\alpha} w_{\alpha} e_{\alpha m} e_{\alpha n} e_{\alpha k} e_{\alpha j} = \frac{c^4}{9} (\delta_{mn} \delta_{kj} + \delta_{mk} \delta_{nj} + \delta_{mj} \delta_{nk}) \quad (\text{A.21})$$

$$\frac{\partial}{\partial x_{1m}} \frac{\partial}{\partial x_{1k}} \sum_{\alpha} w_{\alpha} e_{\alpha m} e_{\alpha n} e_{\alpha k} e_{\alpha j} \rho u_j = \frac{c^4}{9} \left[\frac{\partial^2}{\partial x_{1m} \partial x_{1m}} (\rho u_n) + 2 \frac{\partial^2}{\partial x_{1m} \partial x_{1n}} \rho u_n \right] \quad (\text{A.22})$$

Substituting Eq. (1.6) into Eq. (A.18) and using identity (A.22), we find:

$$\sum_{\alpha} \left[e_{\alpha n} e_{\alpha k} \frac{\partial^2 f_{\alpha}^{(eq)}}{\partial t_1 \partial x_{1k}} + e_{\alpha n} e_{\alpha k} e_{\alpha m} \frac{\partial^2 f_{\alpha}^{(eq)}}{\partial x_{1k} \partial x_{1m}} \right] = \frac{c^2}{3} \left[\frac{\partial^2}{\partial x_{1m} \partial x_{1m}} (\rho u_n) + 2 \frac{\partial^2}{\partial x_{1m} \partial x_{1n}} \rho u_n \right] \quad (\text{A.23})$$

Substituting Eq. (A.23) back into Eq. (A.18), the momentum equation becomes:

$$\frac{\partial \rho u_n}{\partial t} + \frac{\partial \rho u_k u_n}{\partial x_{1k}} = - \frac{\partial p}{\partial x_{1n}} + \left(\tau - \frac{1}{2}\right) \frac{c^2}{3} \left[\frac{\partial^2}{\partial x_{1m} \partial x_{1m}} (\rho u_n) + 2 \frac{\partial^2}{\partial x_{1m} \partial x_{1n}} \rho u_n \right] \quad (\text{A.24})$$

where the pressure p and kinematic viscosity ν are given by:

$$p \equiv c_s^2 \rho = \frac{\rho}{3} \quad (\text{A.25})$$

$$\nu \equiv \frac{c^2}{3} \left(\tau - \frac{1}{2}\right) = \frac{2\tau - 1}{6} \quad (\text{A.26})$$

Therefore, the LBE recovers the N-S equations [Eq. (A.27–28)] in the incompressible flow limit:

$$\frac{\partial u_{\alpha}}{\partial x_{\alpha}} = 0 \quad (\text{A.27})$$

$$\frac{\partial u_\beta}{\partial t} + u_\alpha \frac{\partial u_\beta}{\partial x_\alpha} = -\frac{1}{\rho} \frac{\partial p}{\partial x_\beta} + \nu \nabla^2 u_\beta \quad (\text{A.28})$$

BIBLIOGRAPHY

1. S. Chen and G. D. Doolen, Lattice Boltzmann method for fluid flows, *Ann. Rev. Fluid Mech.* 30, pp. 329-364, 1998.
2. L.-S. Luo, The lattice-gas and lattice Boltzmann methods: Past, Present, and Future, *Proceedings of the International Conference on Applied Computational Fluid Dynamics*, Beijing, China, pp. 52-83, 2000.
3. K. Huang, *Statistical Mechanics*, John Wiley & Sons, New York, 1987.
4. R. Peyret, and T.D. Taylor, *Computational Methods for Fluid Flow*, Springer-Verlag, New York, 1983.
5. J.C. Tannehill, D.A. Anderson, and R.H. Pletcher, *Computational Fluid Mechanics And Heat Transfer*, 2nd edition, Taylor and Francis, 1997.
6. D.A. Wolf-Gladrow, *Lattice Gas Cellular Automata and Lattice Boltzmann Models: an Introduction*, Springer-Verlag, Heidelberg, 2000.
7. D.J. Evans, and G.P. Morris, Nonequilibrium molecular-dynamics simulation of couette flow in two-dimensional fluids, *Phys. Rev. E*, 51(19), pp. 1776-1779, 1983.
8. J. Goodfellow, *Molecular Dynamics*, Macmillan Press, 1991.
9. D.C. Rapaport, *The Art of Molecular Dynamics Simulation*, Cambridge University Press, 1995.
10. U. Frisch, B. Hasslacher, and Y. Pomeau, Lattice-Gas automata for the Navier-Stokes equation, *Phys. Rev. Lett.* 56, pp. 1505-1508, 1986.
11. U. Frisch, D. d'Humières, B. Hasslacher, P. Lallemand, Y. Pomeau, and J.-P. Rivet, Lattice gas hydrodynamics in two and three dimensions, *Complex Systems* 1, pp. 649-707, 1987.
12. O. van Genabeek, and D. H. Rothman, Macroscopic manifestations of microscopic flows through porous media: Phenomenology from simulation, *Ann. Rev. of Earth and Planetary Sciences*, 24, pp. 63-87, 1996.

13. S. Wolfram, Cellular automation fluids. 1: Basic Theory, *J. Stat. Phys.*, 45, pp. 471-526, 1986.
14. D.H. Rothman, and S. Zaleski, *Lattice Gas Cellular Automata*, Cambridge University Press, Cambridge. 1997.
15. G.R. McNamara, and G. Zanetti, Use of the Boltzmann equation to simulate lattice-gas automata, *Phys. Rev. Lett.* 61, pp. 2332-2335, 1988.
16. H. Chen, S. Chen, and W.H. Matthaeus, Recovery of the Navier-Stokes equations using a lattice-gas Boltzmann method, *Phys. Rev. A* 45, pp. R5339- R5342, 1992.
17. Y.H. Qian, D. d'Humières, and P. Lallemand, Lattice BGK models for Navier-Stokes equation, *Europhys. Lett.* 17, pp. 479-484, 1992.
18. J.A. Somers, Direct Simulation of fluid flow with cellular automata and the lattice-Boltzmann equation, *Appli. Sci. Res.* 51, 127, 1993.
19. V. Sofonea, Lattice Boltzmann approach to collective-particle interaction in magnetic fluids. *Europhysics Letters* 25, pp. 385-390, 1994.
20. H. Fang, Z. Lin, and Z. Wang, Lattice Boltzmann simulation of viscous fluid systems with elastic boundaries, *Phys. Rev. E* 57, pp. R25-R29, 1998.
21. C.M. Teixeira, Incorporating turbulence models into the lattice-Boltzmann method, *International Journal of Modern Physics C* 9, pp. 1159-1175, 1998.
22. B. Chopard, and P.O. Luthi, Lattice Boltzmann computations and applications to physics, *Theoretical Computer Science* 217, pp. 115-130, 1999.
23. A.D. Fox, and S.J. Maskell, Two-way interactive nesting of primitive equation ocean models with topography, *Journal of Physics in Oceanography* 25, pp. 2977-2996, 1995.
24. A.D. Fox, and S.J. Maskell, A nested primitive equation model of the iceland-faeroe front, *Journal of Geophysics Research* 101, pp. 18259-18278, 1996.
25. N.S. Martys, and H. Chen, Simulation of multicomponent fluids in complex three-dimensional geometries by the lattice Boltzmann method, *Phys. Rev. E* 53, pp. 743-750, 1996.
26. A.J.C. Ladd, Numerical simulations of particulate suspensions via a discretized Boltzmann equation: Part 1. Theoretical foundation, *J. Fluid Mech.* 271 pp. 285-309, 1994.
27. A.J.C. Ladd, Numerical simulations of particulate suspensions via a discretized Boltzmann equation: Part 2. Numerical results, *J. Fluid Mech.* 271, pp. 311-339, 1994.
28. L. Giraud, D. d'Humières, and P. Lallemand, A lattice Boltzmann model for viscoelasticity, *Int. J. Mod. Phys. C*, 8, pp. 805-815, 1997.

29. L. Giraud, D. d'Humières, and P. Lallemand, A lattice Boltzmann model for Jeffreys viscoelastic fluid, *Europhys. Lett.*, 42, pp. 625-630, 1998.
30. J.-P. Boon, D. Dab, R. Kapral, and A. Lawniczak, Lattice gas automata for reactive systems, *Phys. Rep.* 273, pp. 55-148, 1996.
31. S. Succi, *The Lattice Boltzmann Equation for Fluid Dynamics and Beyond*, Oxford University Press, 2001.
32. R.K. Pathria, *Statistical Mechanics*, 2nd Edition, Butterworth-Heinemann, 1996.
33. P.L. Bhatnagar, E.P. Gross, and M. Krook, A model for collision processes in gases. I. Small amplitude processes in charged and neutral one-component system, *Phys. Rev.*, 94, pp. 511-525, 1954.
34. D. Kandhai, A. Koponen, A. Hoekstra, M. Kataja, J. Timonen, and P.M.A. Slood, Implementation aspects of 3D lattice-BGK: boundaries, accuracy, and a new fast relaxation method, *J. Comput. Phys.*, 150, pp. 482-501, 1999.
35. D. d'Humières, I. Ginzburg, M. Krafczyk, P. Lallemand, and L.-S. Luo, Multi-relaxation-time lattice Boltzmann models in three dimensions, *Phil. Trans. R. Soc. Lond. A* 360, pp. 437-451, 2002.
36. X. He and L.-S. Luo, A priori derivation of the lattice Boltzmann equation, *Phys. Rev. E*, 55, pp. R6333-R6336, 1997.
37. X. He and L.-S. Luo, Theory of the lattice Boltzmann equation: from the Boltzmann equation to the lattice Boltzmann equation, *Phys. Rev. E*, 56, pp. 6811-6817, 1997.
38. P. J. Davis and P. Rabinowitz, *Methods of Numerical Integration*, 2nd ed., Academic, New York, 1984.
39. R. S. Maier, R.S. Bernard, and D.W. Grunau, Boundary conditions for the lattice Boltzmann method, *Phys. Fluids*, 8 (7), pp.1788-1801, 1996.
40. P. Ziegler, Boundary conditions for lattice Boltzmann simulations, *J. Stat. Phys.*, 71, pp. 1171-1177, 1993.
41. I. Ginzbourg, and D. d'Humières, Local second-order boundary methods for lattice Boltzmann models, *J. Stat. Phys.*, 84, pp. 927-971, 1995.
42. S. Chen, D. Martínez, and R. Mei, On boundary conditions in lattice Boltzmann method, *Phys. Fluids* 8, pp. 2527-2536, 1996.
43. Q. Zou and X. He, On pressure and velocity boundary conditions for the lattice Boltzmann BGK model, *Phys. Fluids* 9, pp. 1591-1598, 1997.
44. D.W. Gruna, *Lattice Methods for Modeling Hydrodynamics*, PhD thesis, Colorado State University, 1993.

45. D. Yu, Viscous Flow Computations with the Lattice Boltzmann Equation Method, Ph.D. thesis, Department of Aerospace Engineering, mechanics and Engineering Science, Univ. of Florida, 2002.
46. T. Inamuro, M. Yoshino, and F. Ogino, A non-slip boundary condition for lattice Boltzmann simulations, *Phys. Fluids*, 7, pp. 2928-2930, 1995.
47. R. Mei, and W. Shyy, On the finite difference-based lattice Boltzmann method in curvilinear coordinates, *J. Compu. Phys.* 143, pp. 426-448, 1998.
48. C.K. Aidun, Y. Lu, Lattice Boltzmann simulations of solid particles suspended in fluid, *J. Stat. Phys.*, 81, pp. 49-61, 1995.
49. R. Mei, L.-S. Luo and W. Shyy, An accurate curved boundary treatment in the lattice Boltzmann method, *J. Compu. Phys.* 155, pp. 307-329, 1999.
50. R. Mei, W. Shyy, D. Yu, and L.-S. Luo, Lattice Boltzmann method for 3-D flows with curved boundary, *J. Comp. Phys.* 161, pp. 680-699, 2000.
51. A. Dupuis, From a Lattice Boltzmann Model to a Parallel and Reusable Implementation of a Virtual River, PhD thesis, University of Geneva, 2002.
52. O. Filippova and D. Hänel, Grid refinement for lattice-BGK models, *J. Comput. Phys.* 147, pp. 219-228, 1998.
53. X. He, Q. Zou, L.-S. Luo, and M. Dembo, Analytic solutions and analysis on non-slip boundary condition for the lattice Boltzmann BGK model, *J. Stat. Phys.*, 87, pp.115-136, 1997.
54. Q. Zou, S. Hou, and G.D. Doolen, Analytical solutions of the lattice Boltzmann BGK model, *J. Stat. Phys.*, 81, pp. 319-334, 1995.
55. J. Buick and C. Greated, Gravity in the lattice Boltzmann model, *Phys. Rev. E* 61, pp. 5307-5320, 2000.
56. D. Yu, R. Mei, L.-S. Luo, and W. Shyy, Viscous flow computations with the method of lattice Boltzmann equation, *Progress in Aerospace Sciences*, 39, pp. 329-367, 2003.
57. Z. Guo, and C. Zheng, An extrapolation method for boundary conditions in lattice Boltzmann method, *Phys. Fluids*, 14 (6), pp. 2007-2010, 2002.
58. J.A. Cosgrove, J.M. Buick, S.J. Tonge, C.G. Munro, C.A. Greated, and D.M. Campbell, Application of the lattice Boltzmann method to transition in oscillatory channel flow, *J. Phys. A: Math. Gen.* 36, pp. 2609-2620, 2003.
59. F.H. Harlow, and J.E. Welch, Numerical calculation of time-dependent viscous incompressible flow, *Phys. Fluids* 8, pp. 2182-2189, 1965.

60. B.J. Daly, Numerical study of the effect of surface tension on interface instability, *Phys. Fluids* 12, pp. 1340-1354, 1969.
61. C.W. Hirt, and B.D. Nichols, Volume of fluid (VOF) method for the dynamics of free boundaries, *J. Comput. Phys.*, 39, pp. 201-225, 1981.
62. J.A. Sethian, *Level Set Methods: Evolving Interfaces in Geometry, Fluid Mechanics, Computer Vision, and Materials Science*, Cambridge University Press, 1996.
63. M.E. McCracken, Development and Evaluation of Lattice Boltzmann Models for Investigations of Liquid Break-up, PhD thesis, Purdue University, 2004.
64. S.O. Unverdi, G. Tryggvason, A front-tracking method for viscous, incompressible, multi-fluid flows, *J. Comp. Phys* 100, pp. 25-37, 1992.
65. A.R. Wadhwa, V. Magi, and J. Abraham, Numerical studies of droplet interactions, *Proc. of International Conference on Liquid Atomization and Spray Systems*, Sorrento, Italy, July 2003.
66. G. Tryggvason, B. Bunner, A. Esmaeeli, D. Juric, N. Al-Rawahi, W. Tauber, J. Han, S. Nas, and Y.J. Jan, A front-tracking method for the computations of multiphase flow, *J. Comput. Phys.*, 162, pp. 708-759, 2001.
67. S.G. Yoon, A Fully Nonlinear Model for Atomization of High-Speed Jets, PhD thesis, Purdue University, 2002.
68. A.K. Gunstensen, D.H. Rothman, S. Zaleski, and G. Zanetti, Lattice Boltzmann model of immiscible fluids, *Phys. Rev. A* 43, pp. 4320-4327, 1991.
69. X. Shan and H. Chen, Lattice Boltzmann model for simulation flows with multiple phases and components, *Phys. Rev. E* 47, pp. 1815-1819, 1993.
70. X. Shan and H. Chen, Simulation of nonideal gases and liquid-gas phase transitions by the lattice Boltzmann equation, *Phys. Rev. E* 49, pp. 2941-2948, 1994.
71. X. Shan and G. D. Doolen, Multicomponent lattice-Boltzmann model with interparticle interaction, *J. Stat. Phys.* 81, pp. 379-393, 1995.
72. X. Shan, and D. Doolen, Diffusion in a multicomponent lattice Boltzmann equation model, *Phys. Rev. E* 54, pp. 3614-3620, 1996.
73. M. Swift, W. Osborn, and J. Yeomans, Lattice Boltzmann simulation of nonideal fluids, *Phys. Rev. Lett.* 75, pp. 830-833, 1995.
74. M. Swift, S. Orlandini, W. Osborn, and J. Yeomans, Lattice Boltzmann simulations of liquid-gas and binary-fluid systems, *Phys. Rev. E* 54, pp. 5041-5052, 1996.

75. R. Nourgaliev, T. Dinh, T. Theofanous, and D. Joesph, The lattice Boltzmann equation method: theoretical interpretation, numerics and implications, *Int. J. Multiphase Flow* 29, pp. 117-169, 2003.
76. X. He, S. Chen, and R. Zhang, A lattice Boltzmann scheme for incompressible multiphase flow and its application in simulation of Rayleigh-Taylor instability, *J. Comput. Phys.*, 152, pp. 642-663, 1999.
77. X. He, R. Zhang, S. Chen, and G.D. Doolen, On the three-dimensional Rayleigh-Taylor instability, *Phys. Fluids*, 11 (5), pp. 1143-1152, 1999.
78. X. He, and G. D. Doolen, Thermodynamic foundations of kinetic theory and lattice Boltzmann models for multiphase flows, *J. Stat. Phys.* 107, pp. 309-328, 2002.
79. Q. Kang, D. Zhang and S. Chen, Displacement of a two-dimensional immiscible droplet in a channel, *Phys. Fluids*, 14 (9), pp. 3203-3214, 2002.
80. M. Sukop and D. Or, Lattice Boltzmann method for modeling liquid-vapor interface configurations in porous media, *Water Resource Research*, 40, W01509, 2004.
81. C. Pan, Use of Pore-scale Modeling to Understand Flow and Transport in Porous Media, PhD thesis, Department of Environmental Science & Engineering, University of North Carolina at Chapel Hill, 2003.
82. D. Qian, Bubble Motion, Deformation, and Breakup in Stirred Tanks, PhD thesis, Department of Chemical Engineering, Clarkson University, 2003.
83. N.S. Martys, and J.F. Douglas, Critical properties and phase separation in lattice Boltzmann fluid mixtures, *Phys. Rev. E*, 63, 031205, 2001.
84. L.-S. Luo, and S.S. Girimaji, Theory of the lattice Boltzmann method: Two-fluid model for binary mixtures, *Phys. Rev. E*, 67, 036302, 2003.
85. Z. Guo, C. Zheng, and B. Shi, Discrete lattice effects on the forcing term in the lattice Boltzmann method, *Phys. Rev. E*, 65, 046308, 2002.
86. S. Hou, Lattice Boltzmann Method for Incompressible Viscous Flow, Ph.D. thesis, Department of Mechanical Engineering, Kansas State Univ., 1995.
87. K. Sankaranarayanan, Lattice Boltzmann Simulations of Gas-Liquid Bubbly Flows, PhD thesis, Princeton University, 2002.
88. H. Lamb, *Hydrodynamics*. Cambridge University Press, Dover, Cambridge, New York, 6th edition, 1932.
89. S. Hou, X. Shan, Q. Zou, G. Doolen, and W. Soll, Evaluation of two lattice Boltzmann models for multiphase flows, *J. Comput. Phys.*, 138, pp. 695-713, 1997.
90. M. Sahimi, *Application of Percolation Theory*. Taylor & Francis, Bristol, PA, 1994.

91. Z. Yang, T. Dinh, R. Nourgaliev, and B. Sehgal, Numerical investigation of bubble growth and detachment by the lattice-Boltzmann method, *Int. J. Heat Mass Transfer* 44, pp. 195-206, 2001.
92. F.A.L. Dullien, *Porous Media: Fluid Transport and Pore Structure*, Academic, New York, 1992.
93. U.S. Jeng, L. E. Sibov, L. Crow, A. Steyerl, Viscosity effect on capillary waves at liquid interfaces, *J. Phys. Cond. Matter* 10, pp. 4955-4962, 1998.
94. K. Langaas, and J.M. Yeomans, Lattice Boltzmann simulation of a binary fluid with different phase viscosities and its application to fingering in two dimensions, *Eur. Phys. J. B* 15, pp. 133-141, 2000.
95. J. van der Waals, PhD thesis, University of Leiden, Leiden, The Netherlands, 1873.
96. X. He, X. Shan, and G.D. Doolen, Discrete Boltzmann equation model for nonideal gases, *Phys. Rev. E* 57, pp. R13-R16, 1998.
97. R. Zhang, *Lattice Boltzmann Approach for Immiscible Multiphase Flow*, PhD thesis, Department of Mechanical Engineering, University of Delaware, 2000.
98. P. Yuan, and L. Schaefer, Lattice Boltzmann simulation of two-phase flow and heat transfer in a rectangular channel”, *Proceedings of 2004 ASME International Mechanical Engineering Congress (Fluids Engineering Division)*, pp. 463-473, 2004.
99. D.A. McQuarrie, and J.D. Simon, *Molecular Thermodynamics*, University Science Books, Sausalito, California, 1999.
100. S.I. Sandler, *Chemical and Engineering Thermodynamics*, 3rd edition, John Wiley & Sons, Inc., 1999.
101. J.-L. Wang, *Global Phase Diagrams and Critical Phenomena of Binary Mixtures*, PhD thesis, Department of Mechanical Engineering, Swinburne University of Technology, 2003.
102. N. F. Carnahan, and K.E. Starling, Intermolecular repulsions and the equation of state for fluids, *AICHE J.* 18 (6), pp. 1184-1189, 1972.
103. L.M. Quintales, J.M. Alvariño, and S. Velasco, Computational derivation of coexistence curves for van-der-Waals-type equations, *Eur. J. Phys.*, 9, pp. 55-60, 1988.
104. L. Schaefer, *Single Pressure Absorption Heat Pump Analysis*, PhD thesis, Department of Mechanical Engineering, Georgia Institute of Technology, 2000.
105. P. Pavlo, G. Vahala, and L. Vahala, Higher order isotropic velocity grids in lattice methods, *Phys. Rev. Lett.* 80, pp. 3960-3963, 1998.

106. F. J. Alexander, S. Chen, and J. D. Sterling, Lattice Boltzmann thermohydrodynamics, *Phys. Rev. E* 47, pp. R2249-R2252, 1993.
107. X. Shan, Solution of Rayleigh– Bénard convection using a lattice Boltzmann method, *Phys. Rev. E* 55, pp. 2780-2788, 1997.
108. G. McNamara, A. L. Garcia, and B. J. Alder, Stabilization of thermal lattice Boltzmann models, *J. Stat. Phys.* 81, pp. 395-408, 1995.
109. J. Huang, F. Xu, H. Vallieres, D.H. Feng, Y.-H. Qian, B. Fryxell, and M.R. Strayer, A thermal LBGK model for the large density and temperature differences, *Int. J. Mod. Phys. C* 8, pp. 827,841, 1997.
110. B.M. Boghosian, and P.V. Coveney, Inverse Chapman-Enskog derivation of the thermodynamic lattice-BGK model for the ideal gas, *Int. J. Mod. Phys. C* 9, pp. 1231-1245, 1998.
111. T. Inamuro, M. Yoshino, H. Inoue, R. Mizuno and F. Ogino, A lattice Boltzmann method for a binary miscible fluid mixture and its application to a heat-transfer problem, *J. Compu. Phys.* 179, pp. 201-215, 2002.
112. C. Shu, Y. Peng, and Y. Chew, Simulation of natural convection in a square cavity by Taylor series expansion- and least squares- based lattice Boltzmann method, *Int. J. Mod. Phys.* 13, pp. 1399-1414, 2002.
113. F. Busse, *Hydrodynamics instabilities and the transition to turbulence*, 2nd ed., Springer-Verlag, Berlin, 1986.
114. K. Kono, T. Ishizuka, H. Tsuda, , and A. Kurosawa, Application of lattice Boltzmann model to multiphase flows with phase transition,” *Computer Phys. Communications*, 129, pp. 110-120, 2000.
115. W. Miller, and S. Succi, A lattice Boltzmann model for anisotropic crystal growth from melt,” *J. Stat. Phys.*, 107, pp. 173-186, 2002.
116. N. Takada, M. Misawa, A. Tomiyama, and S. Hosokawa, Simulation of bubble motion under gravity by lattice Boltzmann method, *J. Nuclear Science and Technology*, 38 (5), pp. 330-341, 2001.
117. J. Tölke, M. Krafczyk, M. Schulz, E. Rank, and Berrios, Implicit discretization and nonuniform mesh refinement approaches for FD discretizations of LBGK models, *Int. J. Mod. Phys. C*, 9, pp. 1143-1157, 1998.
118. T. Lee and C.-L. Lin, A characteristic Galerkin method for discrete Boltzmann equation, *J. Compu. Phys.*, 171, pp. 336-356, 2001.
119. A. Lamura, G. Gonnella, and J.M. Yeomans, A lattice Boltzmann model of ternary fluid mixtures, *Europhys. Lett*, 45 (3), pp. 314-320, 1999.

120. T. Azami, S. Nakamura, and T. Hibiya, Effect of Oxygen on thermocapillary convection in a molten silicon column under microgravity, *J. Electrochemical Soc.*, 148, pp. G185-G189, 2001.
121. J.M. Buick, J.A. Cosgrove, S.J. Tonge, M.W. Collins, A.J. Mulholland and B.A. Steves, The lattice Boltzmann equation for modeling arterial flows: Review and Application. *Biomedicine & Pharmacotherapy*, 56(7), pp. 345-346, 2002.
122. H. Yu, L.-S. Luo, and S. S. Girimaji, Scalar mixing and chemical reaction simulations using lattice Boltzmann method, *Int. J. Compu. Eng. Sci.* 3(1), pp. 73-87, 2002.
123. K. Yamamoto, X. He, and G.D. Doolen, Simulation of combustion field with lattice Boltzmann method, *J. Stat. Phys.*, 107, pp. 367-383, 2002.
124. D. Kandhai, A. Koponen, A.G. Hoekstra, M. Katajam, J. Timonen, and P.M.A. Slood, Lattice-Boltzmann hydrodynamics on parallel systems, *Computer Physics Communications*, 111:14-26, 1998.
125. R. Benzi, and S Succi, Two-dimensional turbulence with the lattice Boltzmann equation, *J. Phys. A: Math. Gen.* 23 L1-L5, 1990.
126. A.J.C. Ladd, and R. Verberg, Lattice-Boltzmann simulations of particle-fluid suspensions, *J. Stat. Phys.*, 104, pp. 1191-1251, 2001.